Supporting Information

Isolation and Characterization of Carbene-Supported Air Stable Co(II)-Radical Complex with Bileptic Redox Non-innocent Ligands: Stability, Bonding, Ring-Opening Copolymerization Studies and Photo-Catalytic Ring Cyclization Activity

Sujit Das,[a] Sangita Mondal,[a] Sonam Suthar,[a] Ranay Kumar Ray,[a] Karunamayee Mondal,[a] Avany A Raveendran,[a] Subuhan Ahamed,[a] Chandan Maji,[a] Mahiuddin Baidya,*[a] Björn Schwarz,*[b] Debashis Chakraborty,*[a] Liviu Ungur,*[c] and Kartik Chandra Mondal*[a]

Department of Chemistry, Indian Institute of Technology Madras, Chennai 600036, India. E-mail: csdkartik@iitm.ac.in.

Institute for Applied Materials (IAM), Karlsruhe Institute of Technology (KIT), Hermann-von-Helmholtz-Platz 1, 76344 Eggenstein-Leopoldshafen, Germany.

Department of Chemistry, National University of Singapore.

Content:

1. General Synthesis

All the organic solvents (THF, *n*-hexane, toluene, and C_6D_6) were soaked with 3 Å molecular sieves to remove water and followed by distillation with Na metal and NaK alloy three times under the flow of high-purity argon gas. All the manipulations were performed inside the glove box running with argon gas below the H_2O/O_2 level of 10 ppm. The dithiolene radical anion $[(THF)_2Li(SS\text{-}NHC{=}Se)]$ (**1b)** was prepared by following a similar synthetic method, which led to the synthesis of $[(THF)_2Li(SS\text{-}NHC{=}S)]$ (**1a**), reported by Robinson et al.[15-17] X-ray single crystal mounted was performed using paratone oil under the flow of argon gas and data was collected in Bruker D8 VENTURE model (machine) at 100 K. Data was refined using Apex-4 package. CV was measured in alloyed distilled THF in a potentiometer (Mterohm). NMR was recorded in C_6D_6 in a 500 MHz Bruker instrument at IIT Madras. EPR was simulated using the EASY-SPIN package.

2. Synthesis

Synthesis of complex $[Co^{II}(cAAC)(SS\text{-}NHC{=}S)Cl]$ (**3a**)**:** The dithiolene radical anion $[(THF)_2Li(SS\text{-}NHC{=}S)]$ (**1a**) (0.8 mmol, 506 mg) was dissolved in 30 mL of THF in a 100 mL Schlenk flask to obtained dark purple solution and separately $(cAAC)_2Co_2Cl_4$ (**2**) (0.4 mmol, 268 mg) was also dissolved in 15 mL of THF in another Schlenk flask forming a blue solution. They were mixed via a cannula and stirred for 1 h at room temperature (rt) to obtain a royal

blue. The reaction mixture was stirred for another 4 h to ensure complete conversion. THF was then removed under vacuum, yielding a dry blue mass extracted in *n*-hexane (40 mL). Dark blue needles of complex **3a** were formed from the concentrated solution after a day. The yield is 56%. Decomposition: above 90 ^{o}C. IR (KBr, cm^{-1}): 2964, 2927, 2869, 1629, 1506, 1422, 1352, 1319, 1261, 1191, 1033, 888, 805, 710. UV-vis band at 350, 505, 552, 598, 725, and 796 nm. C, H, N analysis% (calcd): C 65.48 (65.55), H 7.53 (7.45), N 4.79 (4.88), matching with the chemical formula Co^{II}(cAAC)(SS-NHC=S).

Synthesis of complex [Co^{II}(cAAC)(SS-NHC=Se)Cl] (**3b**)**:** A solution of the dithiolene radical anion [$(THF)_2$Li(SS-NHC=Se)] (**1b**) (0.8 mmol, 542 mg) in 30 mL of THF was prepared in a 100 mL Schlenk flask, resulting in a dark purple solution. In a separate Schlenk flask, a solution of the cobalt precursor $(cAAC)_2Co_2Cl_4$ (**2**) (0.4 mmol, 268 mg) in 12 mL of THF was prepared, giving a blue solution. The ligand solution was added dropwise to the cobalt complex under an inert atmosphere. During the addition, the reaction color gradually changed from dark blue to green, indicating the progress of the reaction.

The resulting mixture was stirred for 16 hours at room temperature to ensure complete conversion. The solvent was removed under reduced pressure to extract a dry green solid with 30 mL of n-hexane. Upon concentration of the hexane extract, dark blue needle-like crystals of complex **3b** began to form within 1-2 hours. The isolated yield was 50%. The product decomposes above 90 °C. IR (KBr, cm^{-1}): 3064, 2960, 2928, 2863, 2066, 1765, 1628, 1584, 1443, 1381, 1264, 1179, 1054, 803, 649, and 520. UV-vis (in THF): 303, 363, 486, 654, 736, and 842 nm. C, H, N analysis% (calcd); $C_{47}H_{65}ClCoN_3S_2Se$: C 62.14 (62.07), H 7.16 (7.20), N 4.69 (4.62).

Pure single crystals were isolated (after removal of mother liquor using a syringe; washed with cold *n*-hexane), which were ground to form powders required for all other characterizations (EPR, UV-sis, NMR, and CV). The single crystals of **3a** and **3b** retain their shiny blue color over seven days in open air. The THF solution loses 50% of its intensity after 9 h.

3. UV-vis spectroscopy measurements

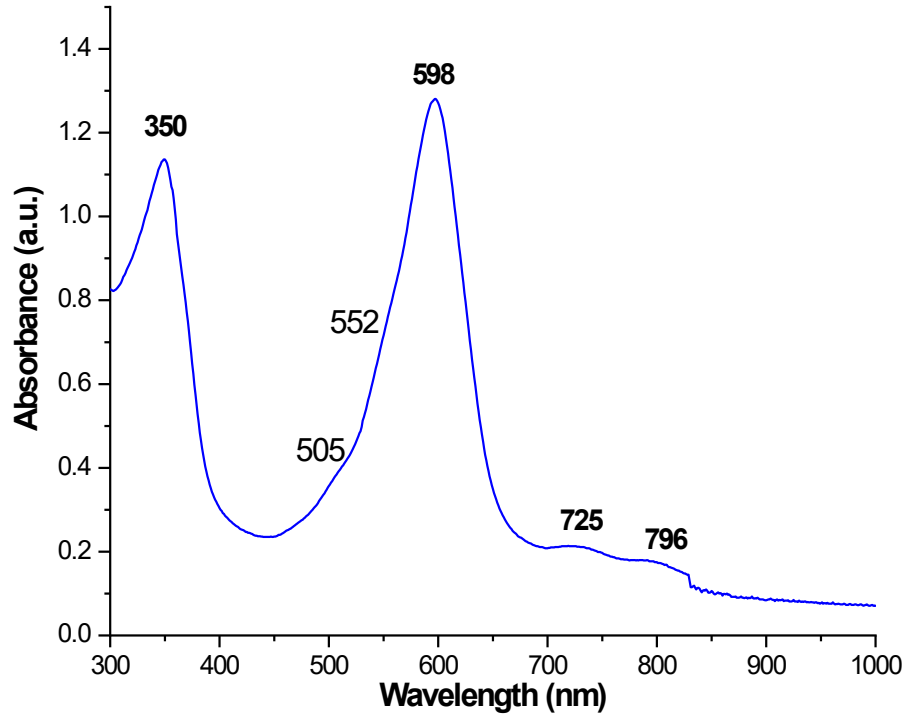

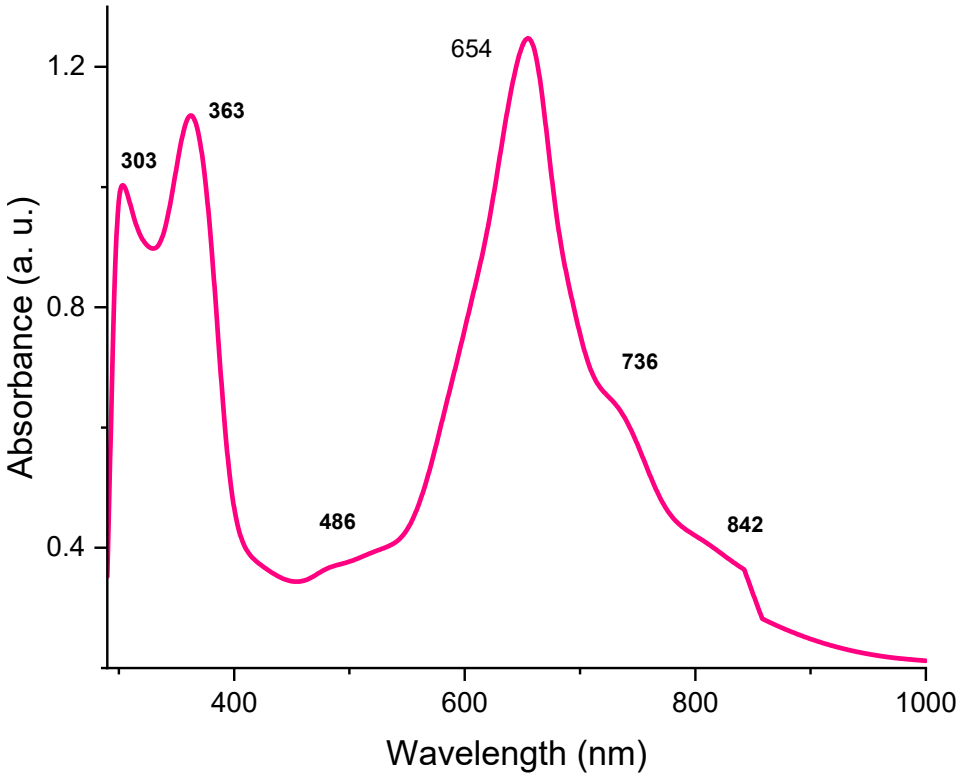

Figure S1. UV-Vis absorption spectrum of THF solutions of complexes [Co^{II}(cAAC)(SS-NHC=S)Cl] (**3a**) (top) and [Co^{II}(cAAC)(SS-NHC=Se)Cl] (**3b**)(bottom). 736 (1.307×10^3 L mol^{-1} cm^{-1}), 654 (2.620×10^3 L mol^{-1} cm^{-1}), 363 (2.348×10^3 L mol^{-1} cm^{-1}).

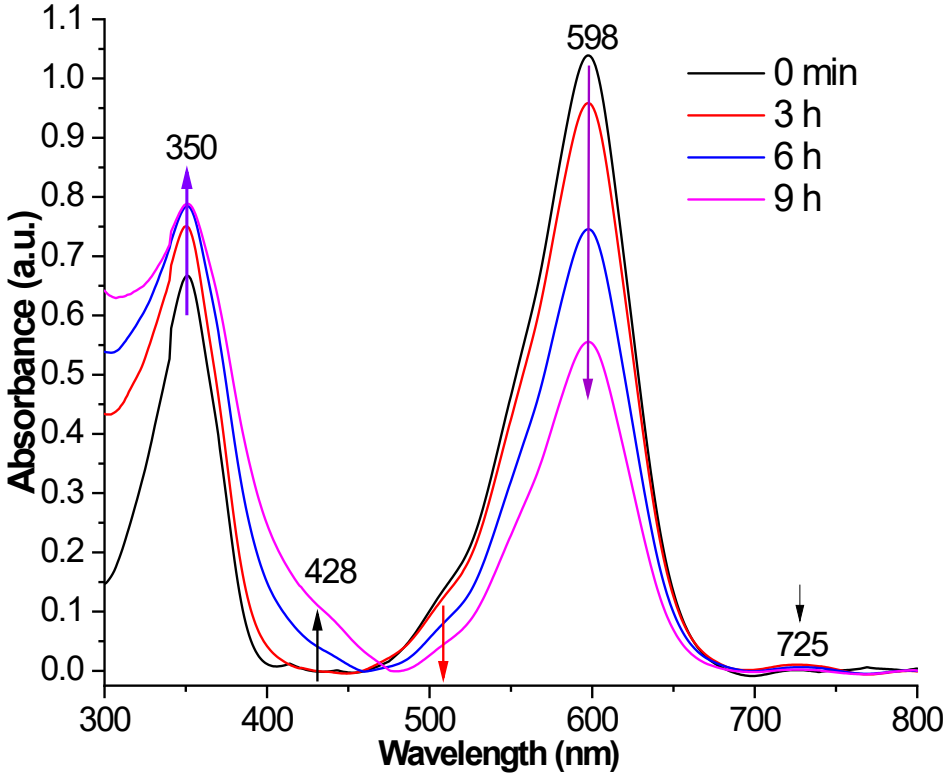

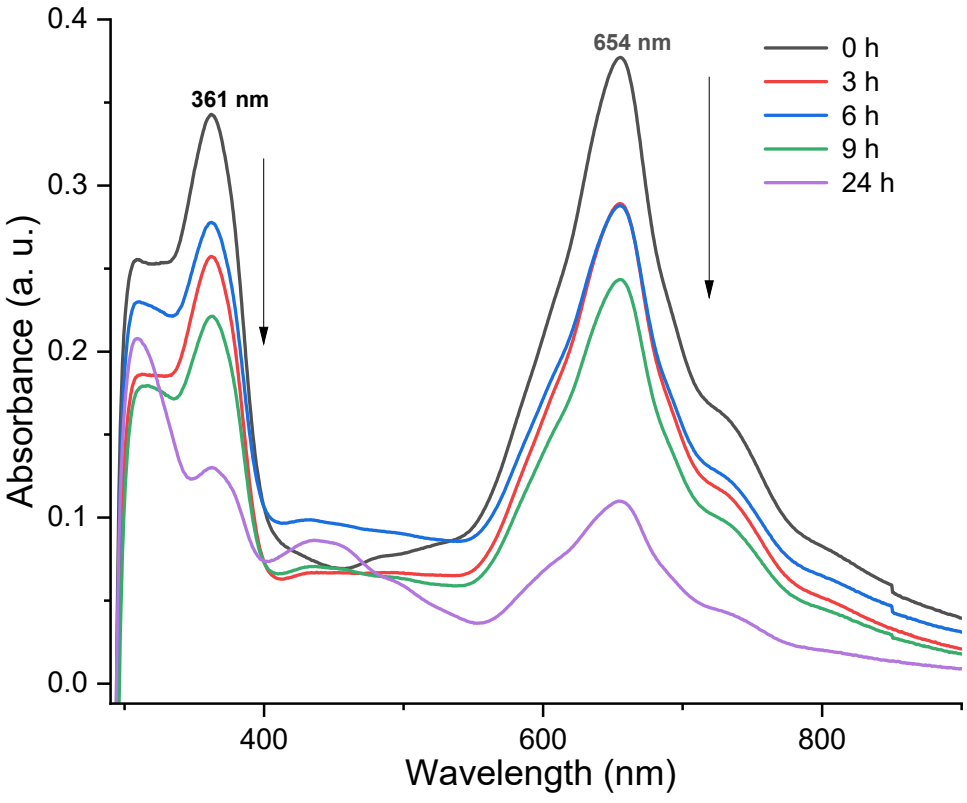

Figure S2. UV-Vis absorption spectrum of THF solutions of complexes [Co^{II}(cAAC)(SS-NHC=S)Cl] (**3a**) (top) and [Co^{II}(cAAC)(SS-NHC=Se)Cl] (**3b**) (bottom) after exposure to open air. 50% of those reacted in the air around 9-10 h.

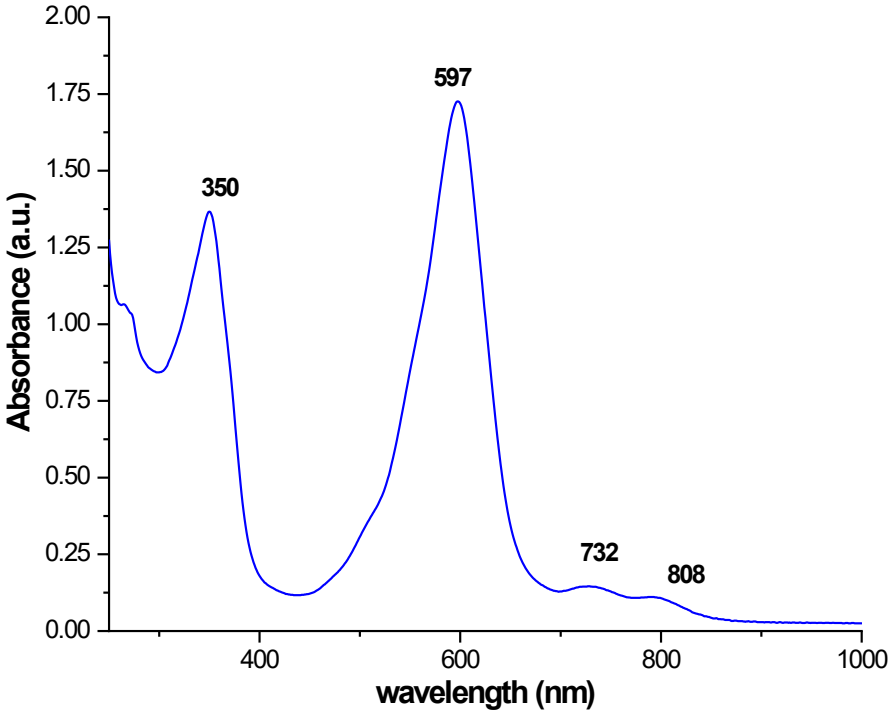

Figure S3. Single crystals (top) of complex **3a** in open air after seven days. They remain shiny, dark blue in the solid state, which was dissolved in THF, and the UV-vis spectrum was recorded (bottom).

4. IR spectra

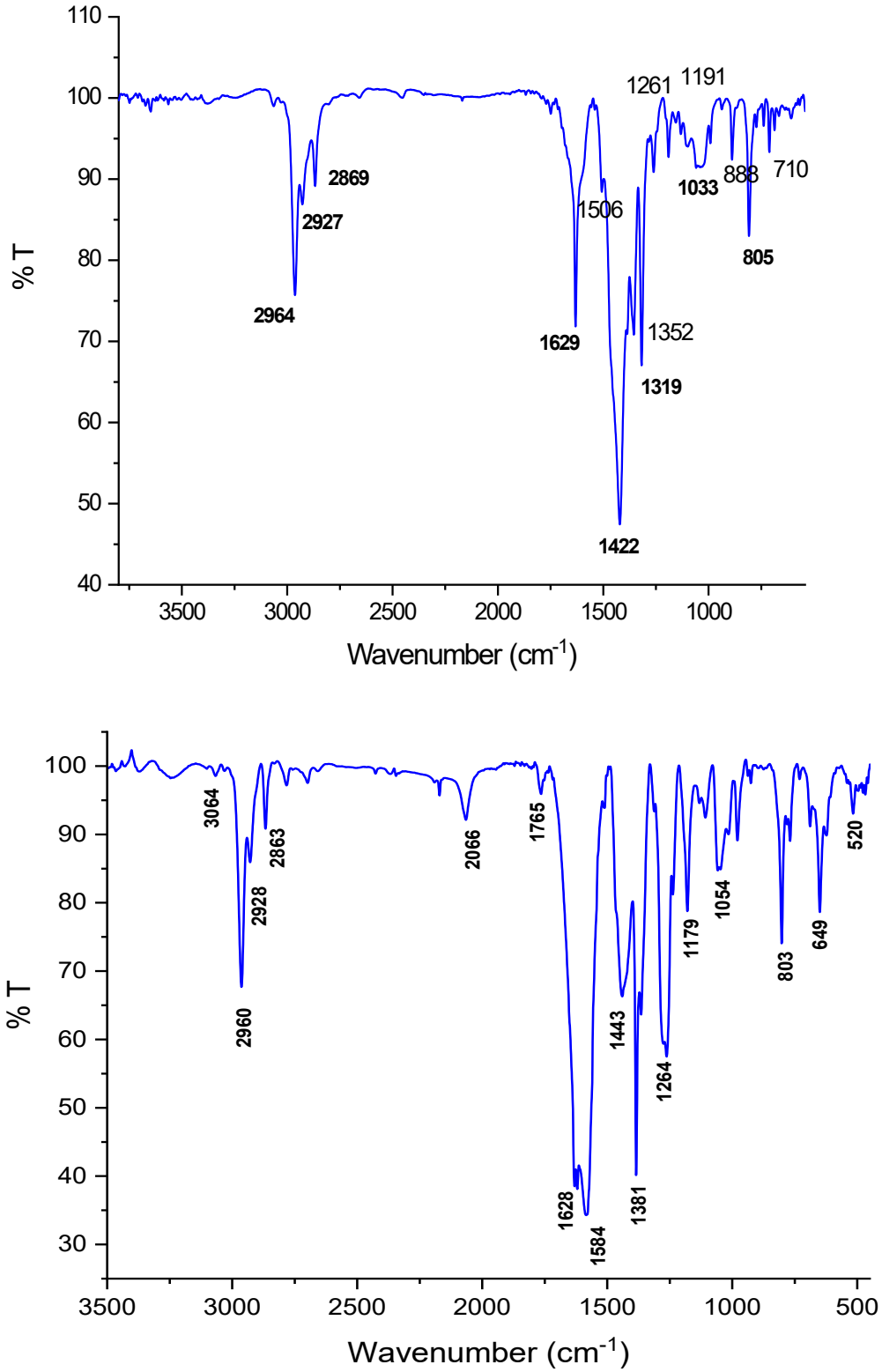

Figure S4. FT-IR spectrum of complexes [Co^{II}(cAAC)(SS-NHC=S)Cl] (**3a**) (top) and [Co^{II}(cAAC)(SS-NHC=Se)Cl] (**3b**) (bottom) with dry KBr. The sample was prepared inside a glove box. (The KBr was made moisture-free by heating it at 250°C under vacuum.)

5. NMR

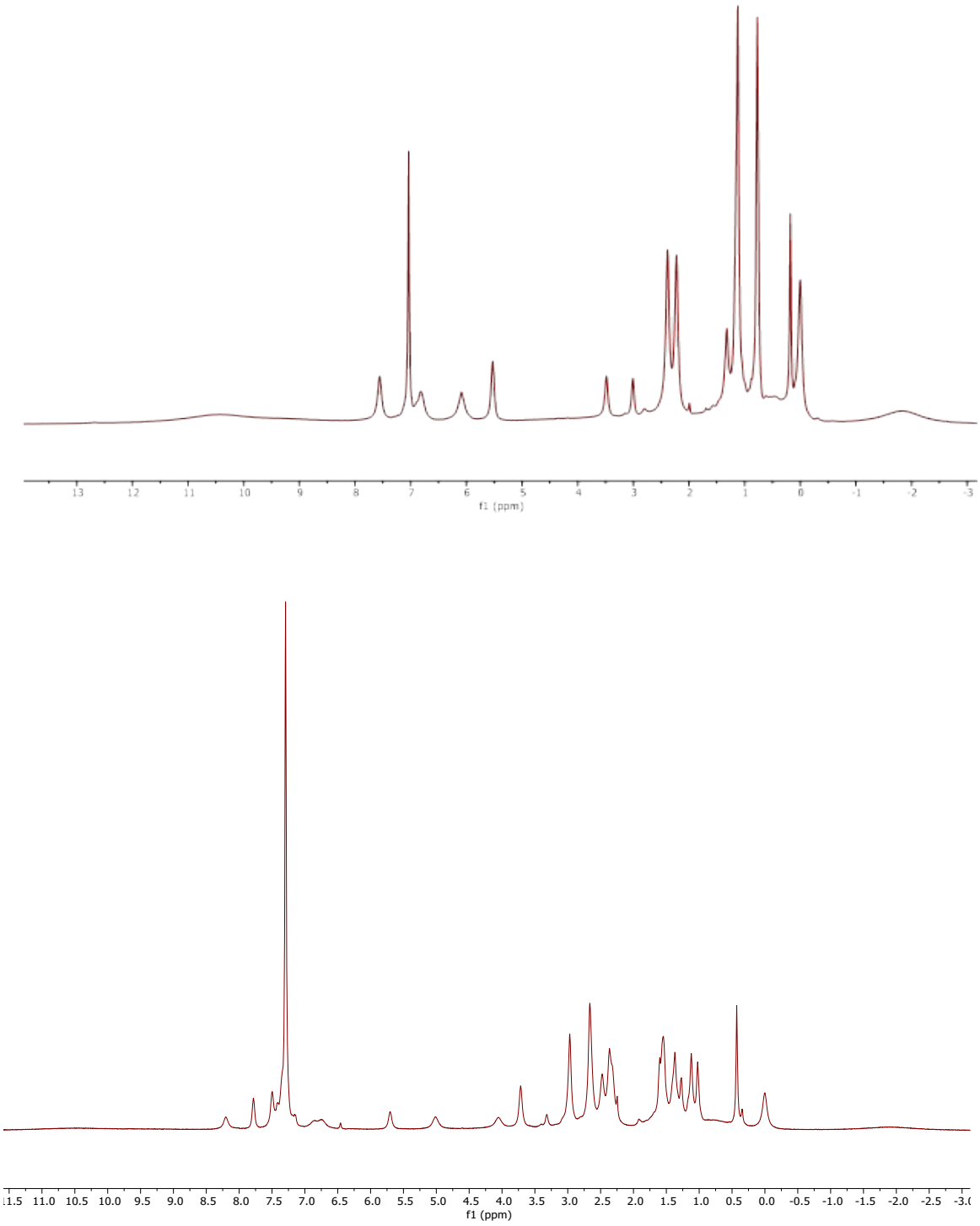

Figure S5. ^{1}H NMR spectrum of complexes [Co^{II}(cAAC)(SS-NHC=S)Cl] (**3a**) (top) and [Co^{II}(cAAC)(SS-NHC=Se)Cl] (**3b**)(bottom) in freshly Na/K-alloy distilled C_6D_6 at room temperature (400 MHz). 15 mg of each sample dissolved in 0.5 mL of C_6D_6.

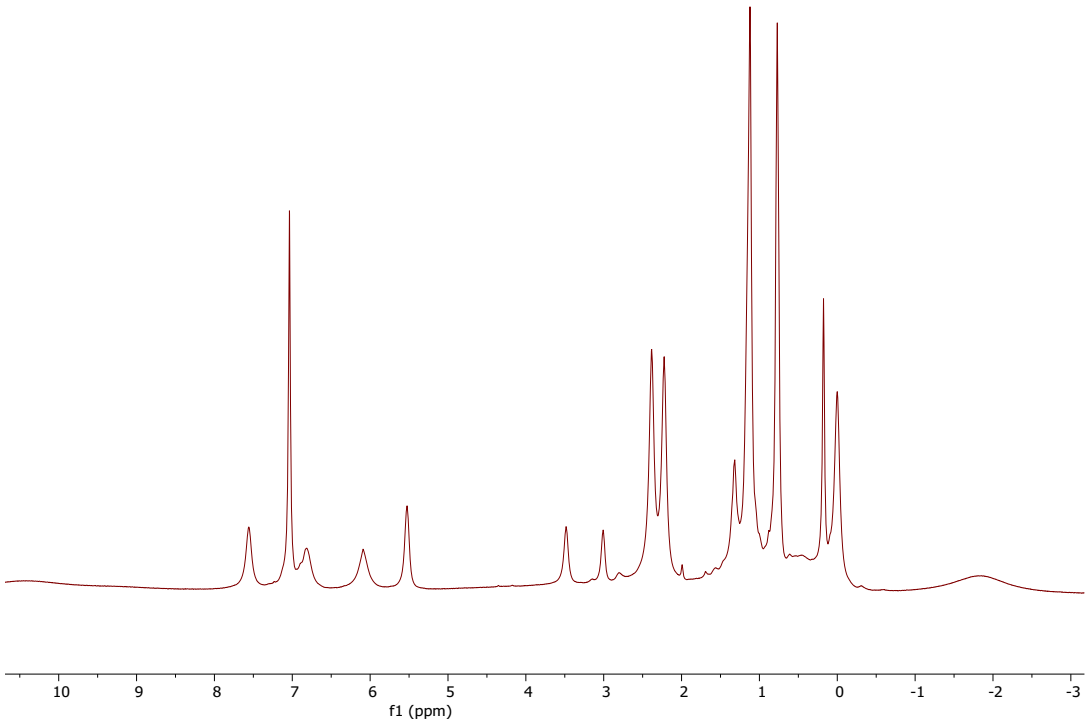

Figure S6. ^{1}H NMR spectrum of complex [Co^{II}(cAAC)(SS-NHC=S)Cl] (**3a**) in freshly Na/K-alloy distilled C_6D_6 at room temperature (400 MHz) (zoomed). 15 mg of sample (**3a**) dissolved in 0.5 mL of C_6D_6.

6. Single-crystal X-ray diffraction

Table S1. Crystal data and structure refinement parameters of complexes [Co^{II}(cAAC)(SS-NHC=S)Cl] (**3a**) and [Co^{II}(cAAC)(SS-NHC=Se)Cl] (**3b**). [SS-NHC=E; E = S (**3a**); Se (**3b**)]

CCDC Deposit	**2374724**	**2453737**	**2450066**
Complex	**3a (at 100 K)**	**3a (at 298 K)**	**3b (at 100 K)**
Shape	**Dark plate**	**Dark long needle**	**Dark block**
Empirical formula	$C_{47}H_{65}ClCoN_3S_3$	$C_{47}H_{65}ClCoN_3S_3$	$C_{47}H_{65}ClCoN_3S_2Se$
Formula weight	862.58	862.58	909.48
Temperature (K)	150 (2)	300(2)	300(2)
Wavelength (Å)	0.71073	0.71073	0.71073
Crystal system	Triclinic	Orthorhombic	Orthorhombic
Space group	*P*-1	*P*bca	$P2_12_12$

Unit cell dimensions	a = 10.9335(16) Å b = 14.234(2) Å c = 18.782(3) Å α = 82.252(5)° β = 79.018(5)° γ = 68.513(4)°	a = 19.056(3) Å b = 18.248(3) Å c = 28.434(5) Å α = 90° β = 90° γ = 90°	a = 17.8203(8) Å b = 26.8357(14) Å c = 10.3438(5) Å α = 90° β = 90° γ = 90°
Volume (Å^3)	2663.3(7)	9887(3)	4946.6(4)
Z	2	8	4
Density (Mg/m^3)	1.076	1.159	1.221
Absorption coefficient (mm^{-1})	0.520	0.56	1.254
F (000)	920	3680	1912
Crystal size (mm^3)	0.508 x 0.345 x 0.220	0.057 x 0.060 x 0.570	0.059 x 0.085 x 0.088
Theta range for data collection (°)	2.155 to 26.466	4.21 to 61.02	3.94 to 60.07
Index ranges	-13<=h<=13, -17<=k<=17, -23<=l<=23	-27<=h<=27, -25<=k<=26, -40<=l<=40	-25<=h<=25, -37<=k<=37, -14<=l<=14
R (int)	0.0909	0.2624	0.1223
Reflections collected	100607	677418	350520
Independent reflections	10928	15092	14485
Completeness to theta = 25.242°	99.4 %	100.0 %	99.9 %
Max. and min. transmission	0.7454 and 0.6266	0.7474 and 0.6753	0.7467 and 0.7120
Number of Restraints	0	19	180
Number of Parameters	512	523	653
Refinement method	Full-matrix least-squares on F^2	Full-matrix least-squares on F^2	Full-matrix least-squares on F^2
Final R indices [I>2sigma(I)]	R_1 = 0.0442, wR_2 = 0.1280	R_1 = 0.0805, wR_2 = 0.1297	R_1 = 0.0612, wR_2 = 0.1416
R indices (all data)	R_1 = 0.0632, wR_2 = 0.1411	R_1 = 0.2076, wR_2 = 0.1796	R_1 = 0.1318, wR_2 = 0.1783
GooF	0.925	1.042	1.028
Largest diff. peak and hole [e·Å^{-3}]	0.542 and -0.387	0.38 and -0.35	1.93 and -0.47

Table S2. Selected bond lengths [Å] for the complexes [Co^{II}(cAAC)(SS-NHC=S)Cl] (**3a**) and [Co^{II}(cAAC)(SS-NHC=Se)Cl] (**3b**):

[Co^{II}(cAAC)(SS-NHC=Se)Cl] (**3b**)	
Co(1)–C(20')	1.99(3)
Co(1)–C(20)	2.12(4)
Co(1)–Cl(1)	2.194(2)
Co(1)–S(3)	2.3160(19)
Co(1)–S(2)	2.3345(16)
S(2)–C(8)	1.683(5)
S(3)–C(9)	1.672(5)
Se(1)–C(7)	1.796(5)
C(8)–C(9)	1.407(7)

[Co^{II}(cAAC)(SS-NHC=S)Cl] (**3a**)

Complex **3a**	100 K/ 298 K
shape	Plate/needle

Solvent of crystallization	THF/hexane
Space group	*P*-1 / *P*bca
Crystal system	Triclinic / Orthorhombic
Co(1)-C(20)	2.003(2)/ 2.016(4)
Co(1)-Cl(1)	2.1909(7)/ 2.1774(14)
Co(1)-S(1)	2.3148(7)/ 2.3088(11)
Co(1)-S(3)	2.3183(7)/ 2.3094(12)
S(1)-C(8)	1.675(2)/ 1.683(3)
S(2)-C(7)	1.644(2)/ 1.638(3)
S(3)-C(9)	1.682(2)/ 1.673(3)
C8–C9	1.414(3) /1.411(4)

Table S3. Selected bond angles [°] for the complexes [Co^{II}(cAAC)(SS-NHC=S)Cl] (**3a**) and [Co^{II}(cAAC)(SS-NHC=Se)Cl] (**3b**):

[Co^{II}(cAAC)(SS-NHC=Se)Cl] (**3b**)	Bond angles (°) (at 100 K)
C(20')–Co(1)–Cl(1)	107.7(6)
C(20)–Co(1)–Cl(1)	117.3(9)
C(20')–Co(1)–S(3)	112.5(7)
C(20)–Co(1)–S(3)	106.3(11)
Cl(1)–Co(1)–S(3)	109.70(11)
C(20')–Co(1)–S(2)	123.2(8)
C(20)–Co(1)–S(2)	117.8(11)

Cl(1)–Co(1)–S(2)	109.26(10)
S(3)–Co(1)–S(2)	93.48(6)
C(8)–S(2)–Co(1)	95.19(18)
C(9)–S(3)–Co(1)	95.5(2)

[Co^{II}(cAAC)(SS-NHC=S)Cl] (**3a**)	Bond angles (°) 100 K / 298 K (shape: plate/needle)

Space group	*P*-1 / *P*bca
C(20)-Co(1)-Cl(1)	115.51(7) / 115.53(12)
C(20)-Co(1)-S(1)	120.24(7) / 123.09(11)
Cl(1)-Co(1)-S(1)	107.67(3) / 105.67(6)

C(20)-Co(1)-S(3)	108.42(6)/ 108.21(10)
Cl(1)-Co(1)-S(3)	108.19(3) / 107.09(7)
S(1)-Co(1)-S(3)	94.28(2) / 94.37(4)
C(8)-S(1)-Co(1)	93.27(8)
C(9)-S(3)-Co(1)	93.17(7)

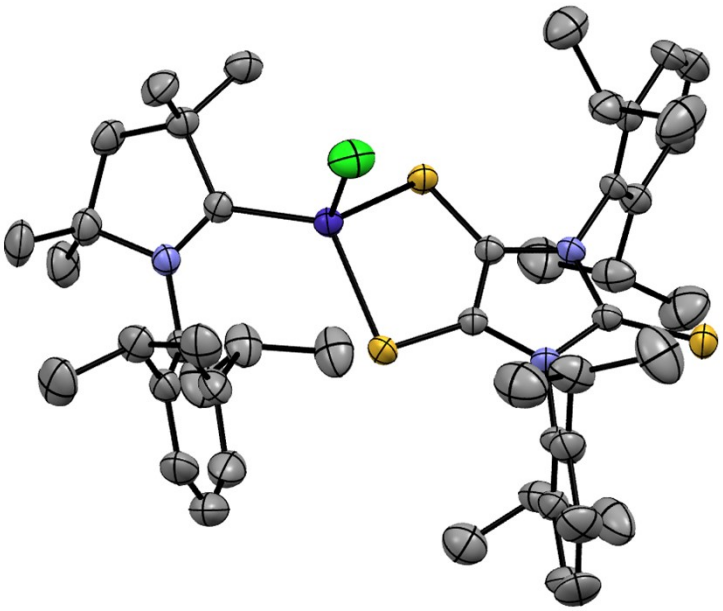

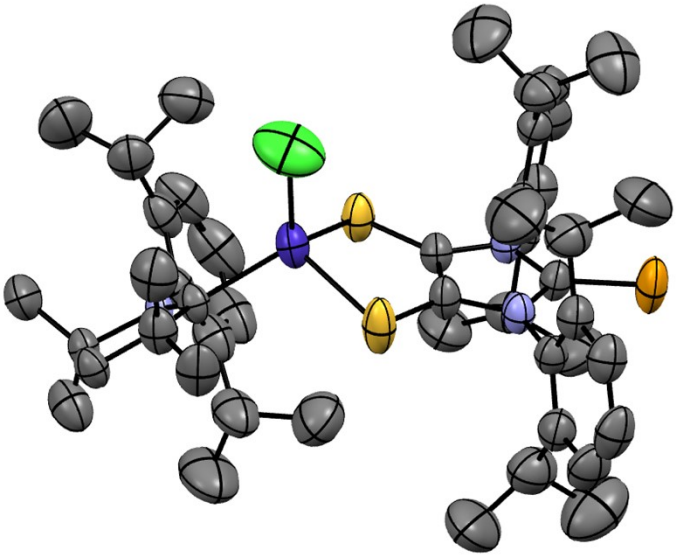

Figure S7. Top: Molecular structure of complex **[Co²⁺(cAAC)(SS-NHC=S)Cl] (3a)** shown as an ellipsoid-ORTEP view.
Bottom: Molecular structure of complex **[Co²⁺(cAAC)(SS-NHC=Se)Cl] (3b)**. Hydrogen atoms are omitted for clarity.

7. Magnetic properties calculations

DC/AC Magnetometry:

Experimental. Direct current (DC) magnetization was measured with a Physical Property Measurement System (PPMS) DynaCool from Quantum Design equipped with a vibrating sample magnetometry (VSM) option. 4.8 mg of the powdered compound **3** was pressed into a polypropylene capsule (QDS-4096-388 from Quantum Design) and attached to the brass half-tube sample holder (QDS-4096-391 from Quantum Design). DC magnetization vs. temperature was measured at a magnetic field of 2500 Oe from 2 K to 50 K in settle mode and from 51 K to 300 K in sweep mode with a 1 K/min heating rate. The temperature step size for signal acquisition was 1 K with a signal averaging time of 10 seconds. Magnetization vs. field was measured at 2, 3, 4, 6, 10, 15, 25, 50, and 300 K up to 7 T with a field step size of 2500 Oe (0.25 T), a signal averaging time of 10 seconds, and a two-fold redundancy per measuring point. At each temperature, the magnetic field was first increased to 7 T and then the field was decreased to zero field again. The superimposed curves for all field scans verified that no reorientation of the sample's powder particles has been induced by the magnetic field. The DC raw data sets have been corrected for diamagnetic contributions (see below).

Alternating current (AC) susceptibility was measured with an ACMS-II option from 10 Hz to 10 kHz at 35 frequencies with log-distribution at 2 K at 0, 500, and 1000 Oe DC field. For the AC measurements, the polypropylene sample capsule was attached to the polymer straw sample holder (AGC2 from Quantum Design) with the help of some polyimide tape. The AC excitation field was 5 Oe with an averaging time per measuring point of 10 seconds. The AC raw data sets have not been corrected for diamagnetic contributions.

Diamagnetic corrections. The measured raw data direct current (DC) magnetic moments have been corrected for the diamagnetic contributions from the atomic closed shells and the bondings according to the incremental method, with the individual values as listed in Table S2 (correction A). A total diamagnetic contribution of about $562.58 \cdot 10^{-6}$ $cm^3\ mol^{-1}$ has been subtracted from the raw data. It should be noted at this point that a somewhat higher diamagnetic correction of $1100 \cdot 10^{-6}$ $cm^3\ mol^{-1}$ instead of $562.58 \cdot 10^{-6}$ $cm^3\ mol^{-1}$ (correction B) would have led to a χT vs. temperature curve with an approximately constant χT values at high temperature around 300 K (see Figure S9). Since the determination of the complete and "true" diamagnetic contribution for a complex molecule as the given one, by the incremental method is a challenging task in general, the actual χT vs. temperature curve of complex 3 might actually lay somewhere in between the cases of correction A and B. In this work, exclusively diamagentic correction A will be considered.

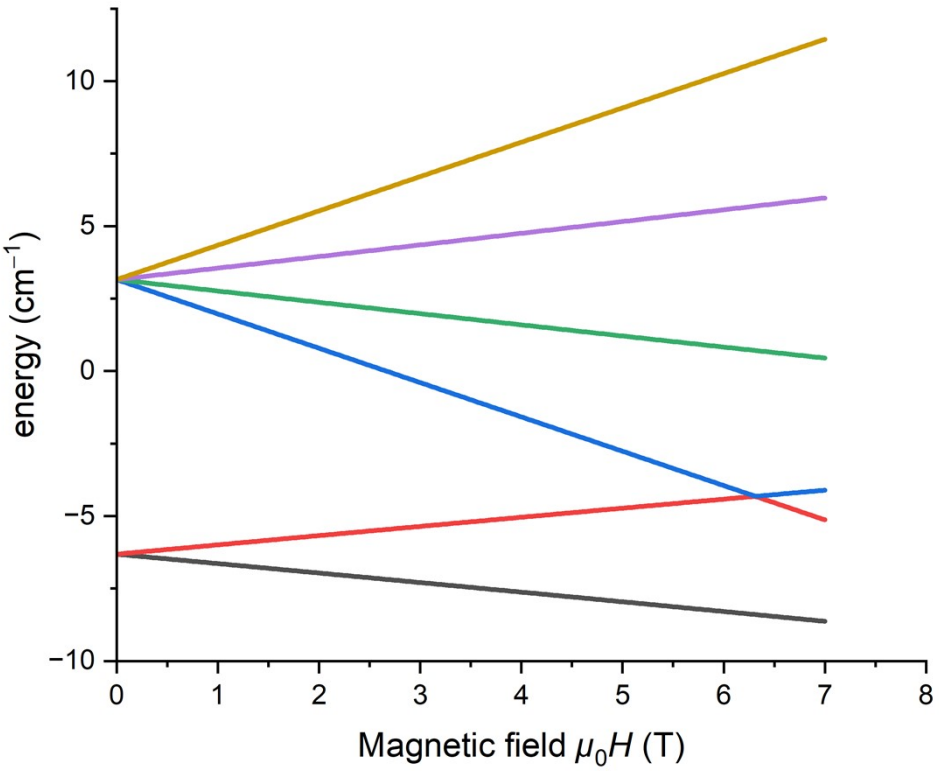

Figure S8. Zeeman diagram (Energy vs magnetic field) of quantum mechanical model **J1EX** that has been refined to the experimental DC magnetometry data sets of complex **3**.

$$\hat{H} = \hat{H}_{\mathrm{SO}} + \hat{H}_{\mathrm{CF}} ++ \hat{H}_{\mathrm{EX}} + \hat{H}_{\mathrm{ZEE}} \qquad \text{(S 1)}$$

with Hamilton operator for spin-orbit coupling (SO), crystal-field interaction (CF), exchange interaction (EX), and Zeeman effect (ZEE).

$$\hat{H}_{\mathrm{SO}} = \sum_{i=1}^{N} \lambda_i \left(\sigma_{\mathrm{SO},i} \vec{\hat{L}}_i \cdot \vec{\hat{S}}_i \right)$$

with spin-orbit coupling constants λ_i, orbital-reduction parameters $\sigma_{SO,i}$, vector operator of total orbital momentum $\vec{\hat{L}}_i$, vector operator of total spin orbital momentum $\vec{\hat{S}}_i$.

$$\hat{H}_{\mathrm{CF}} = \sum_{i=1}^{N} \sum_{k=2,4,6} \sum_{q=-k}^{k} \sigma_i^k B_{ki}^q \theta_k \hat{O}_{ki}^q$$

with crystal-field parameters B_{ki}^{q} ($A_{ki}^{q}\langle r^{k}\rangle_{i}$ in Steven's notation), operator equivalent factors θ_{k} and operator equivalents $\hat{O}_{ki}^{q}$. In this work, the operator equivalent factors are included into the CFPs by setting $B_{ki}^{q} = B'_{ki}^{q}\theta_{k}$.

$$\hat{H}_{\mathrm{EX}} = -2\sum_{i,j \in N,\, i \neq j} \hat{\vec{S}}_{i} \cdot J_{iso} \cdot \hat{\vec{S}}_{j}$$

with scalar isotropic exchange parameter J_{iso}.

$$\hat{H}_{\mathrm{ZEE}} = \mu_{\mathrm{B}} \sum_{i=1}^{N} \left(\sigma_{i}\hat{\vec{L}}_{i} \cdot \bar{\bar{I}} + \hat{\vec{S}}_{i} \cdot \bar{\bar{g}}_{i}\right) \cdot \vec{B}$$

with Bohr magneton μ_{B}, identity matrix $\bar{\bar{I}}$, g-tensor $\bar{\bar{g}}_{i}$ and magnetic induction $\vec{B}$.

Table S4. Diamagnetic correction of complex **3a**.

Atomic diamagnetic contribution to magnetic susceptibility	$25\chi_{C(Ring)} + 22\chi_{C(Open)} + 3\chi_{N(Ring)} + \chi_{Cl} + 3\chi_{S} + 65\chi_{H} + \chi_{Co^{2+}}$
	$[25 \times (6.24) + 22 \times (6.00) + 3 \times (4.61) + (20.1) + 3 \times (15.0) + 65 \times (2.93) + (12.0)] \times (-10^{-6}$ emu mol$^{-1})$
	$= -569.38 \times 10^{-6}$ emu mol^{-1}
Bond diamagnetic contribution to magnetic susceptibility	$3 \times$ (Benzene) $+ 1 \times$ (Pyrrolidine) $+ 3 \times$ (Ar–NR_2) $+ 1 \times$ (Imidazole) $+ 16 \times$ (C_{sp^3}–C_{sp^3}) $+ 22 \times$ (C_{sp^3}–H)
	$[3 \times (-1.4) + 1 \times (0.0) + 3 \times (1.0) + 1 \times (8.0) + 16 \times (0.0) + 22 \times (0.0)] \times (10^{-6}$ emu mol$^{-1})$
	$= +6.8 \times 10^{-6}$ emu mol^{-1}

Total diamagnetic susceptibility correction = Atomic diamagnetic contribution to magnetic susceptibility + Bond diamagnetic contribution to magnetic susceptibility

$= -569.38 \times 10^{-6}$ emu mol^{-1} $+ 6.8 \times 10^{-6}$ emu mol^{-1}

$= -562.58 \times 10^{-6}$ emu mol^{-1}

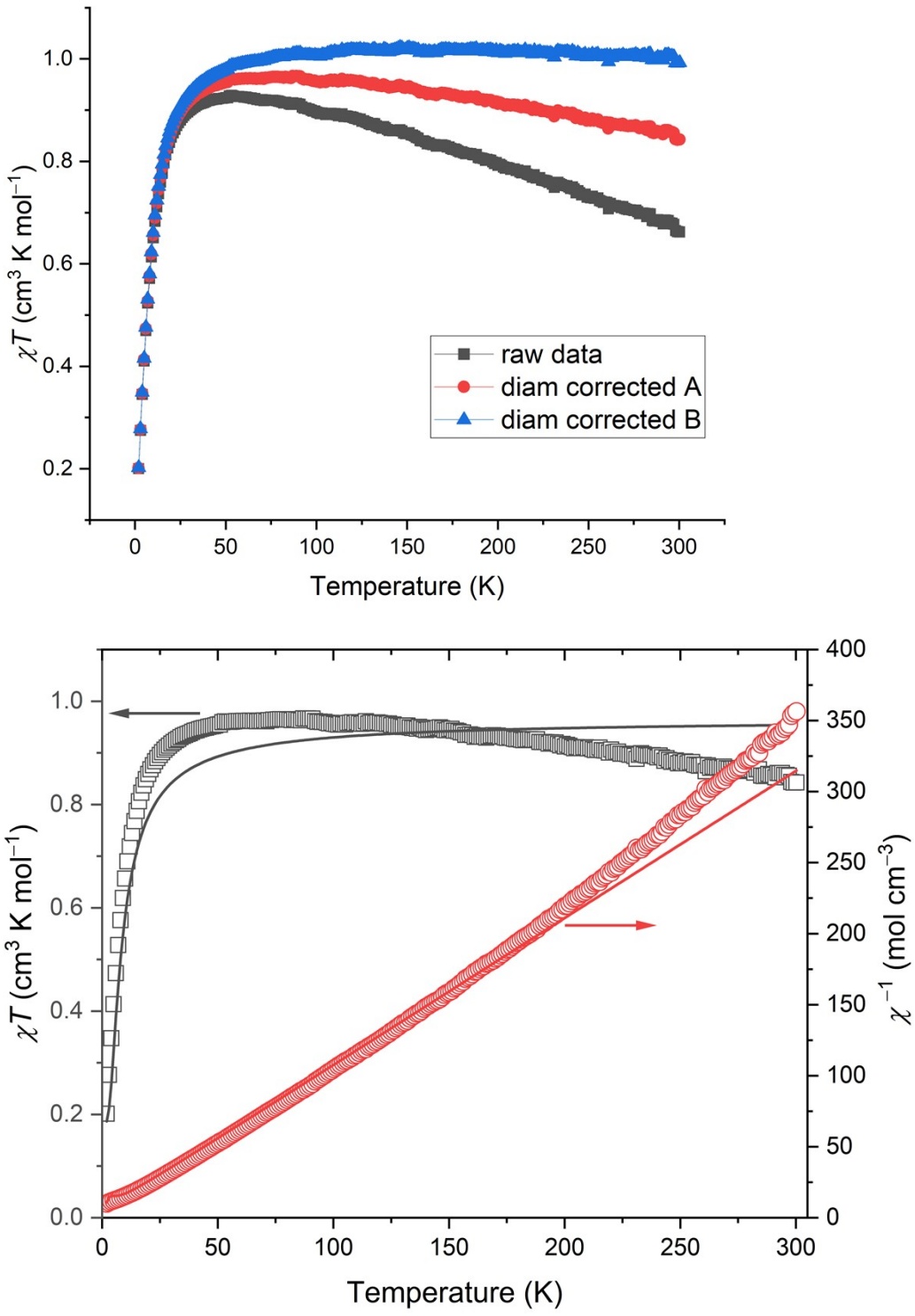

Figure S9. χT vs T plots [top] for complex **3a** without diamagnetic corrections (raw data), with diamagnetic correction A according to the values as listed in Table S2, and with diamagnetic correction B that uses a higher value of diamagentic contribution compared with A (see text). χT vs T (black) and $1/\chi$ vs T (red) plots of **3a** [bottom]. The open symbols represent the experimentally measured values and the solid lines represent the best fits according to the quantum mechanical model J1EX [bottom].

A powdered sample was made by grinding the single crystals of [Co^{II}(cAAC)(SS-NHC=S)Cl] (**3a**) and the temperature-dependent magnetic susceptibility was measured in the temperature range from 2 to 300 K. The measured raw data magnetic moments have been corrected for the diamagnetic contributions from the atomic closed shells and from the bonding according to the incremental method[20a] with the individual values as listed in **Table S4**. The corrected χT vs. temperature curve (**Figure S9, bottom**) slightly increases from about 0.84(1) cm^3 K mol^{-1} at 300 K to a local maximum of about 0.97(1) K at 87 K, before it decreases steeply down to 0.21(1) at 2 K (a more detailed discussion about the diamagnetic correction and its impact on the χT curve can be found in the ESI). For comparison, the spin-only paramagnetic moment of a spin $S = 1$ is $\mu_{eff} = 2.83$ $\mu_{B,}$ which would lead to a χT value of 1 cm^3 K mol^{-1}, that of two spin $S = ½$ (each μ_{eff} = 1.73 μ_B) would lead to a value of 2·0.38 cm^3 K mol^{-1} = 0.75 cm^3 K mol^{-1}, and that of a (hypothetical) isolated orbital momentum $L = 1$ (corresponding to $\mu_{eff} = 1$ μ_B) would lead to a χT value of 0.25 cm^3 K mol^{-1}. The magnetic effective moment (μ_{eff}) of the cobalt(II)iodine unit coordinated three phosphine centre Co(II) ion in the low spin configuration [[$PhBP_3$]Co(II)I] was reported to be 2.85 μ_B. This complex was further reported to be in equilibrium with **a** small percentage of high-spin Co(II) ion. The μ_{eff} values of **3a** and previously reported [[$PhBP_3$]Co(II)I][20b] are significantly lower than those of high spin Co(II) complexes [4.3 and 5.2 μ_B].[21a]

The program package PHI[22a] has been used to set up a quantum mechanical magnetic model based on angular momentum basis states that has been refined to the experimental data sets. A quite simple magnetic model (**named J1EX**) consisting out of an effective total angular momentum $J_e = 1$ (this could equivalently also be considered as effective total spin $S_e = J_e = 1$) together with a refinable isotropic *g*-factor g_{iso} that is capable to account for contributions from orbital momentum turned out to describe the Co(II) magnetic center quite well.

Further, an additional free radical electron is represented by a spin quantum number $S = ½$ only. The isotropic exchange interaction between the Co(II) and the free radical electron is parameterized by the isotropic exchange parameter J_{iso} (see **Equation 1**, **ESI** for detailed description of applied Hamiltonian). The solid lines represent the best fit curves of susceptibility vs temperature (**Figure S9, bottom**) as well as magnetization vs field (**Figure 4**) to the experimentally measured data sets (open symbols). The

isotropic g-factor g_{iso} belonging to the J_e = 1 Co(II) center has been refined to a value of 1.536(2) that corresponds to an effective paramagnetic moment of μ_{eff} = 2.173(2) μ_B. This value is a little bit larger than the theoretical spin-only value for the effective paramagnetic moment of a spin S = 1/2 (μ_{eff} = 1.73 μ_B).

A free Co(II) ion has electronic configuration [Ar]3d^7 (with ^{4}F ground term) and in an ideal tetrahedral coordination the crystal field would cause a level splitting according to e^4t^3 with three unpaired electrons and spin $S = {}^3/_2$. In the ideal tetrahedral crystal field, the ^{4}F term would split into a non-degenerated $^4A_2$, and two $^4T_2$ and $^4T_1$ terms, that means the orbital momentum would be quenched. However, the large total spin quantum number $S = {}^3/_2$ of such a Co(II) in tetrahedral coordination does not agree with the experimental results. Together with the free radical electron with $S = {}^1/_2$, four unpaired S = ½ would contribute to χT with about 4·0.38 cm^3 K mol^{-1} = 1.52 cm^3 K mol^{-1}, that is significantly above the experimentally measured value at 300 K. As a consequence, for the Co(II) that is actually only in a pseudo tetrahedral coordination due to the different ligands (C, Cl, 2·S) a low-spin state is proposed with a total spin quantum number $S = {}^1/_2$. Such a configuration could be obtained already by lowering one of the three t-levels to cause two of the three electrons to be paired. As outlined above, the Co(II) does not only contribute with a paramagnetic moment of a pure S = ½ (1.73 μ_B), but exhibits some additional magnetic moment that is either supposed to originate from some unquenched orbital momentum of the non-ideal tetrahedral coordination or by any other kind of contribution. For instance, also partial excitations from the low-spin configuration to a high-spin configuration (at same Co oxidation state) might play an additional role, or even excitations to Co species of higher oxidation state. Finally, the important low laying energy states of the actual system can quite well be represented by the simplified **model J1EX** with an effective total angular momentum of S_e = J_e = 1 with g_{iso} = 1.536(2). This permanent magnetic moment at the Co(II) center is coupled AFM to the free radical electron. At high temperature, where the magnetic interactions only play a minor role compared to the entropy term, the measured χT originates from the paramagnetic moment of the Co(II) that is slightly larger than that of a S = ½ alone (by additional orbital contributions for instance) plus the paramagnetic moment from the free radical electron with S = ½. Below approximately 50 K, there is a strong reduction of the measured magnetic moment due to the AFM coupling between the effective spin on Co with the spin of the radical electron. The AFM coupling leads to a measured magnetization of only 0.79 μ_B at 2 K and at 7 Tesla that is far below the hypothetical value of two free spin $S = {}^1/_2$ with a saturation magnetization of 2 μ_B.

It was not possible to find a simple reasonable magnetic model that would have been capable to model the decreasing χT vs. temperature curves in the high temperature regime correctly. An alternative magnetic model that makes use of the *TP*-Isomorphism has also been applied. Here, the low-spin $S = ½$ from the Co(II) was coupled with the orbital momentum of a *P* state with $m_L = \pm 1,0$ via a spin-orbit coupling parameter λ_{SO} and an orbital reduction parameter η_{OR}. The S = ½ from the Co(II) was again coupled by isotropic exchange with the free radical electron. However, also this extended model that includes explicitly spin-orbit coupling at the Co(II) center is not capable to model the reducing χT values at high temperature and the residual of the total fit is even slightly worse than that of **model J1EX**. It remains a bit unclear whether the feature of decreasing χT vs temperature curve is a real effect that simply cannot be accounted for by the applied models or whether the diamagnetic contribution is actually larger (as outlined in the ESI).

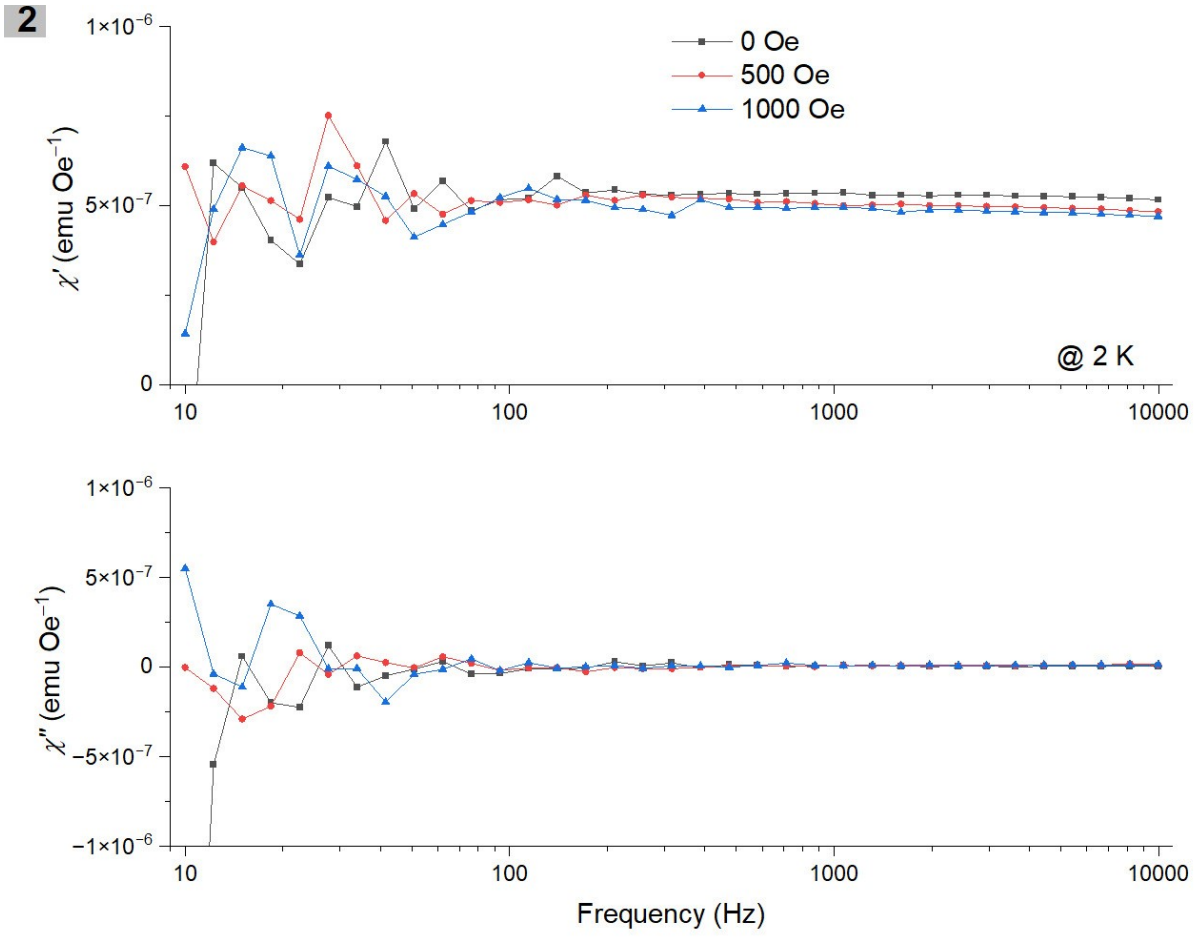

Figure S10. In-phase (χ′) vs. T and out-of-phase (χ″) vs. T plots of complex **3a** at 2 K under different applied DC field.

8. EPR Measurements

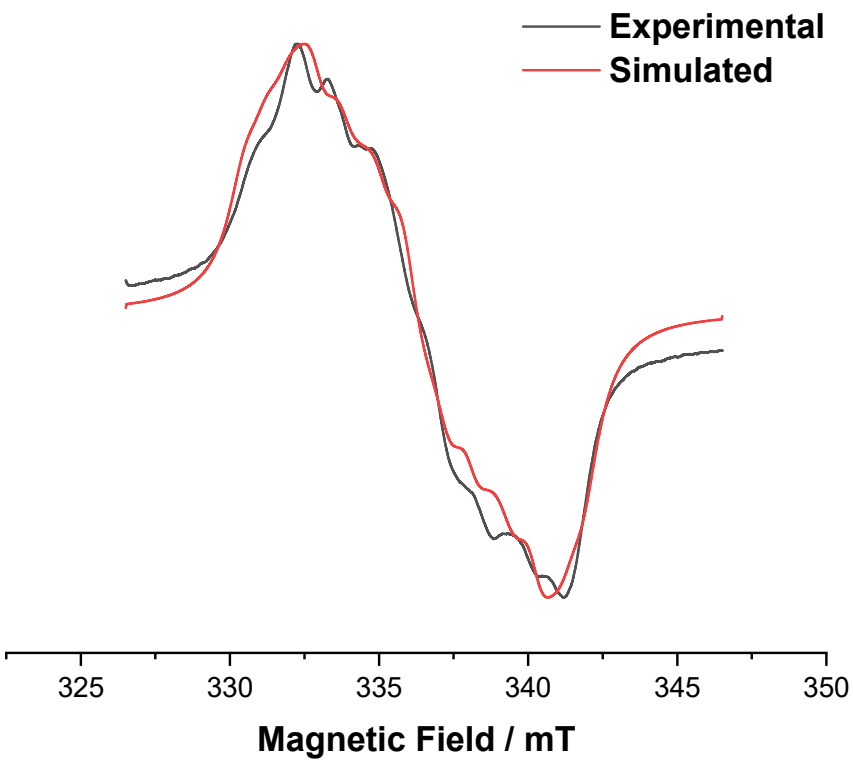

Figure S11. X-Band solid state EPR spectrum (black) of **3a** at room temperature. Red and black lines represent the simulated and the experimental spectra of **3a**, and the simulation is done using EasySpin program.[1] [$\mathbf{g_x}$ = 2.02732, $\mathbf{g_y}$ = 2.00663, $\mathbf{g_z}$ = 1.99043, LWPP (Gaussian broadening) = 0.026615 mT, LWPP (Lorentzian broadening) = 0.809999 mT, $\mathbf{A_x}(^{59}\text{Co})$ = 21.5404 MHz, $\mathbf{A_y}(^{59}\text{Co})$ = 29.3571 MHz, $\mathbf{A_z}(^{59}\text{Co})$ = 20.2722 MHz, X-band experimental frequency = 9.452804 GHz].

$$g_{iso} = \sqrt{\frac{{g_x}^2 + {g_y}^2 + {g_z}^2}{3}} = \sqrt{\frac{2.02732^2 + 2.00663^2 + 1.99043^2}{3}} = 2.008183418$$

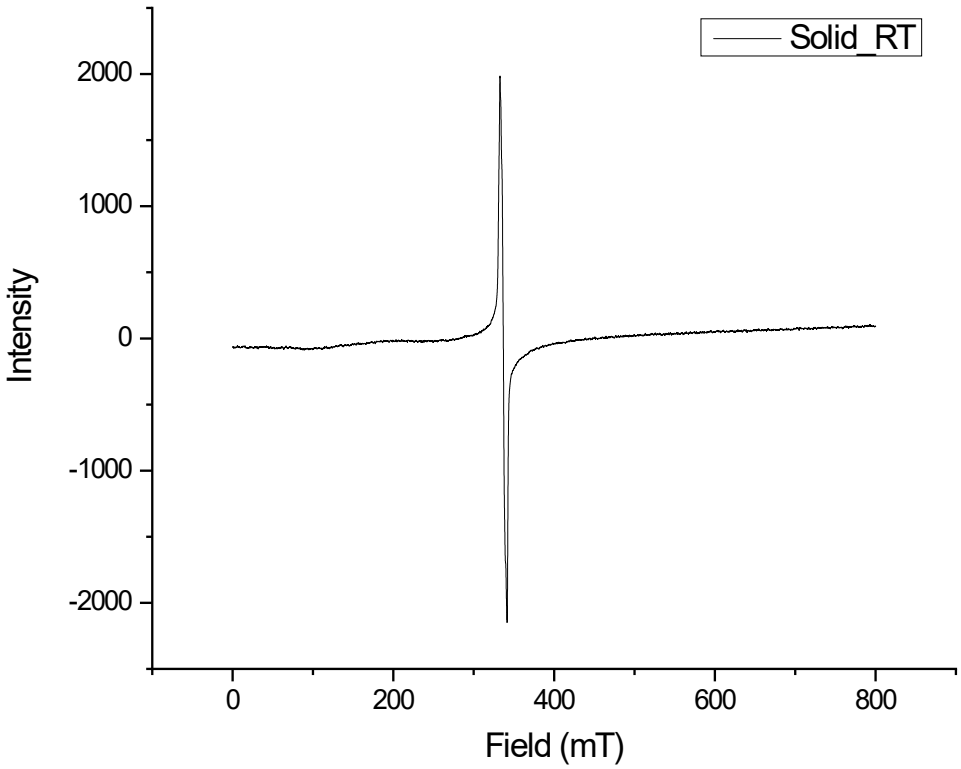

Figure S12. X-Band EPR spectrum of **3** at room temperature in solid-state.

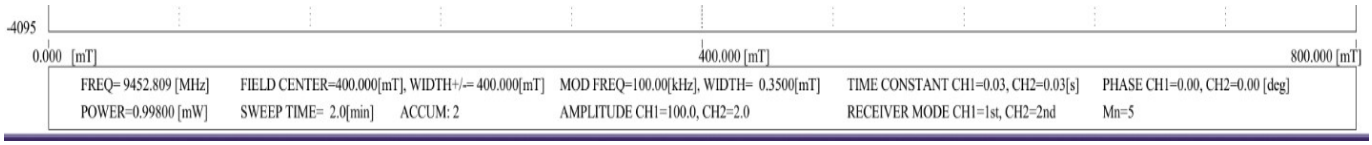

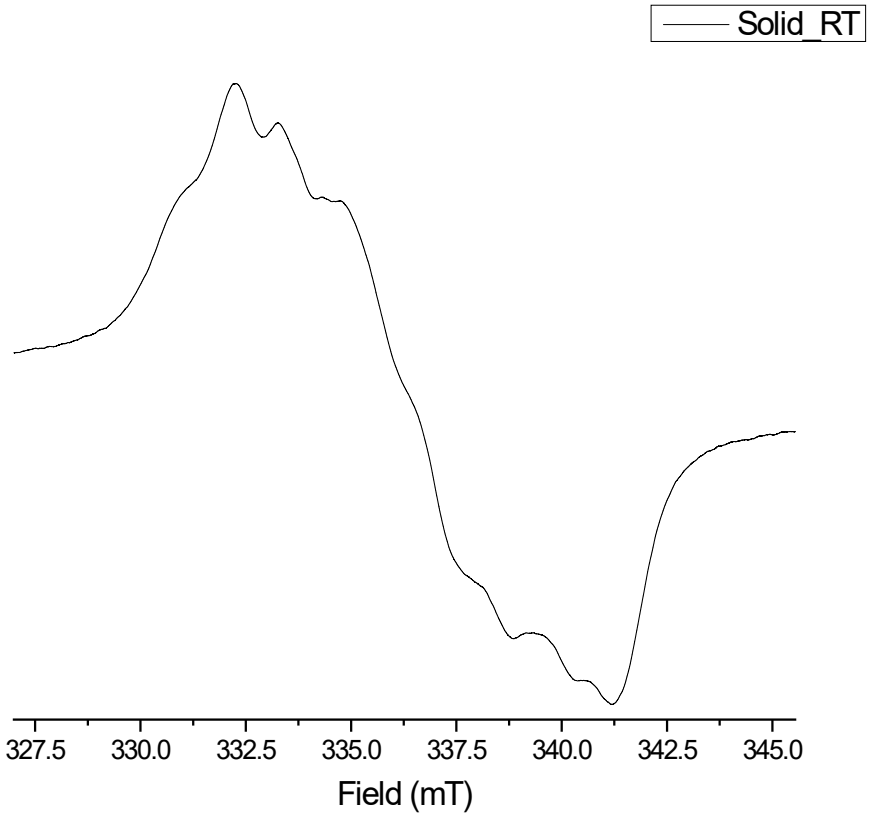

Figure S13. X-Band EPR spectrum of **3** at room temperature in solid-state (326 – 346 mT).

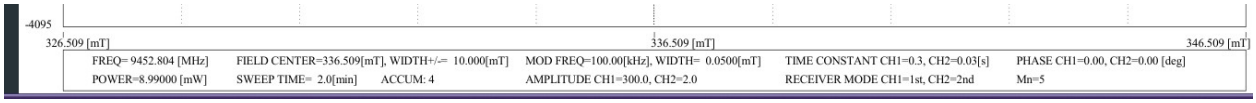

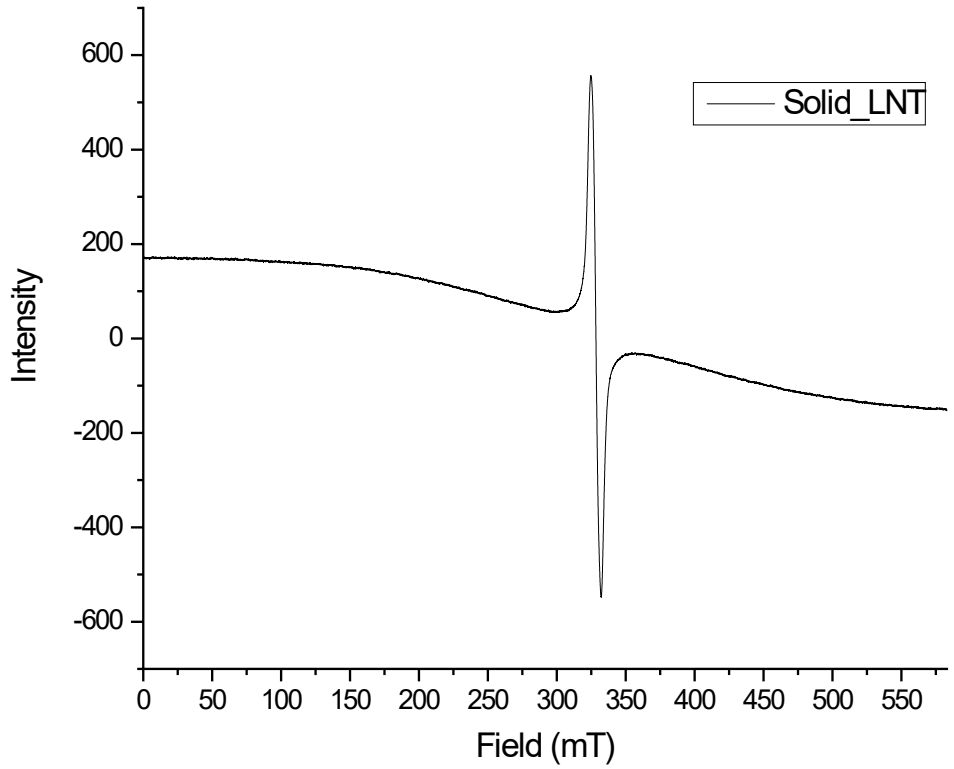

Figure S14. X-Band EPR spectrum of complex (**3**) at 77 K in solid-state (full range, 0-600 mT).

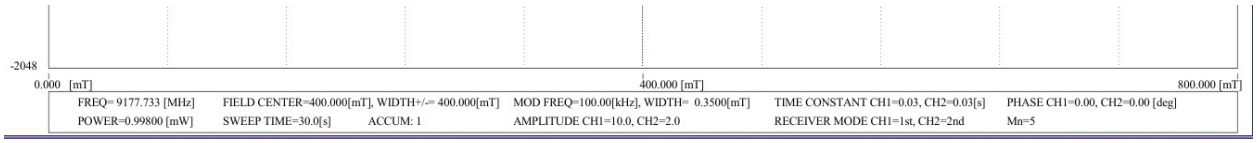

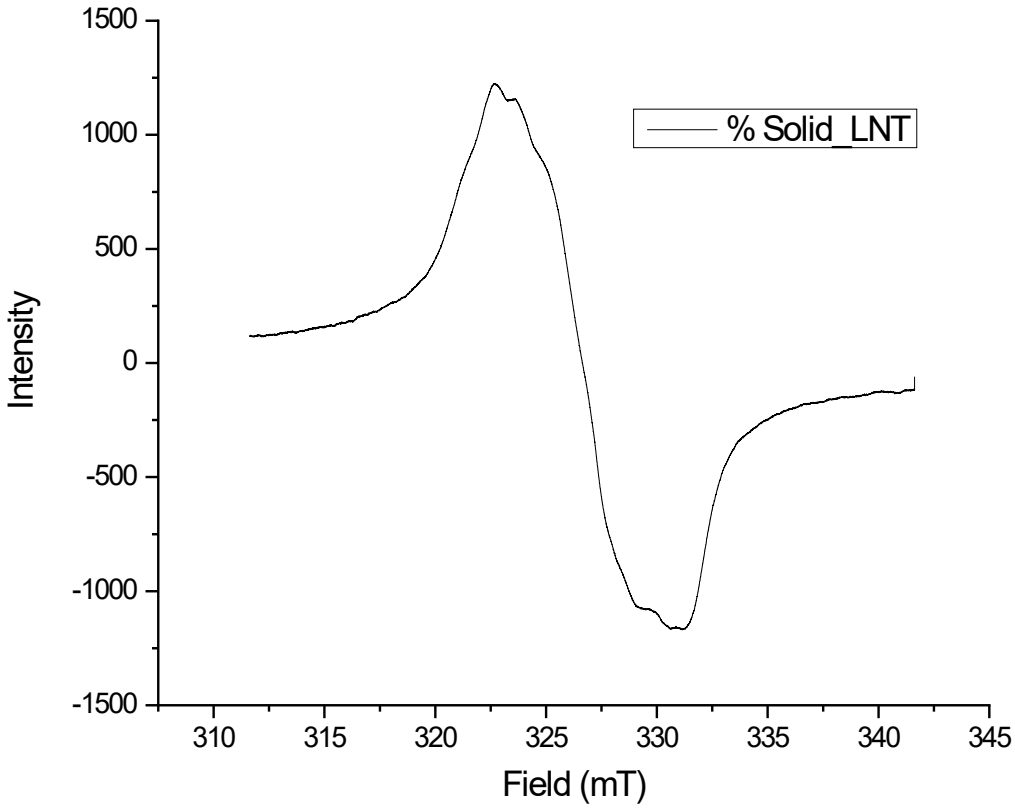

Figure S15. X-Band EPR spectrum of complex **[(cAAC)Co(II)Cl(SS-NHC-S)]** (**3**) at 77 K in solid-state (310 to 342 mT).

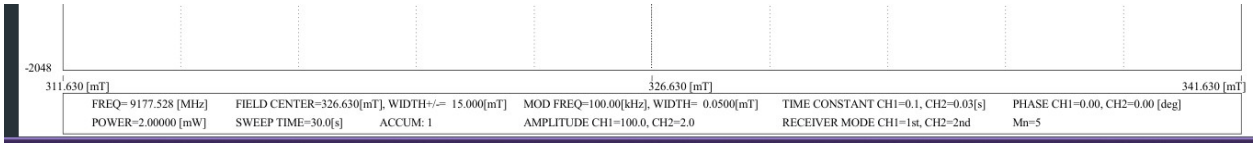

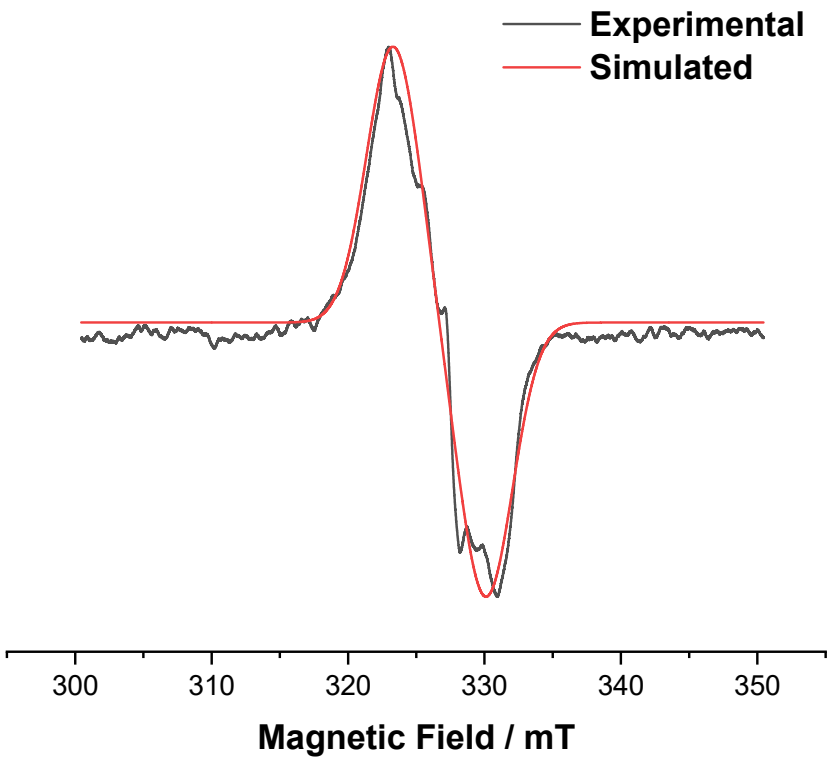

Figure S16. X-band EPR spectrum (black) of the **3a** at liquid nitrogen temperature in THF. Red and black lines represent the simulated and the experimental spectra of **3a** using the EasySpin program. [$\mathbf{g_x}$ = 1.98994, $\mathbf{g_y}$ = 2.0074, $\mathbf{g_z}$ = 2.02272, LWPP (Gaussian broadening) = 3.93383 mT, LWPP (Lorentzian broadening) = 0.0018104 mT, $\mathbf{A_x(^{59}Co)}$ = 2.69687 MHz, $\mathbf{A_y(^{59}Co)}$ = 2.69687 MHz, $\mathbf{A_z(^{59}Co)}$ = 2.69687 MHz, X-band experimental frequency = 9.176029 GHz].

$$g_{iso} = \sqrt{\frac{{g_x}^2 + {g_y}^2 + {g_z}^2}{3}} = \sqrt{\frac{1.98994^2 + 2.0074^2 + 2.02272^2}{3}} = 2.006731352$$

9. TGA measurements

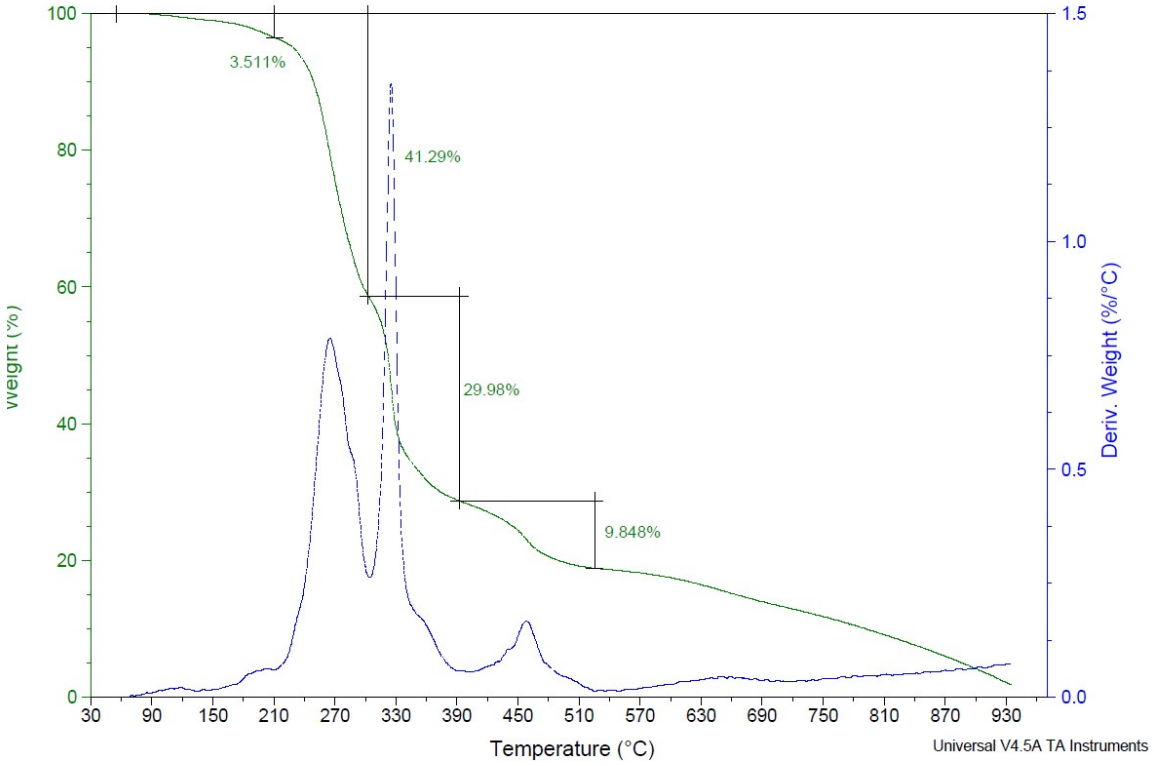

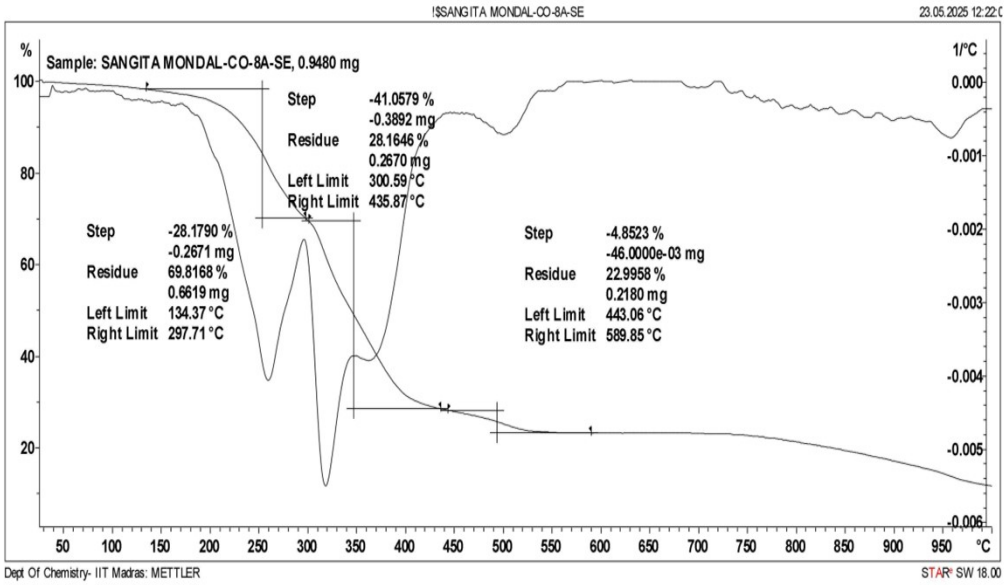

Figure S17. TGA of complexes [Co^{II}(cAAC)(SS-NHC=S)Cl] (**3a**) (top) and [Co^{II}(cAAC)(SS-NHC=Se)Cl] (**3b**) (bottom) in air over 90 min, scanning the temperature from 30 °C to 930 °C.

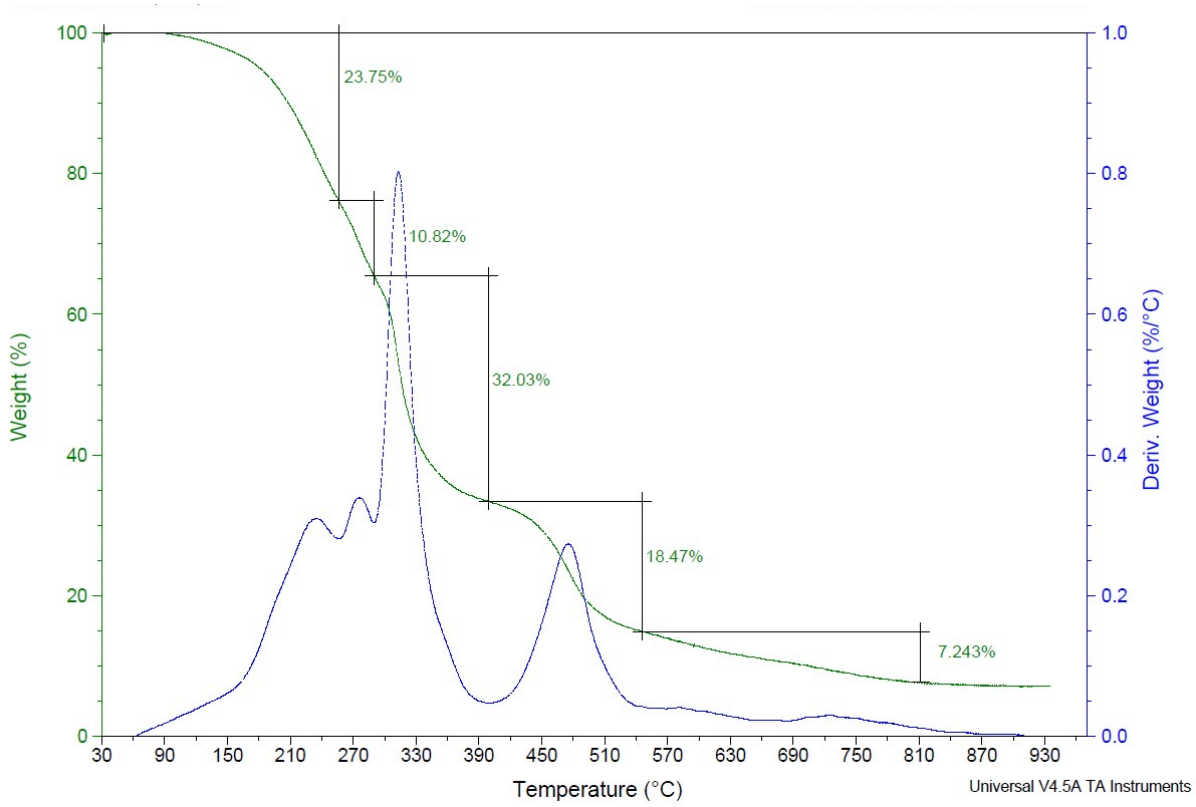

Figure S18. TGA of complex **3a** under N_2 atmosphere, 90 min scanning time in the temperature range from 30 °C to 930 °C.

10. Computational Methods

With the use of DFT, the complex **3′** is optimized using hybrid functional B3LYP[S2-4] along with the dispersion correction term (D3(BJ))[S5-6], and the Ahlrichs triple-ζ-quality basis set def2-TZVPP[S7] using the Gaussian16[S8] package in the gaseous phase. The geometry optimization is favoured by minima on the potential energy surface followed by no negative frequency, with the Dip group in **3** replaced by the methyl group (**3′**) for calculation convenience. The triplet and quintet electronic states have been found to be approximately equally stable with an energy difference of just 2.9 kcal/mol, while the singlet electronic state is destabilized by 26.5 kcal/mol compared to its triplet state. The optimized geometries are shown in Figure S19. The NBO 6.0 program[S9] is used to perform the NBO[S10] calculations of the complexes for Mulliken spin densities.

To study the bonding behaviour of electrons in these complexes, we have adopted the energy decomposition analysis (EDA)[S11] coupled with natural orbital for chemical valence

(NOCV)[S12-13] using the ADF 2020 program package[S14], which gives deep insight into the bond formation process between different fragments. It also gives the flexibility to study the interacting fragment in more than one possible charge and electron configuration. The previously optimized geometries at the B3LYP-D3(BJ)/Def2TZ2P level are used to carry out EDA-NOCV[S15-16] calculations at the same level of theory. ADF (Amsterdam Density Functional) program follows the Morokuma-type energy decomposition method, which involves the breakdown of overall energy into two components, ΔE_{prep} and ΔE_{int}, where E_{prep} gives the energy required to deform the fragments into acquired geometry and valence electronic configuration, while ΔE_{int} is the total interaction energy of those two fragments to form the complex again. ΔE_{int} is further split into four physical components in the ADF output file as,

$$\Delta E_{int} = \Delta E_{elstat} + \Delta E_{Pauli} + \Delta E_{orb} + \Delta E_{disp}$$

The Mulliken Spin density values of complex **3'** over cobalt are 2.600 and 2.633, favouring the presence of approx. three unpaired electrons in the high spin state of the metal centre, which sums up to 92.5% and 65.2% of total alpha-spin density in triplet and quintet states, respectively. The fourth unpaired electron of the quintet state is present majorly over the ligand (SS-NHC=S) with the same spin as in the cobalt centre, as represented by a blue colour in the spin density plot with 28.9% of total α-spin density. Whereas it is present in opposite spin (β-spin) over the SS-NHC=S ligand, resulting in an overall triplet electronic state, as seen by the green colour in the spin density plot and its negative spin density values.

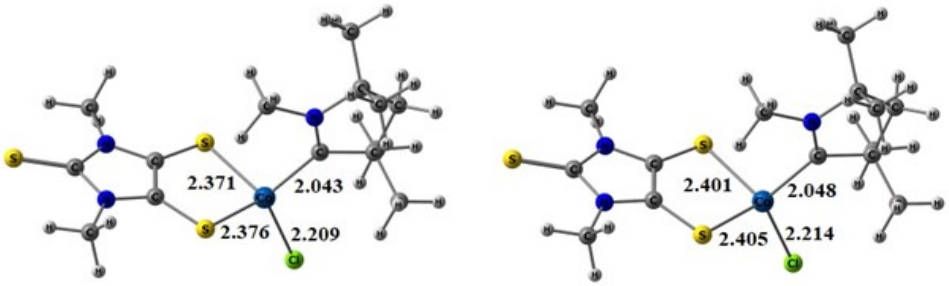

3' (in triplet state) **3'** (in quintet state)

Figure S19. The optimized geometries of complex **3a′** in its triplet (left) and quintet (right) electronic states with selected bond lengths. Dipp is replaced by methyl for calculation purposes.

Table S5. The Mulliken Spin densities of complex **3a′** at B3LYP-D3(BJ)/Def2TZVPP level of theory in its triplet and quintet electronic states for selected atoms. Dipp is replaced by a methyl group over the N-atom.

Complex	Atoms	Spin densities (in triplet state)	Spin densities (in quintet state)
3a′	Co	2.600	2.633
	S, S’	-0.118, -0.118	0.283, 0.283
	C, C’	-0.157, -0.154	0.158, 0.157
	Cl	0.142	0.154

Table S6. The EDA-NOCV results at the B3LYP-D3(BJ)/TZ2P level of theory for complex **3a′ (**in quintet state**)** having (cAAC)(Cl)Co^{+} and (SS-NHC=S)$^{-}$ in quartet and doublet electronic states as interacting fragments. Energies are in kcal/mol. [a]The values in the parentheses show the contribution to the total attractive interaction ΔE_{elec} + ΔE_{orb} +ΔE_{disp}[a], and [b] value in the parentheses shows the contribution to the total orbital interaction.

Energy	Interaction	Complex **3’** (in quintet state)
ΔE_{int}		-176.1
ΔE_{Pauli}		121.1
ΔE_{disp}[a]		-10.2 (3.4%)
ΔE_{elstat}[a]		-181.8 (61.2%)
ΔE_{orb}[a]		-105.2 (35.4%)
$\Delta E_{orb(1)}$[b]	(SS-NHC=S)$^{-}$ → (CAAC)(Cl)Co^{+} σ type e^{-} donation	-48.6 (46.2%)
$\Delta E_{orb(2)}$[b]	(SS-NHC=S)$^{-}$ → (CAAC)(Cl)Co^{+} σ type e^{-} donation	-27.3 (26.0%)
$\Delta E_{orb(3)}$[b]	(SS-NHC=S)$^{-}$ ↔ (CAAC)(Cl)Co^{+} π e^{-} donation	-5.2 (4.9%)
$\Delta E_{orb(rest)}$[b]		-24.1 (22.9%)

The Optimized Coordinate of Co-complex (3a′) at B3LYP-D3(BJ)/TZVPP

Cu-complex (**3a′**) in singlet spin multiplicity

E = -3749.7913913 hf

27	0.034625000	0.186325000	-0.124800000
17	-0.500592000	2.173174000	0.643157000
16	-0.758639000	0.522588000	-2.188061000
16	-5.282035000	0.019832000	0.837987000
16	-0.288676000	-2.008771000	-0.043849000
7	-2.908268000	-1.260024000	0.513013000
7	-3.185985000	0.452563000	-0.833320000
7	2.811000000	-0.327857000	-0.678876000
6	-3.797804000	-0.256888000	0.167110000
6	-1.951879000	-0.095402000	-1.141195000
6	-1.780521000	-1.196260000	-0.270078000
6	1.927242000	0.170515000	0.140601000
6	4.220030000	-0.416617000	-0.158189000
6	3.993964000	-0.121974000	1.330320000
1	3.955321000	-1.062202000	1.881087000
1	4.799873000	0.475179000	1.752456000
6	2.626938000	0.590426000	1.426973000
6	4.780403000	-1.820815000	-0.375432000
1	5.725725000	-1.908893000	0.159771000
1	4.975792000	-2.030645000	-1.426375000
1	4.099636000	-2.577600000	0.014315000
6	5.103637000	0.616892000	-0.859804000
1	6.109647000	0.575538000	-0.442930000
1	4.721819000	1.626364000	-0.728950000
1	5.181452000	0.413779000	-1.927615000
6	2.796272000	2.122100000	1.446227000
1	3.384421000	2.396482000	2.323366000

1	1.831145000	2.615690000	1.493392000
1	3.316443000	2.486107000	0.561780000
6	1.840591000	0.149088000	2.663959000
1	2.407484000	0.391449000	3.564438000
1	1.657945000	-0.925775000	2.653251000
1	0.882241000	0.663101000	2.714000000
6	2.533311000	-0.806786000	-2.026541000
1	1.492821000	-0.630902000	-2.265853000
1	3.168680000	-0.283215000	-2.739530000
1	2.735563000	-1.873824000	-2.091356000
6	-3.729269000	1.673865000	-1.391985000
1	-3.120093000	1.953809000	-2.245266000
1	-4.762089000	1.507137000	-1.688331000
1	-3.692992000	2.466633000	-0.646978000
6	-3.138767000	-2.199985000	1.589222000
1	-3.599377000	-1.675970000	2.422430000
1	-3.808294000	-2.996784000	1.266392000
1	-2.180495000	-2.620281000	1.882369000

Co-complex (**3a′**) in triplet spin multiplicity

E = -3749.8335964 hf

27	0.605645000	1.170701000	-0.028655000
17	1.140050000	3.314301000	-0.017610000
16	-0.998001000	0.737698000	-1.727312000
16	-5.808920000	-1.050985000	0.084644000
16	-0.806371000	0.364223000	1.697242000
7	-3.376318000	-0.394990000	1.125696000
7	-3.502538000	-0.142915000	-1.050139000
7	2.235919000	-1.346475000	-0.217984000
6	-4.237816000	-0.530389000	0.053853000
6	-2.225539000	0.217318000	-0.690929000
6	-2.145122000	0.058623000	0.715140000
6	2.232719000	-0.065349000	-0.010319000
6	3.569812000	-2.040092000	-0.130907000

6	4.441992000	-0.926057000	0.465198000
1	4.616542000	-1.124023000	1.522296000
1	5.413700000	-0.876303000	-0.022283000
6	3.641069000	0.390187000	0.305727000
6	3.476482000	-3.259505000	0.781933000
1	4.473494000	-3.674102000	0.929020000
1	2.851867000	-4.044307000	0.355752000
1	3.076248000	-2.984962000	1.757882000
6	4.017100000	-2.448103000	-1.536250000
1	5.003516000	-2.908039000	-1.482455000
1	4.078926000	-1.583358000	-2.194552000
1	3.339145000	-3.174507000	-1.983694000
6	4.145101000	1.250509000	-0.866834000
1	5.169269000	1.568522000	-0.666482000
1	3.522935000	2.135487000	-0.985265000
1	4.139902000	0.695913000	-1.805636000
6	3.664830000	1.217117000	1.597585000
1	4.697193000	1.466424000	1.849268000
1	3.241230000	0.654214000	2.430903000
1	3.102701000	2.141024000	1.480908000
6	1.046057000	-2.132784000	-0.526027000
1	0.263921000	-1.471553000	-0.880577000
1	1.274901000	-2.863601000	-1.298268000
1	0.703465000	-2.653125000	0.366903000
6	-4.003703000	-0.113019000	-2.409294000
1	-3.916067000	0.895765000	-2.809236000
1	-3.420767000	-0.789126000	-3.033258000
1	-5.043266000	-0.423093000	-2.388402000
6	-3.721412000	-0.674306000	2.504755000
1	-4.760640000	-0.985062000	2.532153000
1	-3.081084000	-1.464855000	2.893548000
1	-3.576588000	0.221439000	3.106542000

Co-complex (**3a′**) in quintet spin multiplicity

E = - -3749.8289655 hf

27	0.611696000	1.186953000	-0.038227000
17	1.166305000	3.330425000	-0.022890000
16	-1.019617000	0.781522000	-1.757552000
16	-5.780897000	-1.076060000	0.097091000
16	-0.804537000	0.385289000	1.727612000
7	-3.352801000	-0.391670000	1.130084000
7	-3.487977000	-0.142331000	-1.043655000
7	2.215235000	-1.345877000	-0.246035000
6	-4.216067000	-0.537931000	0.061460000
6	-2.215239000	0.235959000	-0.690392000
6	-2.127963000	0.075524000	0.718810000
6	2.229868000	-0.068016000	-0.023980000
6	3.533555000	-2.065035000	-0.135787000
6	4.414718000	-0.970182000	0.483677000
1	4.569965000	-1.179872000	1.541493000
1	5.394396000	-0.932455000	0.011314000
6	3.638148000	0.360827000	0.323136000
6	3.396713000	-3.286277000	0.768995000
1	4.381238000	-3.723832000	0.932685000
1	2.762765000	-4.054859000	0.327179000
1	2.984076000	-3.007381000	1.738514000
6	4.001208000	-2.474733000	-1.533841000
1	4.976589000	-2.955366000	-1.462713000
1	4.094298000	-1.607761000	-2.185590000
1	3.317693000	-3.184408000	-1.999415000
6	4.176174000	1.224883000	-0.831480000
1	5.200617000	1.526928000	-0.609049000
1	3.568267000	2.119443000	-0.953114000
1	4.180945000	0.679111000	-1.775483000
6	3.649340000	1.175779000	1.622796000
1	4.679968000	1.408817000	1.896142000
1	3.202073000	0.611974000	2.442996000
1	3.102290000	2.108606000	1.503626000

6	1.014753000	-2.103260000	-0.585355000
1	0.266115000	-1.426582000	-0.982826000
1	1.250292000	-2.854923000	-1.334946000
1	0.622651000	-2.595456000	0.303185000
6	-3.996255000	-0.113216000	-2.400730000
1	-3.940580000	0.901740000	-2.790570000
1	-3.394767000	-0.764337000	-3.033105000
1	-5.025936000	-0.454326000	-2.378884000
6	-3.691398000	-0.676642000	2.510152000
1	-4.722451000	-1.013164000	2.538116000
1	-3.030383000	-1.449325000	2.899720000
1	-3.568799000	0.223514000	3.110033000

…….

11. Ab initio and CASSSCF calculations

Computational Estimation of the ground state spin in 3

Table S7. Ground state total energy for different spin multiplicities (a.u.) of **3** (neutral)

DFT	Spin	Absolute Energy (a.u.)	Relative Energy (a.u.)	Relative Energy (cm^{-1})
B3LYP	$S = 2$	-5030.552003098	0.0752695780	16519.8
	$S = 1$	-5030.627272676	0.0	0.0
	$S = 0$	-5030.620069042	0.0072036346	1581.0
PBE	$S = 2$	-5028.547556817	0.0208812998	4582.9
	$S = 1$	-5028.568438117	0.0	0.0
	$S = 0$	-5028.556874654	0.0115634625	2537.9
TPSS0	$S = 2$	-5032.106480389	0.0385204685	8454.3
	$S = 1$	-5032.145000857	0.0	0.0
	$S = 0$	-5032.139323636	0.0056772209	1246.0
wB97	$S = 2$	-5031.912033118	0.0325695550	7148.2
	$S = 1$	-5031.944602673	0.0	0.0
	$S = 0$	-5031.939171898	0.0054307757	1191.9

All DFT calculations predict ground state spin S=1.

Table S8. Loewdin spin population analysis on the main atoms of **3**, *S* =1. The atoms with dominant spin density are highlighted.

Atom	nr	B3LYP	PBE	TPSS0	wB97
		Spin	Spin	Spin	Spin
Co	1	2.465225	2.128221	2.584593	2.516573
Cl	2	0.135012	0.172565	0.102740	0.133755
S	3	-0.093077	-0.008924	-0.123074	-0.115886
S	4	-0.190287	-0.151876	-0.197130	-0.189863
S	5	-0.084994	-0.018649	-0.109327	-0.099513
N	6	-0.010147	-0.011270	-0.006043	0.003249
N	7	-0.005273	-0.009591	-0.000120	0.010486
N	8	0.004989	0.001507	0.005402	0.005709
C	18	-0.032391	-0.029681	-0.031728	-0.028529
C	19	-0.127384	-0.084482	-0.140533	-0.156278
C	20	-0.131643	-0.083455	-0.147197	-0.163370
C	33	0.001063	0.001374	0.001206	0.001335
C	41	0.000794	0.000859	0.000914	0.001326
C	42	0.054575	0.068348	0.047040	0.062844
C	43	0.004098	0.005818	0.003577	0.003791
C	44	0.003145	0.005086	0.002639	0.002821
C	47	0.007740	0.011079	0.006853	0.007702

If the ground spin state on Co were S=1/2, there would be only one (1) unpaired electron. If the ground spin state on Co were S=3/2, there would be only three (3) unpaired electrons.

However, as we note in Table S8, the spin population analysis predicts about 2.5 unpaired electrons on Co for the ground S=1 state. This indicates that Co is in its high spin state S=3/2.

We also note the opposite signs of the spin population on the Co and ligand in **3** (Table S8). This indicates an antiferromagnetic spin alignment between the Co and radical: 3/2 - 1/2=1.

Multireference calculations for 3a

We used OpenMOLCAS, CASSCF, and CASPT2 methods to compute the low-lying energy structure for **3**. Seven states with S=2 and seven states with S=1 were optimized within the multiconfigurational self-consistent field method (CASSCF) and mixed further by spin-orbit interaction in restricted state interaction (RASSI). The XMS-CASPT2 method included dynamic electron correlation. The resulting spin-orbit eigenfunctions express the compound's spin and magnetic moments and compute its magnetic properties.

ANO-RCC basis sets described all atoms. Co, S, N, and closest C atoms to the Co were described by VTZP basis set contractions, while distant atoms acquired VDZ basis set contraction. RI/CD decomposition of the bielectronic integrals method allowed for a significant speedup in the calculation.

Three active spaces were used:

1) **CAS(8in6)** consists of seven electrons in five Co-3d orbitals ($3d^7$) and one additional electron of the radical in one additional orbital.
2) **CAS(10in8)** consists of CAS(8in6)+ one doubly occupied orbital (HOMO-1) and one empty orbital (LUMO-1)
3) **CAS(12in10)** consists of CAS(8in6)+ two doubly occupied orbitals (HOMO-1 and HOMO-2) and two empty orbitals (LUMO-1 and LUMO-2)

Table S9. Low-lying energy structure on **3a** in different computational models, in cm^{-1}, as predicted by CASSCF/CASPT2/RASSI-SO.

CAS-8in6		CAS-10in8		CAS-12in10		CAS-14in12	
CASSCF	CASPT2	CASSCF	CASPT2	CASSCF	CASPT2	CASSCF	CASPT2
0.0	0.0	0.0	0.0	0.0	0.0	0.0	0.0
17.8	11.7	17.8	11.5	18.5	11.8	18.4	12.1
24.8	19.4	24.8	19.6	25.7	20.3	25.8	20.7
639.6	1783.0	658.3	1812.7	724.9	1878.4	761.1	1873.6
642.5	1783.9	661.2	1813.6	727.6	1879.5	763.7	1874.6
660.6	1811.7	679.4	1840.6	748.2	1908.0	785.3	1904.1
677.9	1822.2	696.7	1851.4	765.7	1920.2	802.6	1916.5
680.8	1828.9	699.6	1857.8	769.2	1926.9	806.5	1923.4
3029.3	4187.0	3040.9	4255.3	3083.2	4325.8	3087.4	4311.7
3042.5	4202.4	3054.0	4269.5	3097.2	4343.8	3101.7	4330.9
3053.0	4203.1	3063.8	4271.4	3104.6	4346.7	3107.7	4333.7
3138.4	4280.0	3148.4	4344.0	3188.7	4427.3	3191.6	4416.5
3153.7	4296.7	3165.2	4362.8	3207.1	4435.9	3212.1	4422.8
3199.7	4318.8	3206.5	4384.5	3244.9	4499.8	3244.8	4511.6
3270.5	4381.5	3277.0	4446.1	3310.3	4562.4	3308.6	4573.1
3303.9	4404.0	3309.7	4470.0	3344.2	4598.5	3342.1	4612.8
3819.5	5140.0	3822.6	5156.0	3849.6	5167.1	3849.6	5161.7
3837.1	5164.1	3840.5	5178.2	3865.6	5182.2	3865.6	5174.8
3912.9	5210.6	3916.1	5225.3	3938.6	5233.8	3938.0	5228.1
4399.7	6462.4	4415.9	6531.9	4491.5	6597.7	4509.3	6604.5
4401.9	6467.9	4418.2	6537.3	4493.1	6604.8	4510.9	6611.2
4520.2	6534.3	4537.0	6604.8	4630.6	6678.1	4651.7	6697.2
4548.4	6574.4	4565.4	6643.1	4656.8	6727.0	4678.3	6741.7
4577.2	6583.8	4594.5	6653.2	4695.4	6732.7	4718.8	6751.4
4905.2	6663.1	4913.5	6738.1	4912.6	6789.8	4918.1	6804.3
4961.0	6711.2	4969.7	6787.1	4969.1	6834.6	4975.6	6850.2
4989.4	6733.3	4997.8	6810.1	5000.2	6853.3	5006.4	6878.7
5092.2	7384.7	5104.6	7458.5	5090.2	7474.8	5098.7	7492.0
5130.8	7398.8	5142.4	7472.9	5129.4	7489.7	5137.6	7506.4
5172.4	7438.7	5184.4	7511.9	5183.9	7538.4	5194.2	7556.2

Table S10. Main values of the *g* tensor for the ground state within the formalism of pseudospin $S = 1$ for the **3a**. Zero-field splitting parameters are also listed.

	CAS-8in6		CAS-10in8		CAS-12in10		CAS-14in12	
	CASSCF	CASPT2	CASSCF	CASPT2	CASSCF	CASPT2	CASSCF	CASPT2
	Main values of the *g* tensor for the ground $S = 1$							
g_x	2.4844	2.3773	2.4839	2.3758	2.4838	2.3748	2.4843	2.3752
g_y	2.4384	2.3140	2.4373	2.3105	2.4378	2.3077	2.4377	2.3092
g_z	2.2379	2.1915	2.2376	2.1890	2.2312	2.1828	2.2318	2.1807
g_{iso}	2.3893	2.2956	2.3887	2.2931	2.3868	2.2898	2.3871	2.2898
	Zero-Field Splitting parameters, *D*, *E* for the ground $S = 1$							
D	21.3129	15.5237	21.3073	15.5409	22.1008	16.0548	22.1195	16.4098
E	-3.4671	-3.8688	-3.5307	-4.0354	-3.5987	-4.2548	-3.6958	-4.3078

$$g_{iso} = \sqrt{\frac{g_x^2 + g_y^2 + g_z^2}{3}}$$

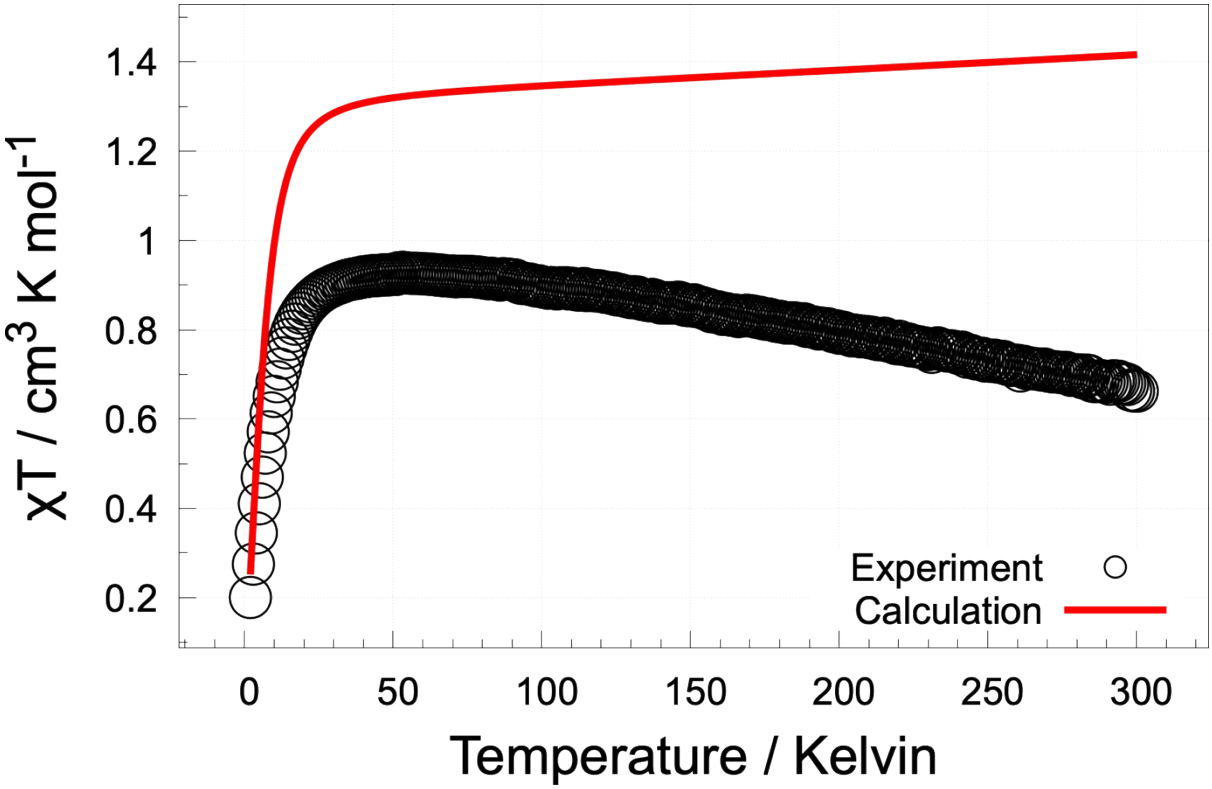

Figure S20. Comparison between measured and ab initio calculated magnetic susceptibility (XT) for **3a**, using the CASPT2, CAS(14in12) results.

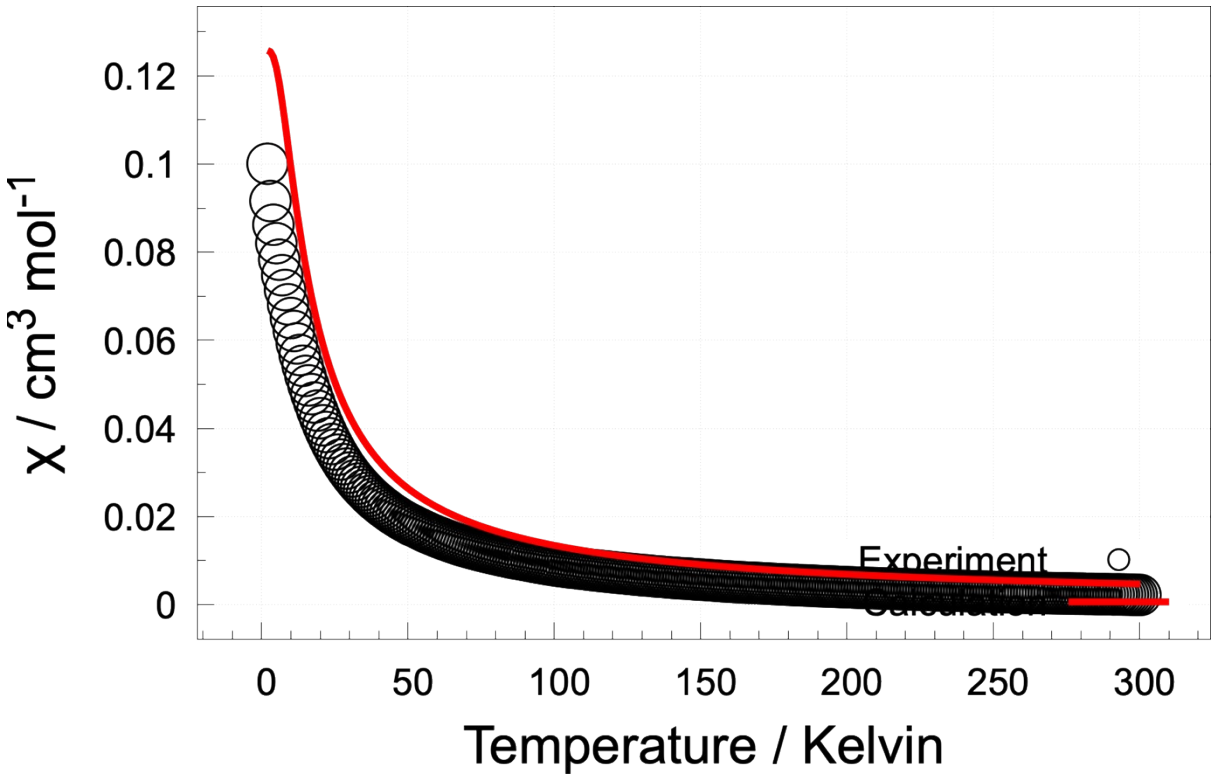

Figure S21. Comparison between measured and ab initio calculated magnetic susceptibility (X) for **3a**, using the CASPT2, CAS(14in12) results.

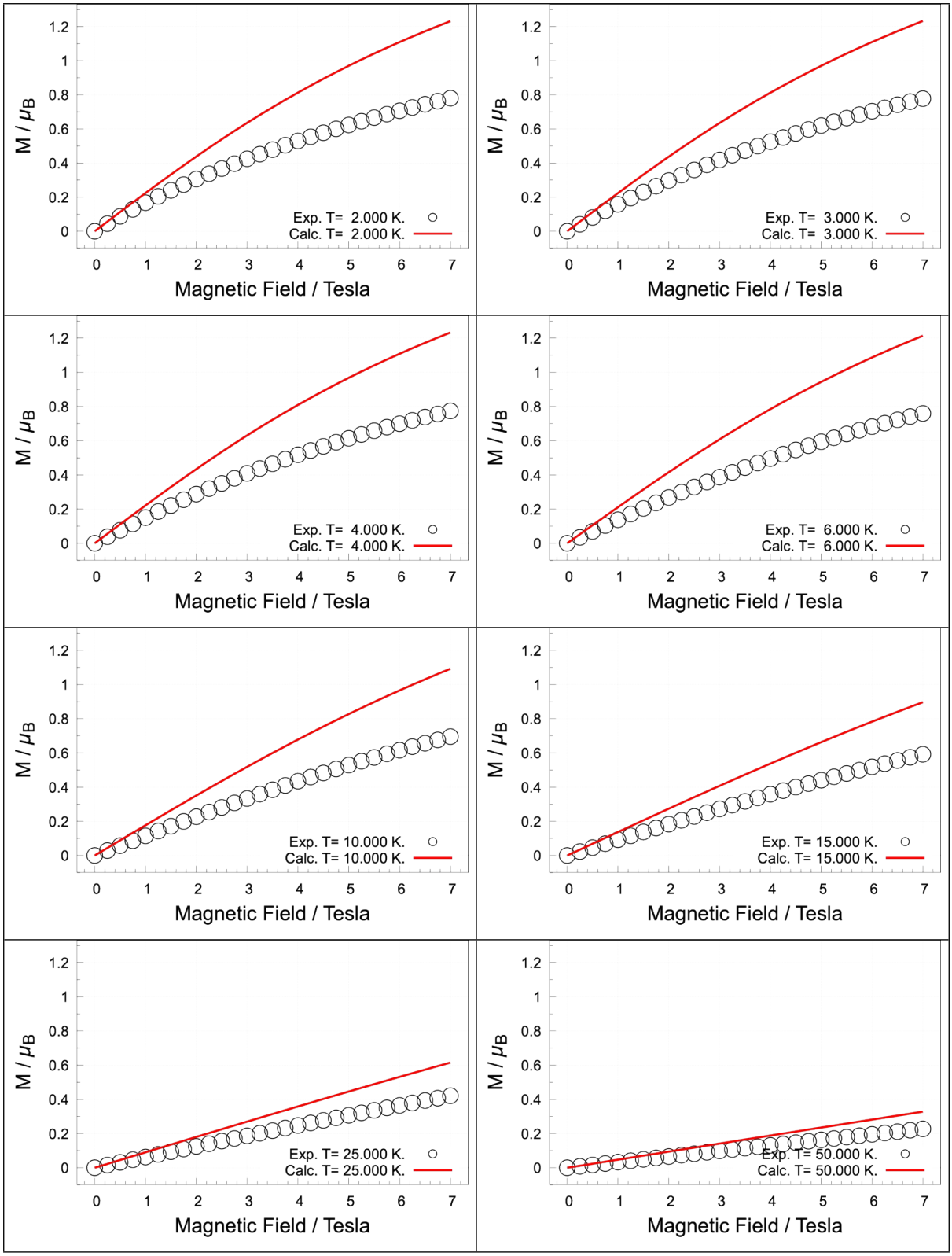

Figure S22. Comparison between measured and calculated molar magnetization for **3a**, using the CASPT2, CAS(14in12) results.

Computational Estimation of the ground state spin on Co alone

The previous section revealed that the ground state of **3a** is *S*=1, indicating that this state results from the antiferromagnetic coupling between a high-spin Co (*S*=3/2) and a radical (*S*=1/2). To this end, we employed two ways of killing the radical, such that we find the ground spin state on Co alone. The elimination of the radical is done in two approaches:

First approach: Compute the cationic form of **3a**, by removing one electron. We label it $\mathbf{3}^{+}$.

Second approach: Add one H attached to the atom S4, such as the additional electron from the added H atom compensating the radical's electron. We label it $\mathbf{3}^{\mathbf{H}}$.

Table S11. Ground state total energies for different spin multiplicities (a.u.) for $\mathbf{3}^{+}$ (where the radical's electron is removed).

DFT	Spin	Absolute Energy (a.u.)	Relative Energy (a.u.)	Relative Energy (cm^{-1})
B3LYP	*S* = 1/2	-5030.380681089	0.0236533469	5191.3
	S = 3/2	-5030.404334436	0.0	0.0
PBE	*S* = 1/2	-5028.342085057	0.0073030678	1602.8
	S = 3/2	-5028.349388125	0.0	0.0
TPSS0	*S* = 1/2	-5031.886230006	0.0304448450	6681.9
	S = 3/2	-5031.916674851	0.0	0.0
wB97	*S* = 1/2	-5031.678409831	0.0267497880	5870.9
	S = 3/2	-5031.705159619	0.0	0.0

Table S12. Loewdin spin population analysis on the main atoms, with S =3/2, for the $\mathbf{3}^{+}$ (where the radical's electron is removed).

Atom	nr	B3LYP	PBE	TPSS0	wB97
Co	1	2.506321	2.316225	2.612582	2.529717
Cl	2	0.138706	0.251939	0.095822	0.140482
S	3	0.008662	0.069030	-0.028977	-0.090262
S	4	0.123787	0.035037	0.162152	0.272980
S	5	0.014395	0.099324	-0.019790	-0.060659
N	6	0.017911	-0.001540	0.022897	0.039507
N	7	0.019122	0.017567	0.022940	0.043023
N	8	0.014189	0.012447	0.011743	0.011487
C	18	-0.015766	-0.004433	-0.031344	-0.081474
C	19	0.028689	0.019054	0.029772	0.043894
C	20	0.025139	-0.004983	0.026055	0.032305
C	42	0.076184	0.119066	0.059487	0.079213
C	47	0.009452	0.017070	0.007685	0.008949

Table S13. Ground state total energies for different spin multiplicities (a.u.) for **3^{H}** (where the additional H atom kills the radical).

DFT	Spin	Absolute Energy (a.u.)	Relative Energy (a.u.)	Relative Energy (cm^{-1})
B3LYP	S = 1/2	-5031.158285760	0.0287645983	6313.1
	S = 3/2	-5031.187050358	0.0	0.0
PBE	S = 1/2	-5029.106512227	0.0188335249	4133.5
	S = 3/2	-5029.125345752	0.0	0.0
TPSS0	S = 1/2	-5032.676460992	0.0340152739	7465.5
	S = 3/2	-5032.710476266	0.0	0.0
wB97	S = 1/2	-5032.482268427	0.0313694906	6884.8
	S = 3/2	-5032.513637918	0.0	0.0

Table S14. Loewdin spin population analysis on main atoms, S =3/2 for **3^{H}** (where the additional H atom kills the radical)..

Atom	nr	B3LYP	PBE	TPSS0	wB97
Co	1	2.486311	2.248471	2.598596	2.528865
Cl	2	0.144459	0.199576	0.112114	0.135092
S	3	0.121679	0.183330	0.091486	0.109394
S	4	0.011297	0.020322	0.008316	0.007513
S	5	0.115849	0.167631	0.088557	0.106403
C	18	0.024131	0.036922	0.019013	0.018257
C	19	0.009369	0.020247	0.006775	0.006237
C	20	0.010297	0.022991	0.007214	0.007406
C	42	0.046790	0.057157	0.041442	0.055932

As we infer from Tables S10 and S12, the two methods of deactivating the radical's spin predict the ground spin state to be S=3/2, where spin is dominantly localized on the Co site. By comparing the spin delocalization in the ligand, Table S8 and Tables S10 and S12, we can conclude the radical's spin is distributed among atoms S3, S4, C18, C19. We also note the opposite signs of the spin population on the Co atom and ligand in **3a** (Table S8), a sign of antiferromagnetic coupling. In addition, the spin population on the Co atom is similar in Table S8, S10, and S12, which proves that the spin on Co(II) in compound **3a** is S=3/2.

Multireference calculations for 3^+ (where the radical's electron is removed).

We used OpenMOLCAS, CASSCF, and CASPT2 methods to compute the low-lying energy structure for **3**. To this end, ten states $S = 3/2$ and forty states $S = 1/2$ were optimized within the multiconfigurational self-consistent field method (CASSCF) and mixed further by spin-orbit interaction in restricted state interaction (RASSI). The XMS-CASPT2 method included dynamic electron correlation. The resulting spin-orbit eigenfunctions express the compound's spin and magnetic moments and compute its magnetic properties.

ANO-RCC basis sets described all atoms. Co, S, N, and closest C atoms to the Co were described by VTZP basis set contractions, while distant atoms acquired VDZ basis set contraction. RI/CD decomposition of the bielectronic integrals method allowed for a significant speedup in the calculation.

Three active spaces were used:

1) **CAS(7in5)** comprises seven electrons in five Co-3d orbitals ($3d^7$).
2) **CAS(7in10)** consists of CAS(7in5) + a full set of empty shell Co $4d^0$
3) **CAS(9in12)** consists of CAS(7in10) + one doubly occupied orbital (HOMO-1 and one empty orbital (LUMO-1)

Table S15. Low-lying energy structure on $\mathbf{3}^{+}$ in different computational models, in cm^{-1}., as predicted by CASSCF/RASSI

CAS-7in5		CAS-7in10		CAS-9in12	
CASSCF	CASPT2	CASSCF	CASPT2	CASSCF	CASPT2
0.0	0.0	0.0	0.0	0.0	0.0
0.0	0.0	0.0	0.0	0.0	0.0
54.9	53.9	52.7	54.6	49.0	48.7
54.9	53.9	52.7	54.6	49.0	48.7
2186.5	2407.1	2111.2	2587.6	2205.8	2762.4
2186.5	2407.1	2111.2	2587.6	2205.8	2762.4
2321.8	2483.2	2233.0	2672.7	2325.5	2842.5
2321.8	2483.2	2233.0	2672.7	2325.5	2842.5
3674.0	4718.4	3840.2	4922.7	3899.9	5044.2
3674.0	4718.4	3840.2	4922.7	3899.9	5044.2
3855.7	4824.9	3998.0	5001.0	4057.5	5117.6
3855.7	4824.9	3998.0	5001.0	4057.5	5117.6
4333.9	5651.5	4561.2	5603.6	4589.1	5683.9
4333.9	5651.5	4561.2	5603.6	4589.1	5683.9
4455.3	5736.7	4664.2	5709.8	4700.1	5780.9
4455.3	5736.7	4664.2	5709.8	4700.1	5780.9
5765.8	7277.5	6002.8	7376.2	6067.4	6138.7
5765.8	7277.5	6002.8	7376.2	6067.4	6138.7
5920.2	7336.3	6137.8	7439.1	6198.9	7506.4
5920.2	7336.3	6137.8	7439.1	6198.9	7506.4
6376.4	8213.6	6659.7	8338.2	6703.2	7576.7
6376.4	8213.6	6659.7	8338.2	6703.2	7576.7
6532.0	8271.8	6795.4	8368.5	6837.5	8410.4
6532.0	8271.8	6795.4	8368.5	6837.5	8410.4
9014.6	8421.4	9606.5	11194.9	9576.6	8454.2
9014.6	8421.4	9606.5	11194.9	9576.6	8454.2
9054.6	11296.5	9637.7	11829.0	9608.9	10851.0
9054.6	11296.5	9637.7	11829.0	9608.9	10851.0

Table S16. Main values of the *g* tensor for the ground state within the formalism of pseudospin $S = 3/2$ for the $\mathbf{3}^{+}$. Zero-field splitting parameters are also listed.

	CAS-7in5		CAS-7in10		CAS-9in12	
	CASSCF	CASPT2	CASSCF	CASPT2	CASSCF	CASPT2
	Main values of the *g* tensor for the ground $S = 3/2$					
g_x	2.1744	2.3009	2.1564	2.1128	2.1575	2.1163
g_y	2.3405	2.2162	2.3032	2.1590	2.3083	2.1584
g_z	2.5353	2.0520	2.5116	2.4016	2.4904	2.3737

g_{iso}	2.3547	2.1922	2.3283	2.2281	2.3227	2.2190
	Zero-Field Splitting parameters, *D*, *E* for the ground *S* = 3/2					
D	-24.4693	26.6413	-23.8060	-26.2705	-21.6373	-23.2669
E	-7.1660	-2.4287	-6.5269	-4.3206	-6.6151	-4.1572

$$g_{iso} = \sqrt{\frac{g_x^2 + g_y^2 + g_z^2}{3}}$$

The axial zero-field splitting (ZFS) parameter D and the rhombicity parameter E/D were calculated using the ab initio state-averaged CASSCF method combined with the effective Hamiltonian approach. The computed values are:

D = −24.4693 cm $^{-1}$

E/D = 0.2928

The calculations were performed using the def2-TZVP basis set for Co, Cl, and S, while the def2-SVP basis set was used for the lighter elements C and H.

Table S17. Main values of the *g* tensor for the ground state within the formalism of pseudospin *S* = 1/2 for the **3**$^{+}$, for the ground and first excited Kramers doublets.

	CAS-7in5		CAS-7in10		CAS-9in12	
	CASSCF	CASPT2	CASSCF	CASPT2	CASSCF	CASPT2
	Main values of the *g* tensor for the ground Kramers Doublet pseudospin S = 1/2					
g_x	1.4587	5.1818	1.3846	0.9213	1.4897	0.9889
g_y	2.0643	3.8044	1.9162	1.1083	2.1226	1.2030
g_z	7.0544	2.0020	7.0445	7.0059	6.8880	6.8956
	Main values of the *g* tensor for the first excited Kramers Doublet pseudospin S = 1/2					
g_x	1.9941	0.5838	2.0377	2.2229	1.9210	2.1639
g_y	2.6139	0.6348	2.6843	3.2109	2.4891	3.1156
g_z	5.8188	6.1077	5.7083	5.1563	5.8140	5.2294

Broken-Symmetry evaluation of the magnetic exchange interactions in CoR

Table S18. Broken-symmetry calculations of magnetic exchange between Co^{II} $S = 3/2$ and one radical (S=1/2) ($H_{exch} = -2J\ S_A S_B$ convention).

DFT	*J*(1)	*J*(2)	*J*(3)
B3LYP	-423.82	-282.55	-533.62
PBE	-639.64	-426.43	-730.34
TPSS0	-333.00	-222.00	-427.93
wB97	-317.39	-211.59	-409.73

J(1) (from -(E[HS]-E[BS])/Smax**2)

J(2) (from -(E[HS]-E[BS])/(Smax*(Smax+1))

J(3) (from -(E[HS]-E[BS])/(<S**2>HS-<S**2>BS))

Lines model description of the magnetic properties for Co^{II}-Radical (POLY-ANISO)

$\hat{H}_{exch} = -2J\hat{S}_{Co}\hat{S}_{Rad}$

Where $\hat{S}_{Co} = 3/2$, while $\hat{S}_{Rad} = 1/2$. The Co site was described using the *ab initio* calculation for the **3**$^{+}$ case, CAS(9in12), CASPT2, data given in Table S17.

We use the magnetic exchange obtained in BS-DFT with B3LYP, Table S13, $J = -533.62$ cm^{-1}.

Results:

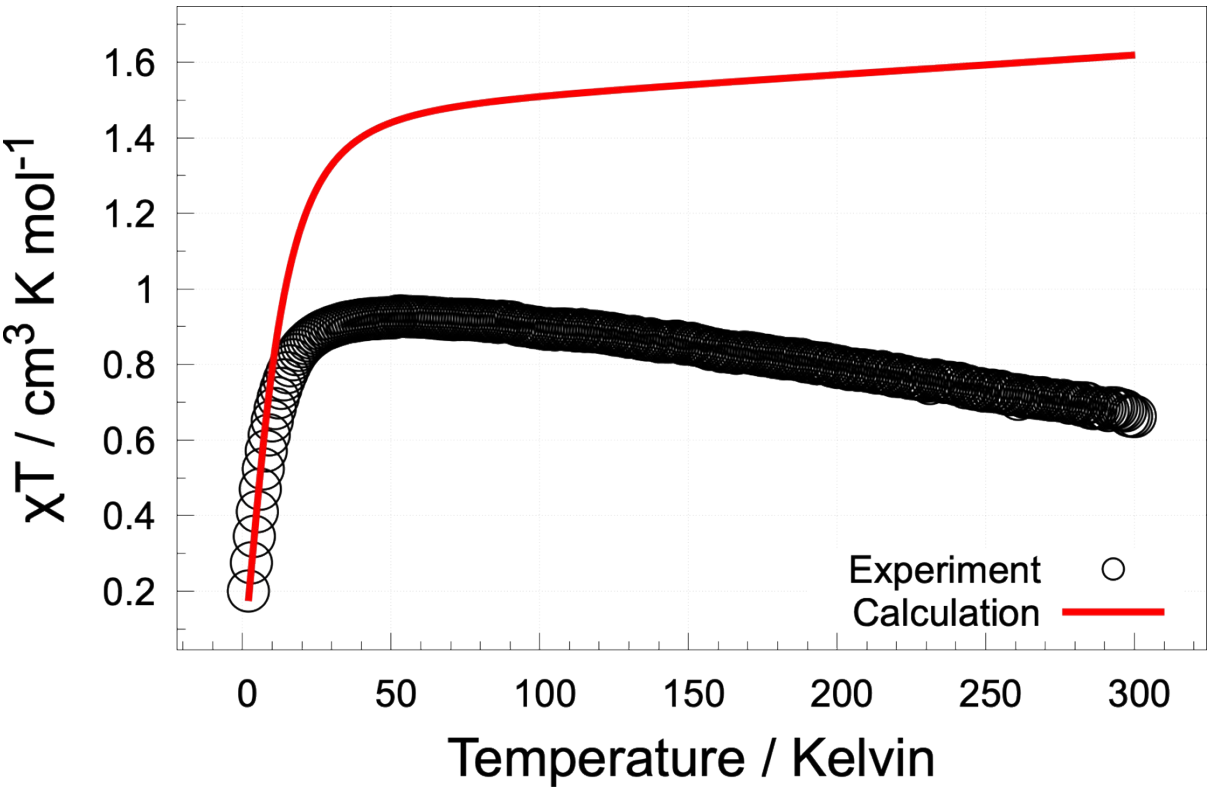

Figure S23. Comparison between measured and ab initio calculated magnetic susceptibility (XT) for **3**, using the CASPT2, CAS(9in12) results, and J=-533.62 cm^{-1}.

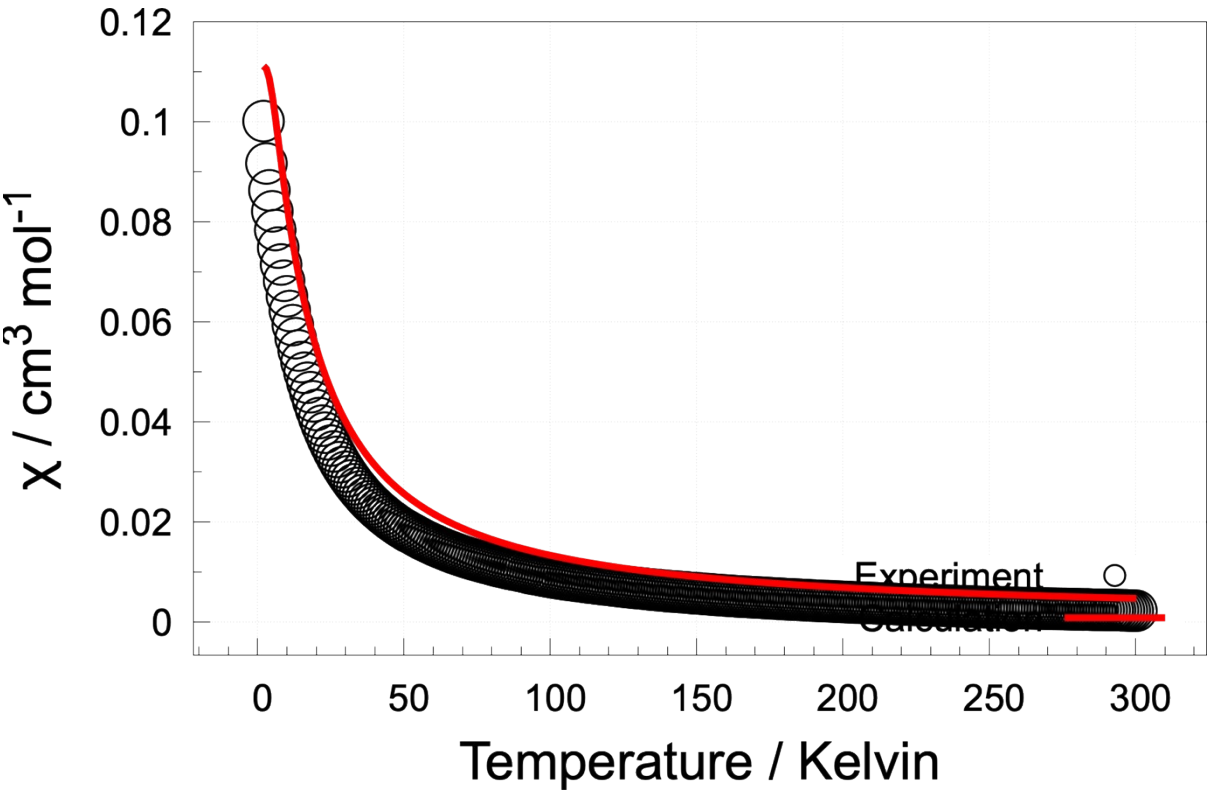

Figure S24. Comparison between measured and ab initio calculated magnetic susceptibility (X) for **3**, using the CASPT2, CAS(9in12) results, and J=-533.62 cm^{-1}.

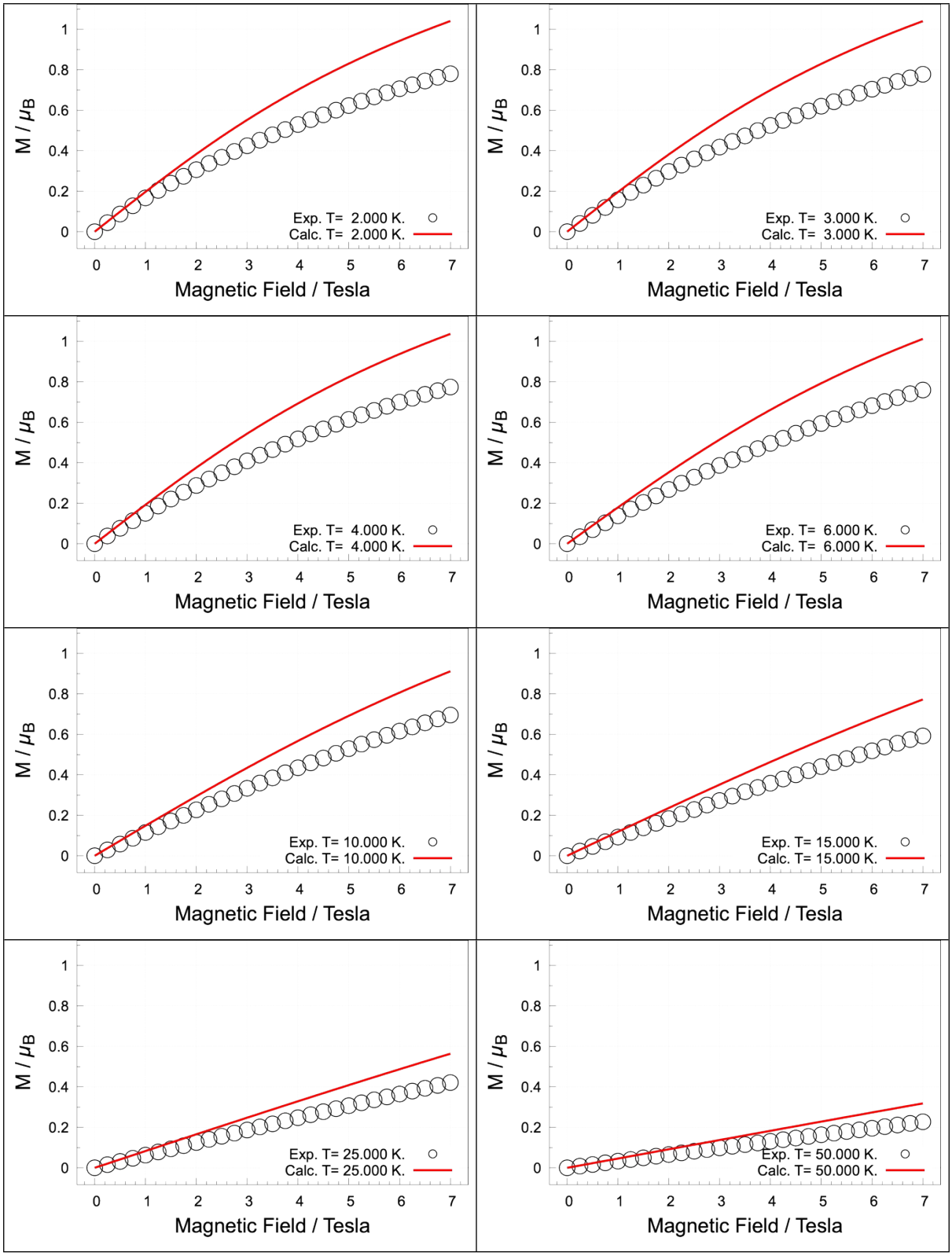

Figure S25. Comparison between measured and calculated molar magnetization for **3a**, using the CASPT2, CAS(9in12) results, and J = -533.62 cm^{-1}.

……

12. Photo-Catalysis: Catalytic organic transformation

4a ; **4b** **5a,** 38% ; **5b,** 46%

N-isopentylcrinasiadi

A 16×100 mm oven-dried reaction tube equipped with a magnetic stir was charged with **Cat. 3a** (5.0 mol%) and iodo-substituted benzamide **4** (0.2 mmol, 1.0 equiv) under a nitrogen atmosphere. The reaction tube was capped with a septum, and dry CH_3CN (2 mL) and nBu$_3$N (5.0 equiv) were added via a syringe. After that, the reaction mixture was allowed to stir with irradiation of 427 nm blue LEDs under N_2 atmosphere at room temperature for 24 h. Then, volatiles were removed under reduced pressure, and the crude reaction mixture was loaded onto a silica gel column for purification, yielding pure phenanthridinone **5**. Upon irradiation of **Cat. 3a** with 427 nm Kessil light in the absence of any reactants, gradual decomposition was observed over 20 hours, indicating limited photostability under prolonged light exposure. In contrast, **Cat. 3a** remained stable for at least 24 hours when kept in the dark. Furthermore, when the reaction was carried out under 427 nm irradiation in the absence of **Cat. 3a**, the starting material was fully recovered, and no product formation was observed. Similarly, when **Cat. 3a** was present, but the reaction was performed in the dark, and no product was formed. These results demonstrate that both the presence of **Cat. 3a** and light irradiation are essential for catalytic activity.

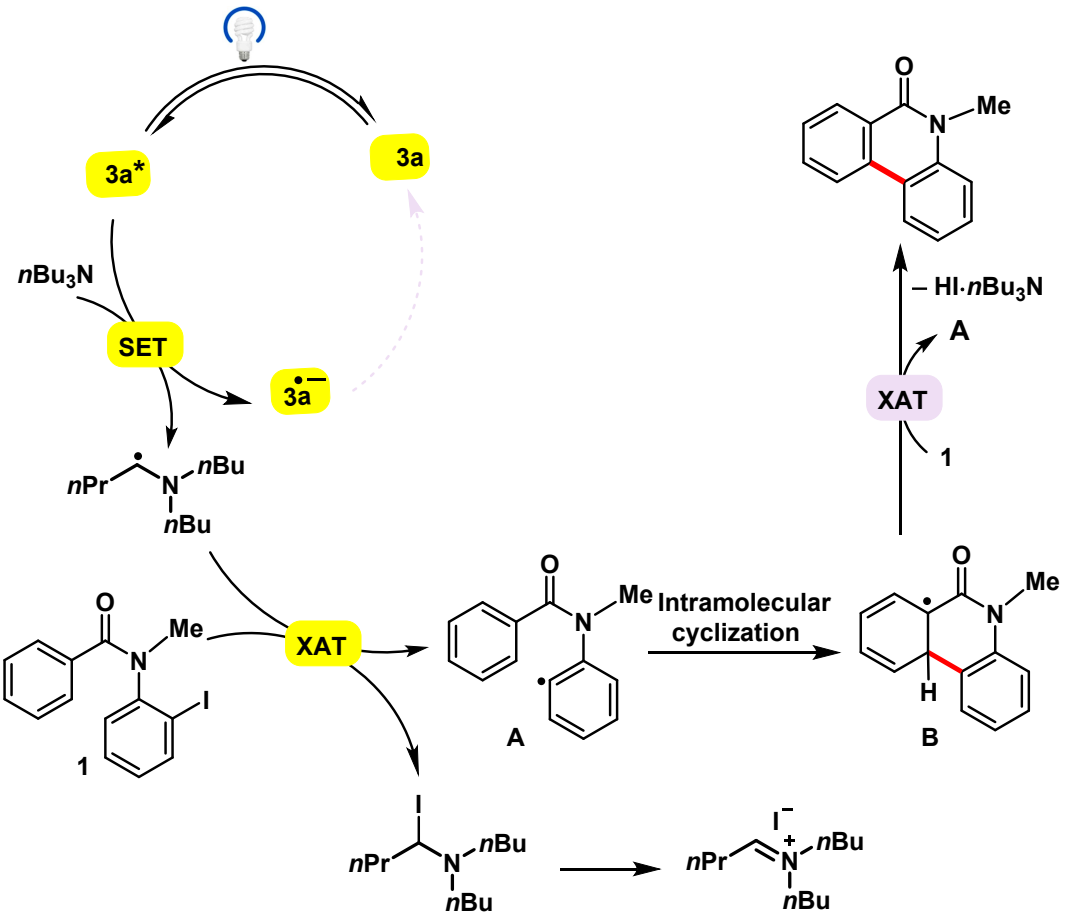

Scheme S1. Plausible reaction mechanism for the photo-catalytic reaction of **3a**.

^{1}H and ^{13}C NMR spectral data of synthesized compounds (**5a-5b**):

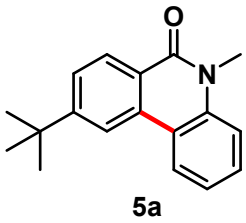 **5a**	Compound, **5a**: White solid, eluent (5% ethyl acetate in hexane). **Yield:** 38% (19 mg); **^{1}H NMR (400 MHz, $CDCl_3$)** δ 8.57 (d, J = 2.3 Hz, 1H), 8.26 – 8.19 (m, 2H), 7.82 – 7.80 (m, 1H), 7.53 – 7.49 (m, 1H), 7.40 (d, J = 8.4 Hz, 1H), 7.30 (t, J = 7.6 Hz, 1H), 3.81 (s, 3H), 1.43 (s, 9H). **^{13}C NMR (101 MHz, $CDCl_3$)** δ 161.8, 145.4, 136.0, 134.0, 132.4, 129.1, 127.9, 127.3, 125.8, 121.6, 119.6, 118.9, 115.0, 34.7, 31.6, 30.1.
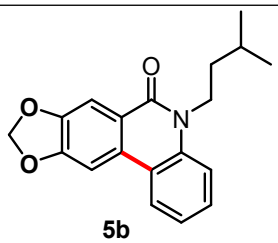 **5b**	Compound **5b**: White solid, eluent (5% ethyl acetate in hexane). **Yield:** 46% (28 mg); **^{1}H NMR (500 MHz, $CDCl_3$)** δ 8.11 – 8.09 (m, 1H), 7.91 (s, 1H), 7.61 (s, 1H), 7.52 – 7.49 (m, 1H), 7.39 – 7.37 (m, 1H), 7.29 – 7.28 (m, 1H), 6.11 (s, 2H), 4.40 – 4.37 (m, 2H), 1.86 – 1.79 (m, 1H), 1.70 – 1.65 (m, 2H), 1.06 (d, J = 6.6 Hz, 6H). **^{13}C NMR (101 MHz, $CDCl_3$)** δ 160.7, 152.3, 148.5, 136.7, 130.6, 129.0, 123.3, 122.2, 121.5, 119.6, 115.1, 107.0, 102.1, 100.5, 41.6, 36.2, 26.8, 22.7.

^{1}H and ^{13}C NMR Spectra of Synthesized Compounds

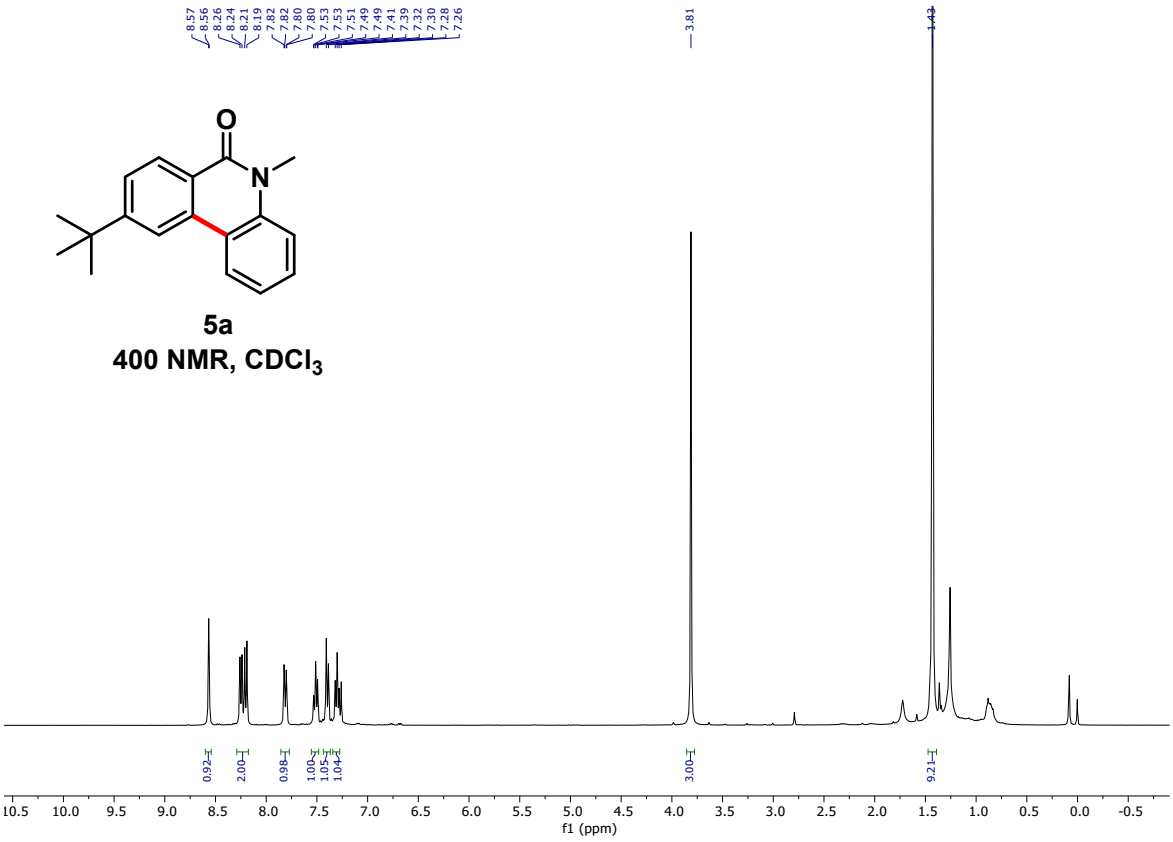

Figure S26. ^{1}H NMR spectrum of **5a**.

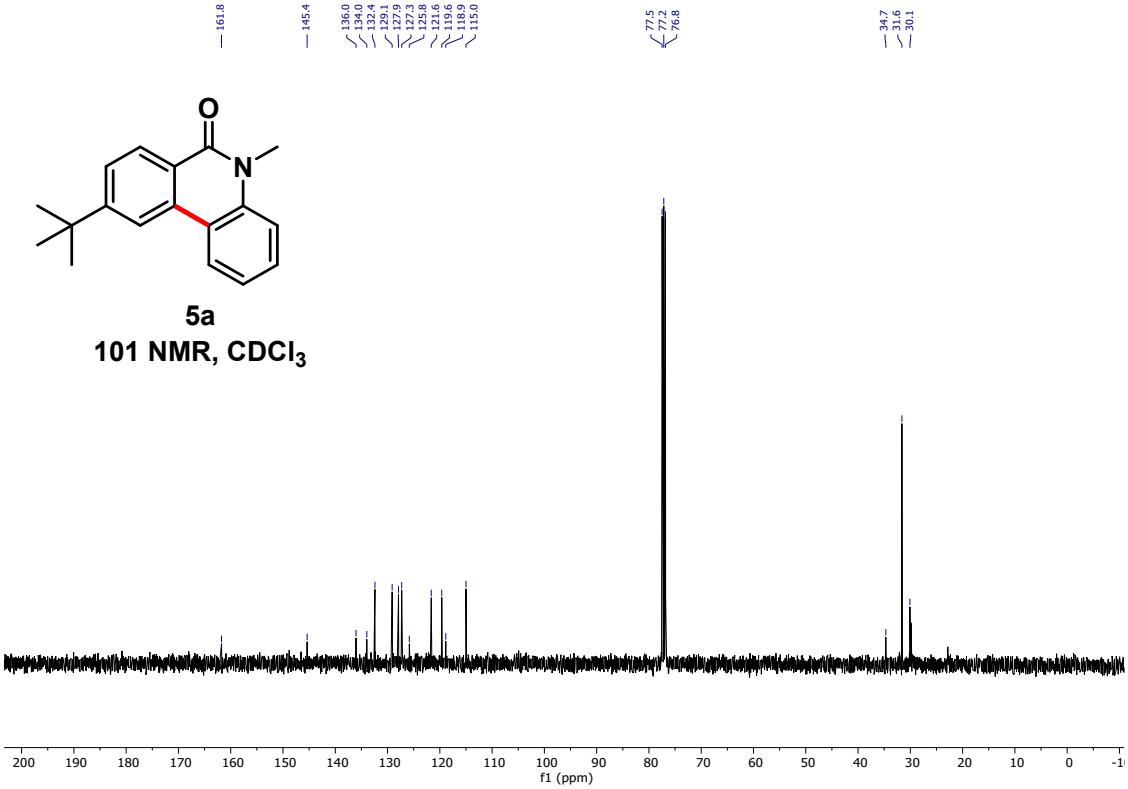

Figure S27. ^{13}C NMR spectrum of **5a**.

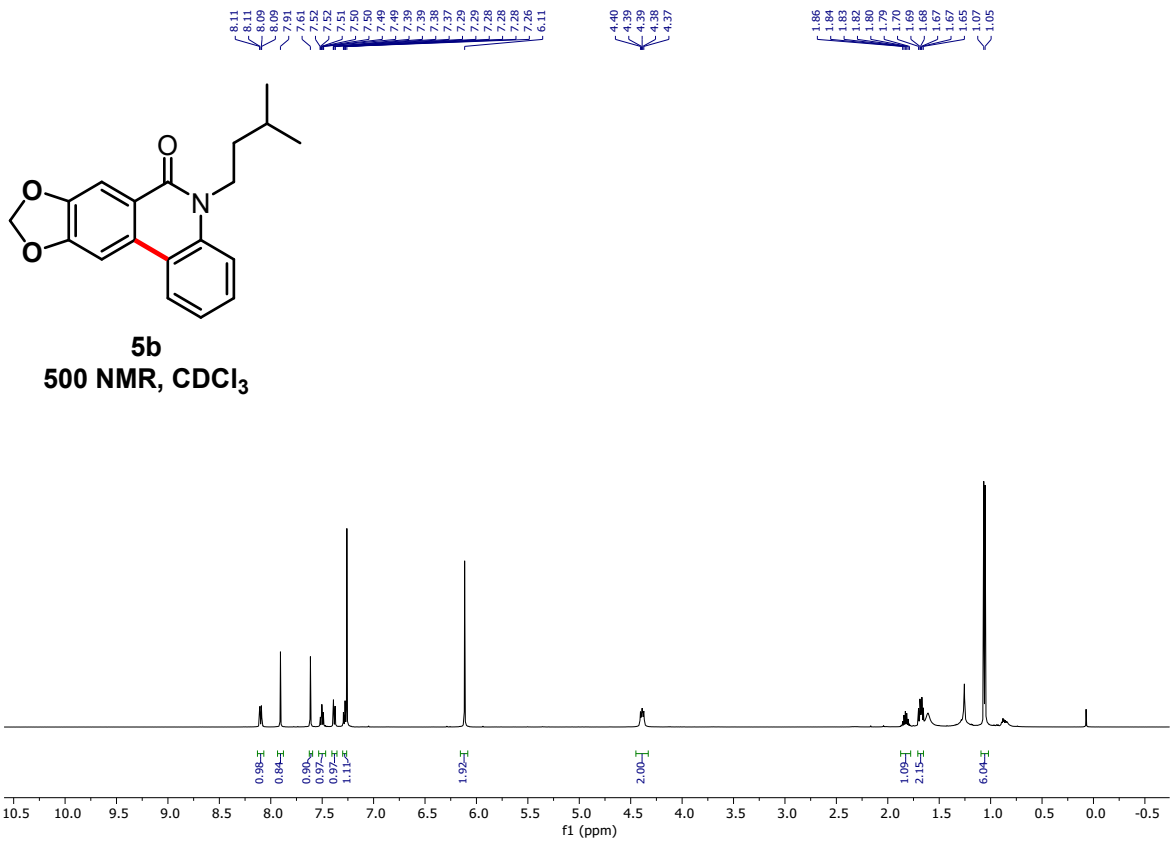

Figure S28. ^{1}H NMR spectrum of **5b**.

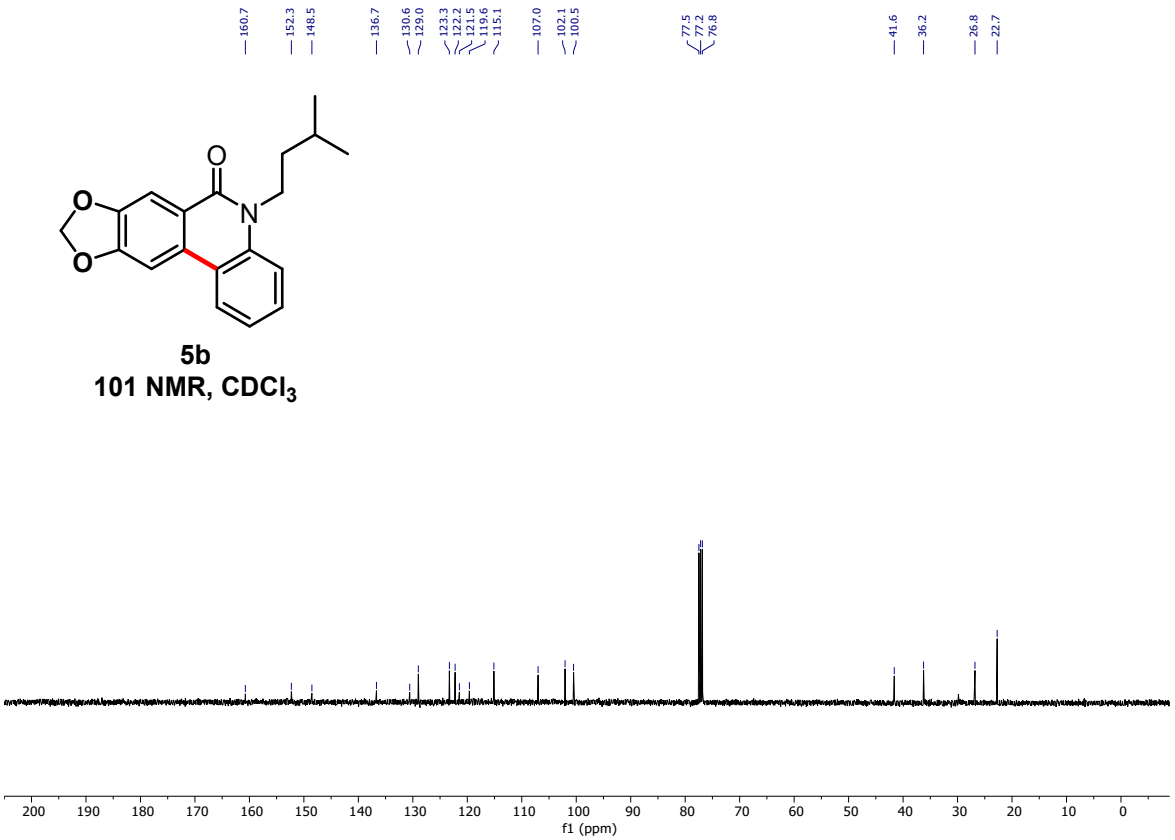

Figure S29. ^{13}C NMR spectrum of **5b**.

13. Experimental procedures for polymerization reaction

1. Methods

All the NMR experiments were performed in Bruker Avance-500 instrument with the chemical shift (δ) referenced to residual solvent (δ^H, δ^C = 0 for $Si(CH_3)_4$. All spectra were processed using Topspin software. The GPC analysis of the polymers was carried out on a WATERS LC-20AD instrument equipped with a refractive index (RI) detector at 40 °C and with a flow rate of 0.8 mL/min. The samples were dissolved in HPLC-grade THF and were filtered through 0.2 μm PTFE filters prior to the analysis. The instrument was calibrated using narrow-M_n polystyrene standards. The DSC measurements were performed on **NETZSCH DSC 204 F1 PHOENIX at a heating rate of 10 °C/min.** Thermogravimetric analysis (TGA) was done with a TA Instruments Q500. 5 mg of each sample was loaded onto a platinum pan and subjected to a dynamic high-resolution scan with a heating rate of 20 °C min^{-1} in a nitrogen atmosphere. Each sample was heated up to 900 °C from room temperature.

2. Materials

All the moisture and air-sensitive reactions were performed under an inert atmosphere of argon using an MBraun glovebox. The reagents were obtained from Sigma Aldrich and used as

received, unless stated otherwise. Toluene was dried over Na/benzophenone and freshly distilled before each use. The monomer *rac*-LA was recrystallized from dry toluene, sublimed under vacuum before use, and stored inside the glove box. Cyclohexene oxide (CHO) was dried over calcium hydride (CaH_2) and freshly distilled before use. Phthalic anhydride (PA) was crystallized twice from hot chloroform ($CHCl_3$) and sublimed under vacuum before use. NMR solvent $CDCl_3$ (Cambridge Isotope Laboratories, Inc.) was dried over CaH_2 and distilled before use. The purification of tetra-*n*-butylammonium bromide (TBAB) was carried out by crystallizing it from toluene and drying it in a vacuum before use. The purification of Tetraphenylphosphonium chloride (TPPCl), bis(triphenylphosphine)iminium chloride (PPNCl) was carried out by crystallizing it from chloroform and hexane, and dried in a vacuum. Argon gas was purchased from Indogas, Bangalore, India.

3. Synthesis

3.1. General polymerization procedure for ROP of *rac*-LA

The reaction for the ROP of *rac*-LA was performed in a glass reaction tube equipped with a magnetic stirring bar. The constituents of the reaction were weighed inside the glove box and mixed such that *rac*-LA:Cat. = 200:1 followed by the addition of 1mL of dry toluene. The reaction tube was sealed properly by applying grease and taken out of the glove box. The tube was dipped in an oil bath maintained at 100 ˚C. The progress of the reaction was monitored by the analysis of the ^{1}H NMR spectra of the aliquots taken at different time interval. After the desired time interval, the solvent was evaporated under vacuum. Upon removal of the solvent, the crude product was dissolved in dichloromethane and precipitated by the addition of cold methanol. The polymer was filtered and dried under vacuum until the pure product gave constant weight.

3.2. General polymerization procedure for ROCOP of epoxide and anhydride

The reaction for the ROCOP of epoxide and anhydride was performed in a glass reaction tube equipped with a magnetic stirring bar. The constituents of the reaction were weighed inside the glove box and mixed such that CHO:PA:Cat:Cocat. = 400:100:1:1 followed by the addition of 1mL of dry toluene. The reaction tube was sealed properly by applying grease and taken out of the glove box. The tube was dipped in an oil bath maintained at 100 ˚C. The progress of the reaction was monitored by the analysis of the ^{1}H NMR spectra of the aliquots taken at different time intervals. After the desired time interval, the solvent was evaporated under vacuum. Upon removal of the solvent, the crude product was dissolved in dichloromethane and precipitated

by the addition of cold methanol. The polymer was filtered and dried under vacuum until the pure product gave a constant weight.

Table S19. ROCOP of CHO with PA using **3a** as a catalyst (Top) and results of polymerization reaction employing **2, [**$(cAAC)_2Co_2Cl_4$] and $Co^{II}Cl_2$ instead of complex **3a** (bottom).

Entry	Time (h)	Solvent	Temperature (^oC)	Cocat.	PA Conv. (%)[a]	Ester (%)[b]	M_n (g/mol)[c]	[$Đ$][d]	TOF (h^{-1})[e]
1	0.5	Neat	100	-	83	48	4070	1.56	166
2	1.5	Neat	100	PPNCl	78	34	5085	1.25	52
3	2	Neat	100	TBAB	16	52	-	-	-
4	1	Neat	100	TPPCl	>99	82	7205	1.23	100
5	1	Toluene	100	TPPCl	99	77	7550	1.10	99
6	3	Neat	80	TPPCl	79	72	2563	1.36	26
7[f]	2	Toluene	100	TPPCl	>99	77	2930	1.26	50

Entry	Catalyst	Cocat.	Solvent	Temperature (^{o}C)	Time (h)	PA Conv. (%)	Ester (%)	M_n (g/mol)	PDI
8	$CoCl_2$	-	Neat	100	4	11	-	-	-
9	$(cAAC)_2Co_2Cl_4$	TPPCl	Neat	100	4.5	99	49	-	-

Reaction conditions: [CHO]/[PA]/[Cat]/[Cocat] = 400:100:1:1. [a] Determined by ^{1}H NMR spectroscopy by integrating the normalized resonances of PA (7.97 ppm) and the phenylene signals of polymer (7.30-7.83 ppm). [b] Determined by ^{1}H NMR spectroscopy by integrating the normalized resonances of ester linkages (4.80-5.26 ppm) and the ether linkages (3.22-3.64 ppm). [c] M_n (GPC) measured by GPC at 40 ^{o}C in THF relative to polystyrene standards. [d] Determined by GPC, in THF with calibration using narrow-M_n polystyrene standards. [e] Turnover frequency (TOF) = TON/time(h). TON = Conversion X number of equivalents of monomer. [S17]. [f] The reaction was carried out with only TPPCl.

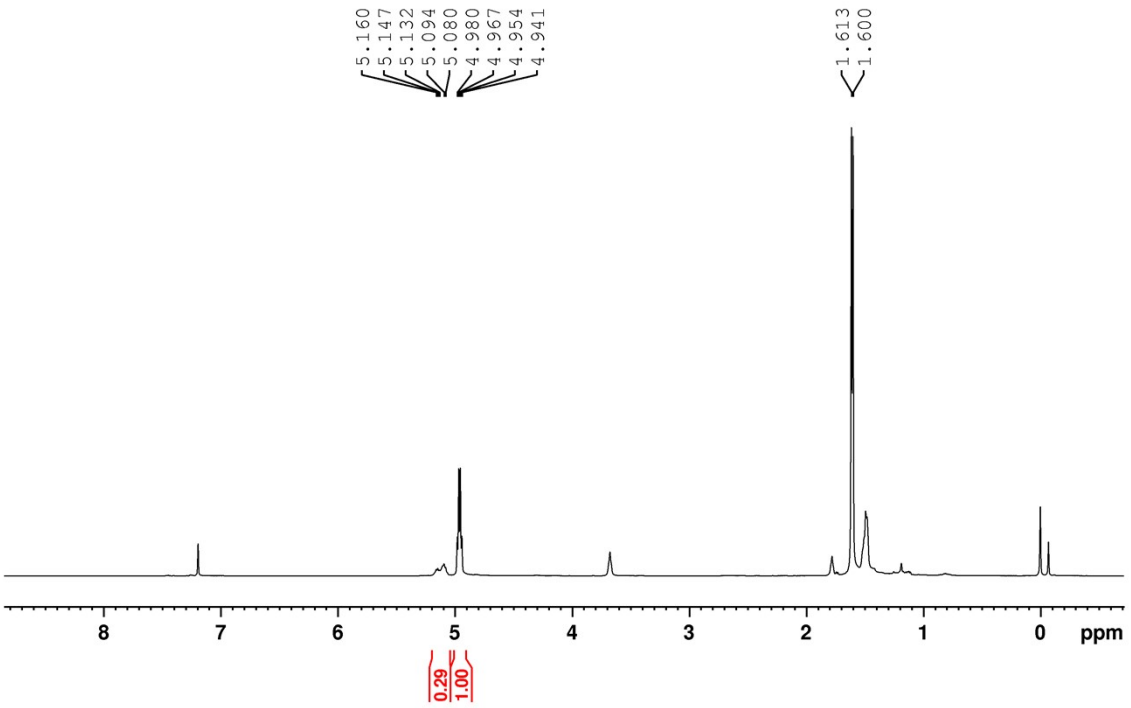

Figure S30. ^{1}H NMR ($CDCl_3$) spectrum of the crude PLA using **3a** as a catalyst

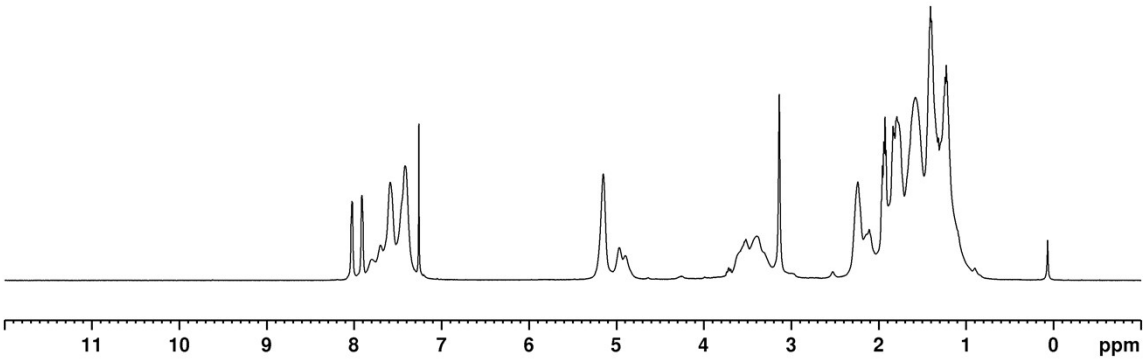

Figure S31. ^{1}H NMR ($CDCl_3$) spectrum of the crude polyesters of CHO/PA with **3a** in neat condition (Table 1, Entry 1)

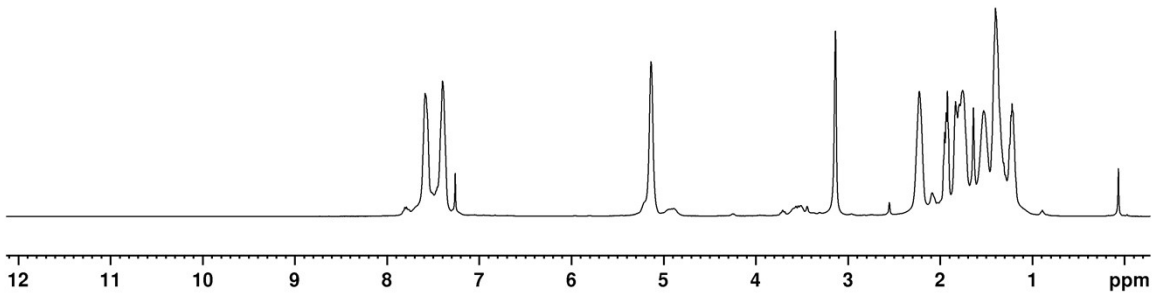

Figure S32. ^{1}H NMR ($CDCl_3$) spectrum of the crude polyesters of CHO/PA with **3a**/TPPCl in neat condition (Table S19, Entry 4)

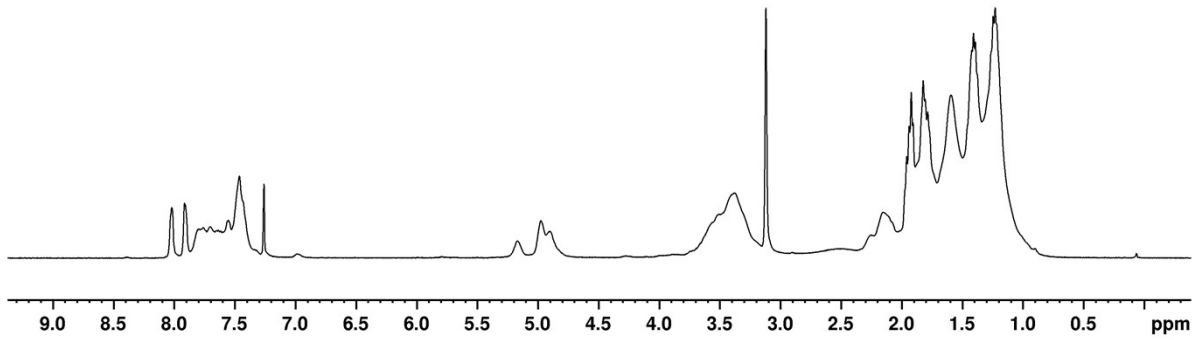

Figure S33. ^{1}H NMR ($CDCl_3$) spectrum of the crude polyesters of CHO/PA with **3a**/PPNCl in neat condition (Table S19, Entry 2)

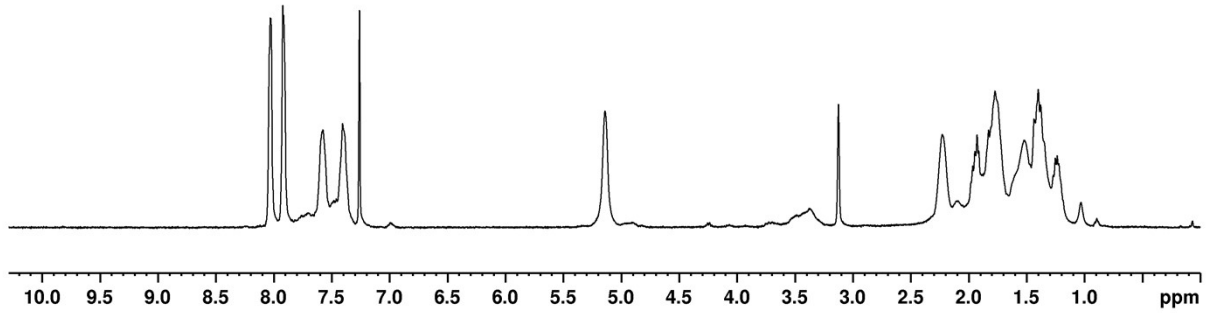

Figure S34. ^{1}H NMR ($CDCl_3$) spectrum of the crude polyesters of CHO/PA with **3a**/TBAB in neat condition (Table S19, Entry 3)

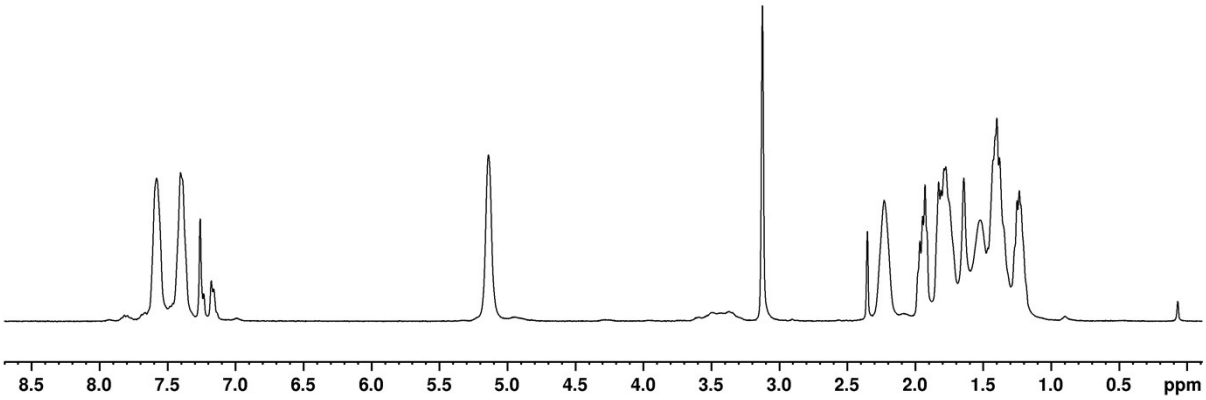

Figure S35. ^{1}H NMR ($CDCl_3$) spectrum of the crude polyesters of CHO/PA with **3a**/TPPCl in toluene (Table S19, Entry 5)

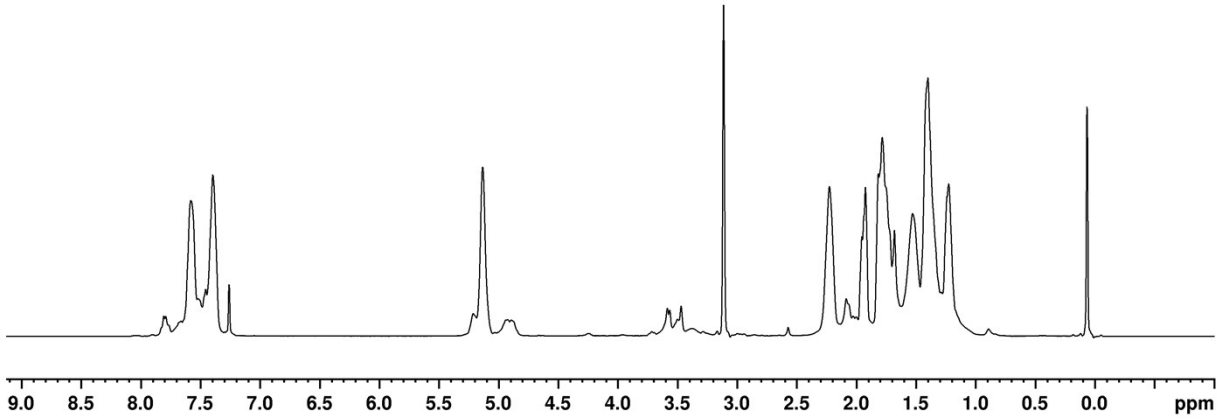

Figure S36. ^{1}H NMR ($CDCl_3$) spectrum of the crude polyesters of CHO/PA with **3a**/TPPCl at 80 °C neat condition (Table S19, Entry 6)

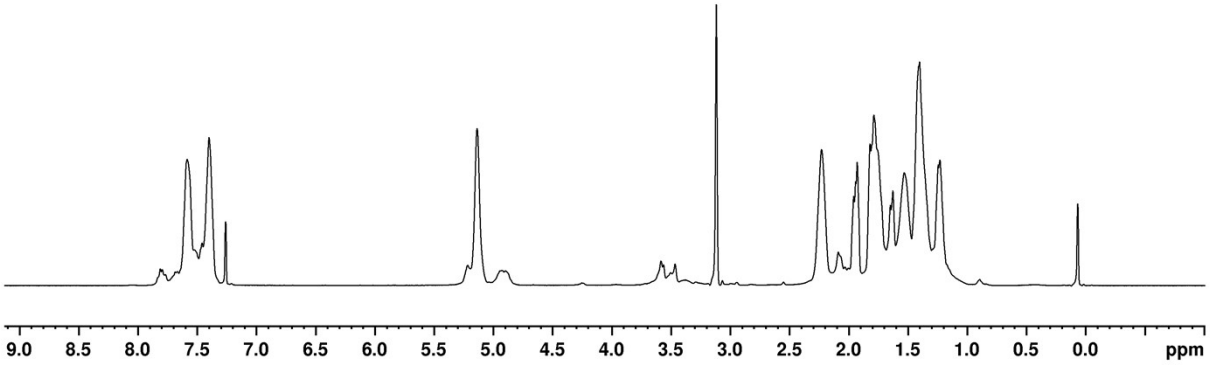

Figure S37. ^{1}H NMR ($CDCl_3$) spectrum of the crude polyesters of CHO/PA with TPPCl at 100 °C in toluene (Table S19, Entry 7)

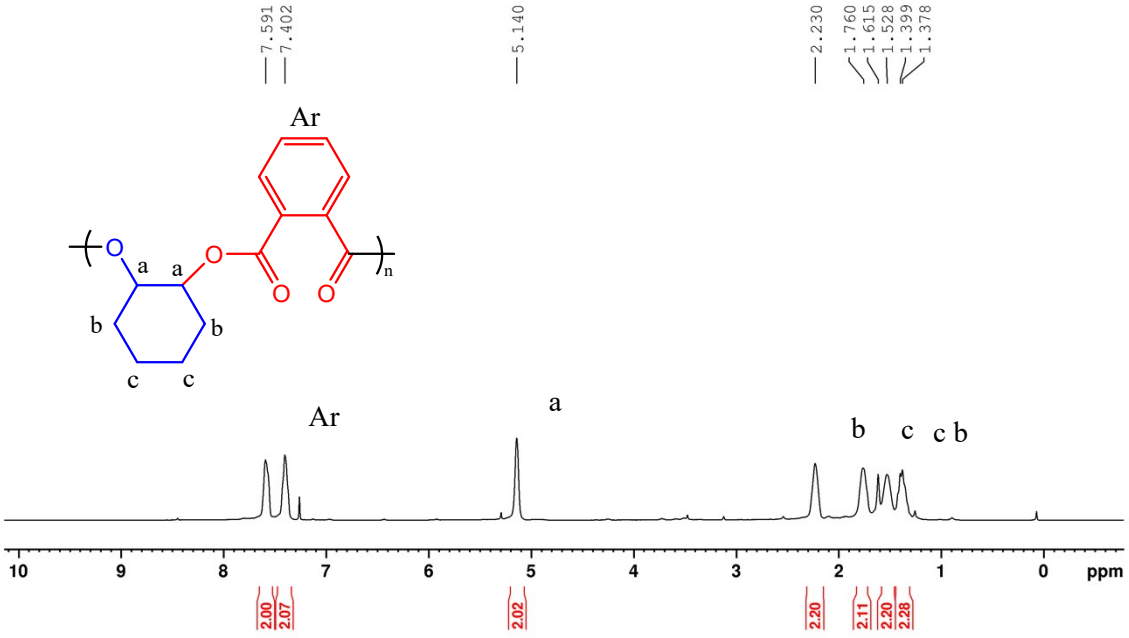

Figure S38. ^{1}H NMR ($CDCl_3$) spectrum of the pure polyesters of CHO/PA with **3a**/TPPCl in neat condition (Table S19, Entry 4)

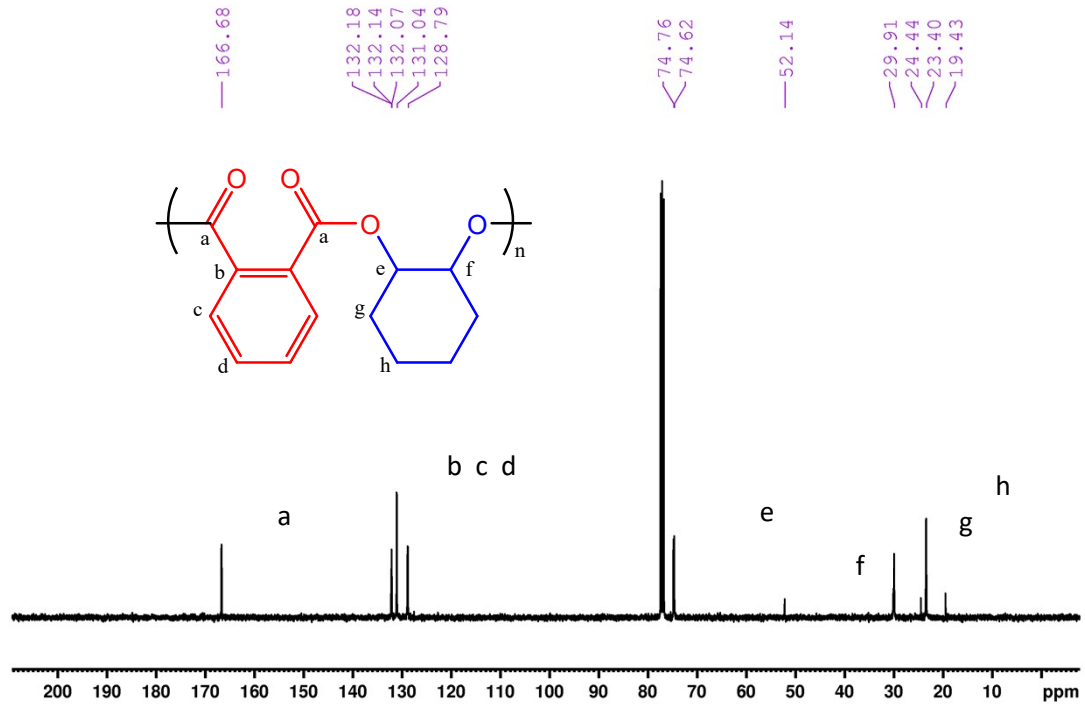

Figure S39. ^{13}C NMR ($CDCl_3$) spectrum of the pure polyesters of CHO/PA with **3a**/TPPCl in neat condition (Table S19, Entry 4)

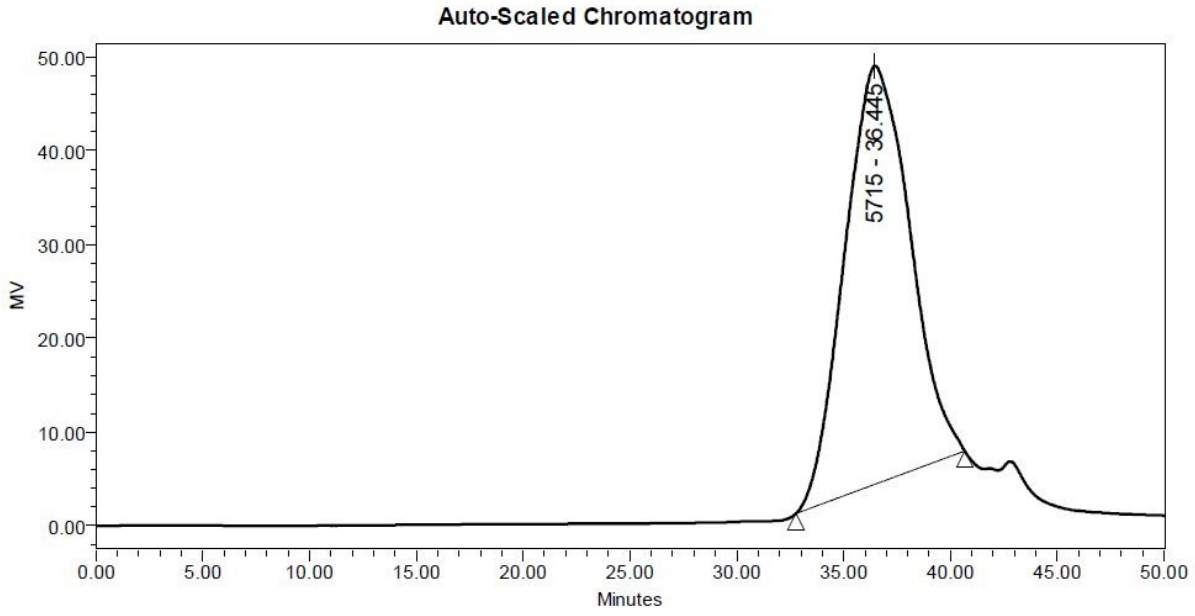

GPC Results

	Dist Name	Mn	Mw	MP	Mz	Mz+1	Mv	Polydispersity	MW Marker 1	MW Marker 2
1		4070	6359	5715	9164	12075		1.562521		

Figure S40. GPC trace of polyester (CHO/PA) using **3a** in neat condition (Table S19, Entry 1)

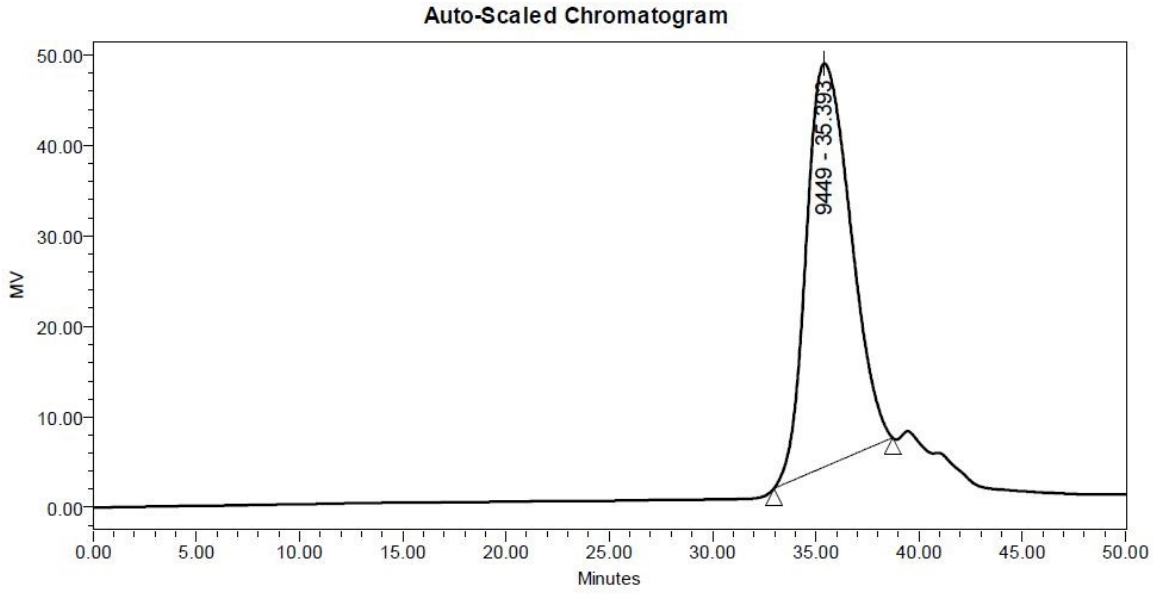

GPC Results

	Dist Name	Mn	Mw	MP	Mz	Mz+1	Mv	Polydispersity	MW Marker 1	MW Marker 2
1		7205	8891	9449	10621	12305		1.234092		

Figure S41. GPC trace of polyester (CHO/PA) using **3a** and TPPCl in neat condition (Table S19, Entry 4)

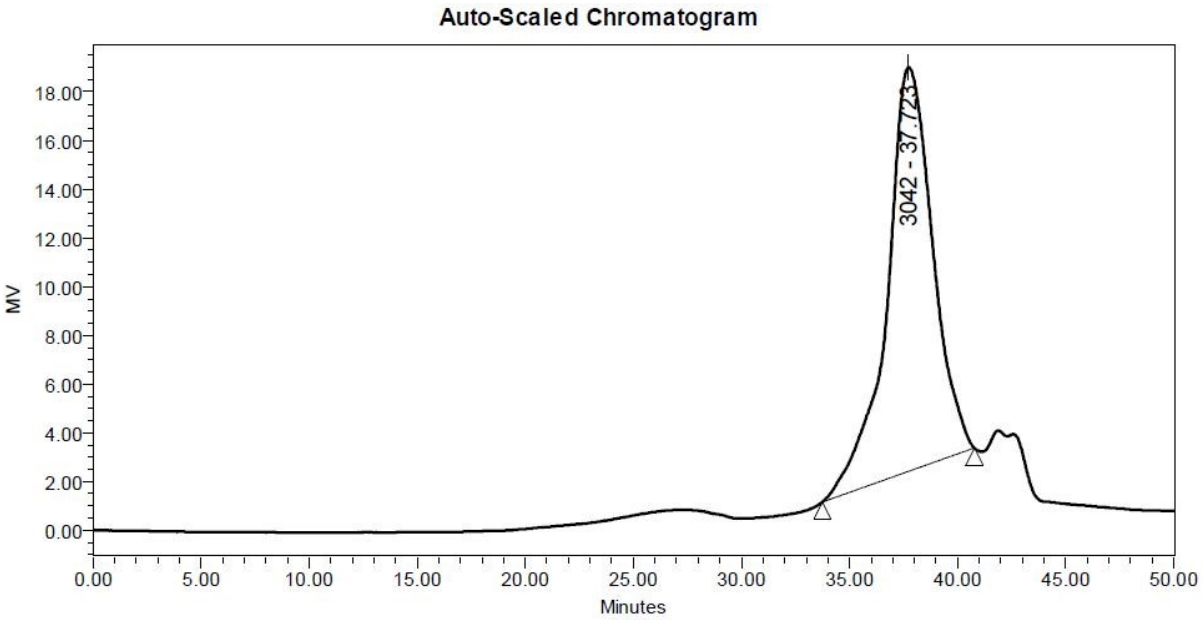

GPC Results

	Dist Name	Mn	Mw	MP	Mz	Mz+1	Mv	Polydispersity	MW Marker 1	MW Marker 2
1		2563	3496	3042	4993	7175		1.364143		

Figure S42. GPC trace of polyester (CHO/PA) using **3a** and TPPCl in 80 ^{o}C (Table S19, Entry 6)

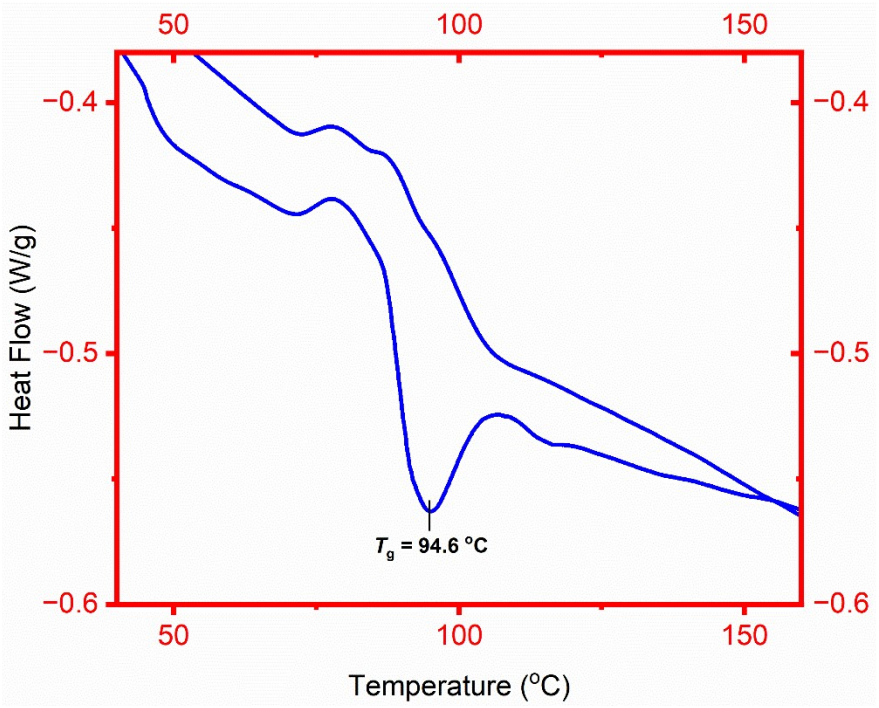

Figure S43. DSC trace of polyester (CHO/PA) using **3a** and TPPCl (Table S19, Entry 4)

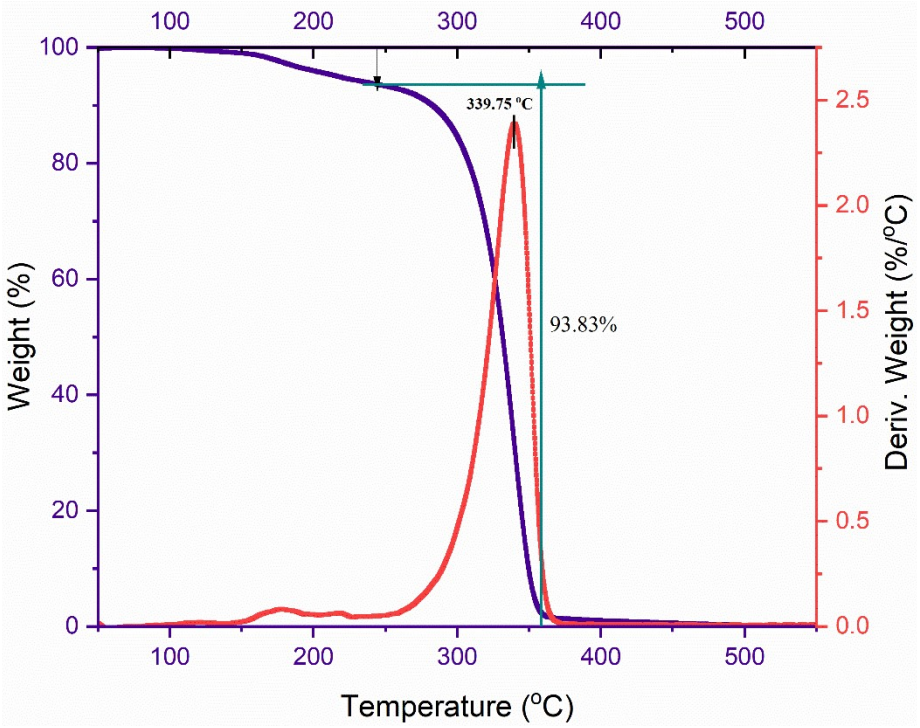

Figure S44. TGA trace of polyester (CHO/PA) using **3a** and TPPCl (Table S19, Entry 4).

Table S20. ROCOP of CHO with PA using **1** as a catalyst.

Entry	Catalyst	Cocat.	Solvent	Temperature (° C)	Time (h)	PA Conv. (%)	Ester (%)	M_n (g/mol)	PDI
1	1	TPPCl	Neat	100	6	99	80	3282	1.44

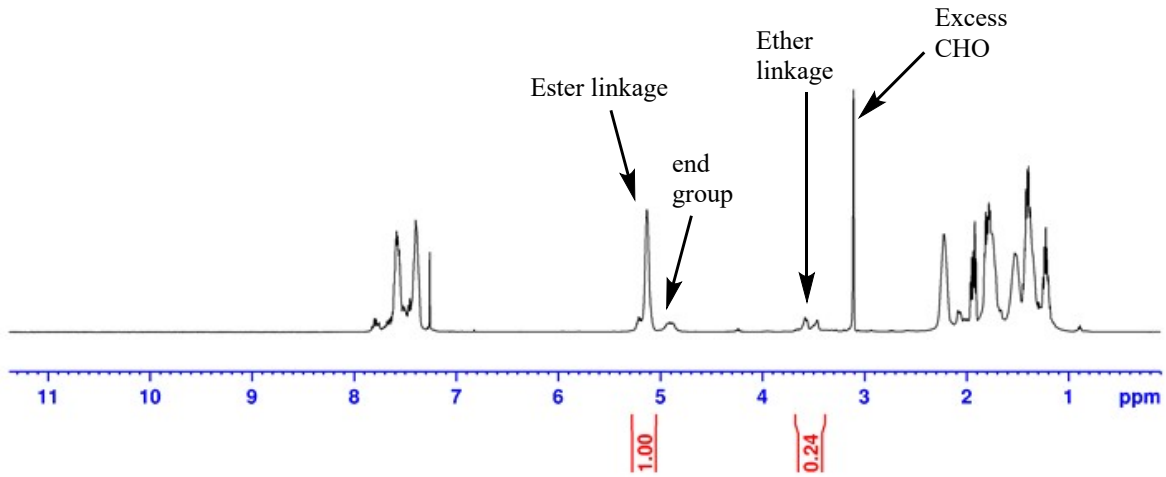

Figure S45. ^{1}H NMR spectrum ($CDCl_3$, 500 MHz) of crude polymer obtained by **1** and TPPCl.

We have explored the ROCOP of CHO with PA exploiting **1** as a catalyst in the presence of TPPCl cocatalyst, maintaining the same reaction conditions. It was found that the PA conversion and selectivity (% ester linkage) were almost the same, only the time taken for the PA conversion was higher with **1** (Table **S20**, Entry **1**), i.e., **1** is comparatively less catalytically active than **3a**. The GPC trace of the corresponding polyester also shows evidence of the formation of low molecular weight polyester (3282 D) with a broader dispersity value (**Figure S45**).

Empower 2 software

GPC Report

SAMPLE INFORMATION

Sample Name:	RKR SD CHO PA 1 TPPCl NEAT	Acquired By:	System
Sample Type:	Broad Unknown	Sample Set Name:	
Vial:	1	Acq. Method Set:	RI
Injection #:	1	Processing Method:	NEWPM
Injection Volume:	10.00 ul	Channel Name:	410
Run Time:	50.0 Minutes	Proc. Chnl. Descr.:	410
Date Acquired:	10-05-2025 12:56:20 IST		
Date Processed:	10-05-2025 14:53:29 IST		

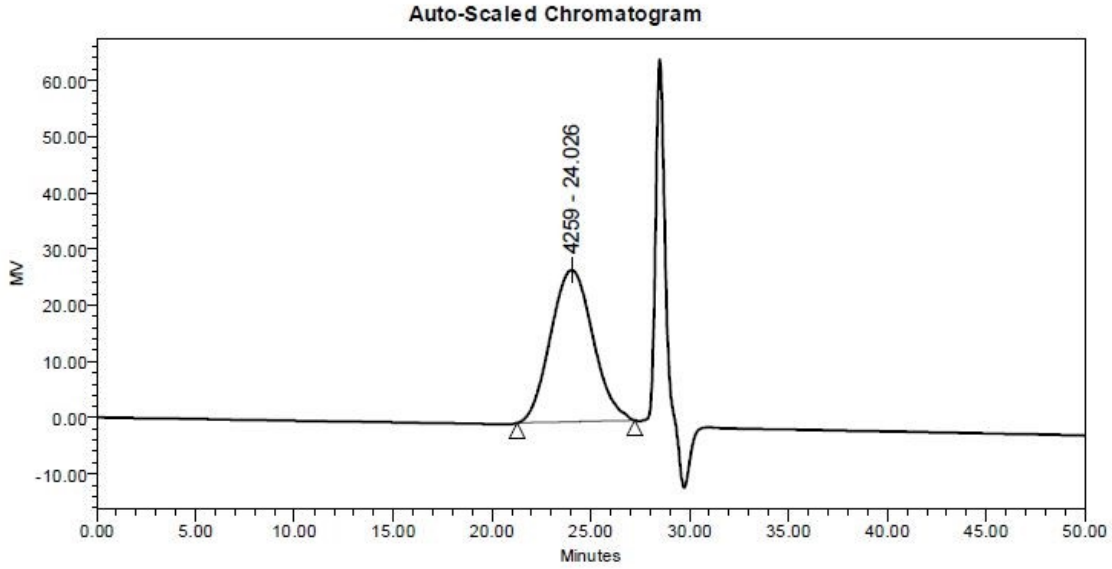

GPC Results

	Dist Name	Mn	Mw	MP	Mz	Mz+1	Mv	Polydispersity	MW Marker 1	MW Marker 2
1		3282	4752	4259	6340	7943		1.447833		

Figure S46. GPC trace of polyester obtained by **1** and TPPCl.

Empower 2 software

GPC Report

SAMPLE INFORMATION

Sample Name:	RKR SD Se CHO PA PPNCl	Acquired By:	System
Sample Type:	Broad Unknown	Sample Set Name:	
Vial:	1	Acq. Method Set:	RI
Injection #:	1	Processing Method:	NEWPM
Injection Volume:	10.00 ul	Channel Name:	410
Run Time:	50.0 Minutes	Proc. Chnl. Descr.:	410
Date Acquired:	20-05-2025 14:24:18 IST		
Date Processed:	20-05-2025 15:18:03 IST		

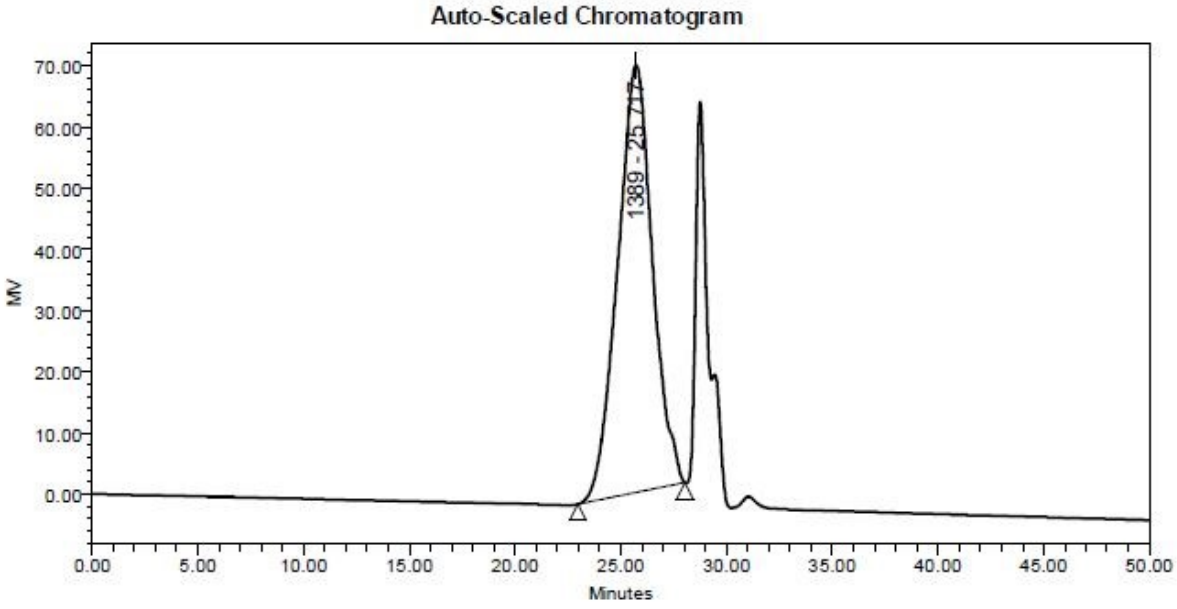

GPC Results

	Dist Name	Mn	Mw	MP	Mz	Mz+1	Mv	Polydispersity	MW Marker 1	MW Marker 2
1		1155	1625	1389	2158	2724		1.406483		

Figure S47. GPC trace of polyester obtained by **2** and TPPCl.

Table S20. ROCOP of CHO with PA using **3b** as a catalyst.

Entry	Catalyst	Cocat.	Solvent	Temperature (°C)	Time (h)	PA Conv. (%)	Ester (%)	M_n (g/mol)	PDI
1	**3b**	TPPCl	Neat	100	8	99	56	1155	1.40

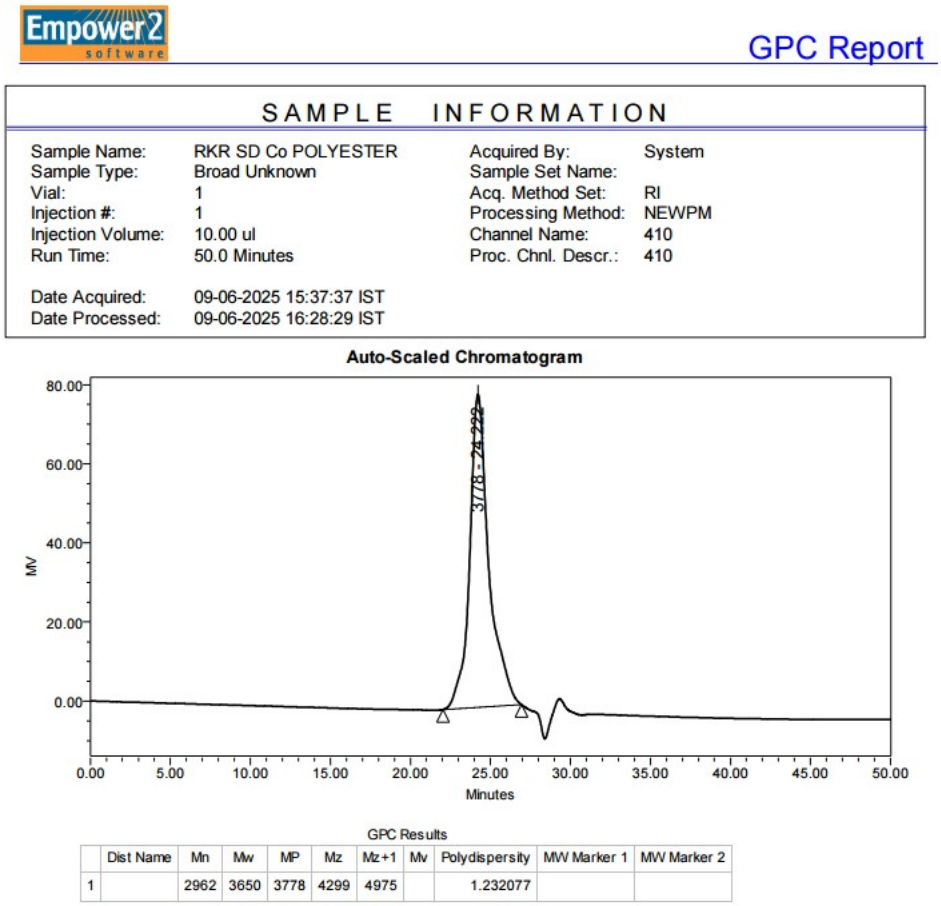

Figure S48. GPC trace of isolated polyester (CHO/PA) using **3a** in n-hexane.

Table S21. ROCOP of CHO with PA using **3a** as a catalyst in n-hexane.

Entry	Time (h)	Solvent	Temperature (°C)	Cocat.	PA Conv. (%)	Ester (%)	M_n (GPC) (g/mol)	[$Đ$]^e	TOF (h^{-1})
1	1	n-hexane	80	TPPCl	> 99	83	2962	1.23	166

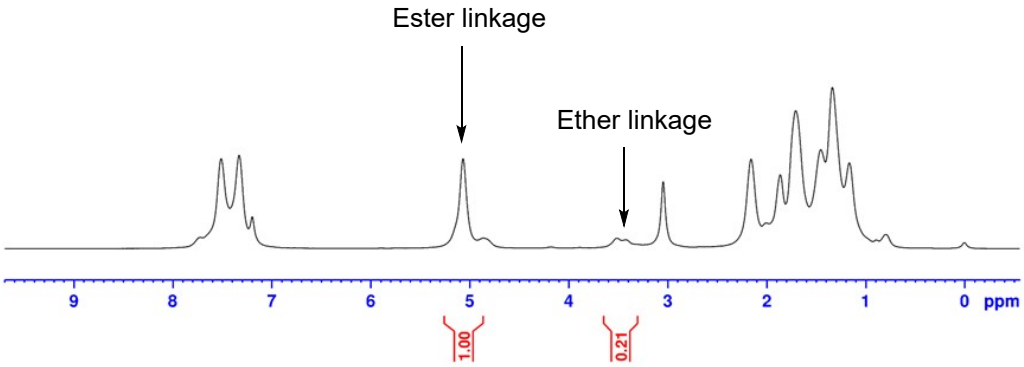

Figure S49. ^{1}H NMR ($CDCl_3$, 500 MHz) spectrum of the crude polyesters of CHO/PA with **3a** in n-hexane.

14. Additional characterizations of [Co^{II}(cAAC)(SS-NHC=Se)Cl] (3b)

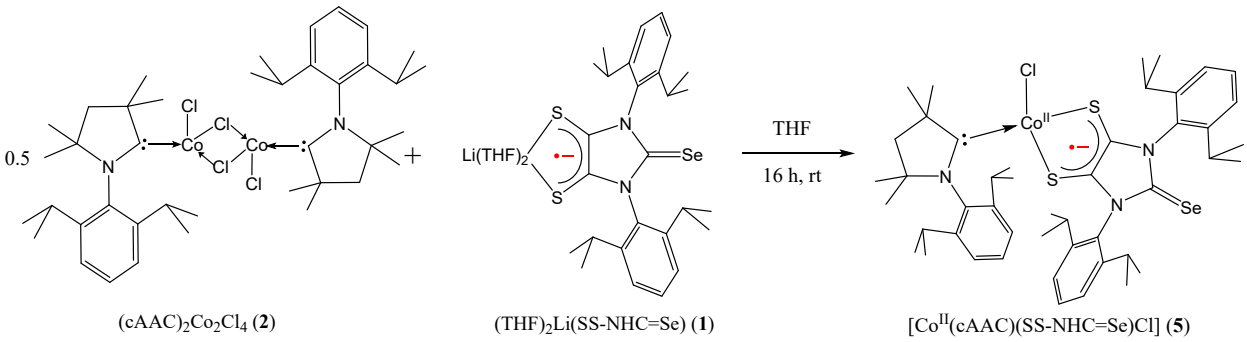

$(cAAC)_2Co_2Cl_4$ (**2**) $(THF)_2Li(SS\text{-}NHC{=}Se)$ (**1**) [Co^{II}(cAAC)(SS-NHC=Se)Cl] (**5**)

Scheme S2. Synthesis of cobalt complex Co^{II}(cAAC)(SS-NHC=Se)Cl] (**3b**).

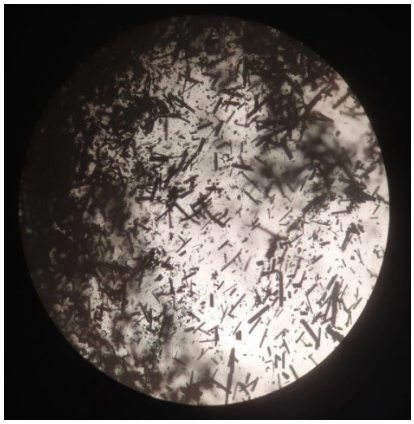

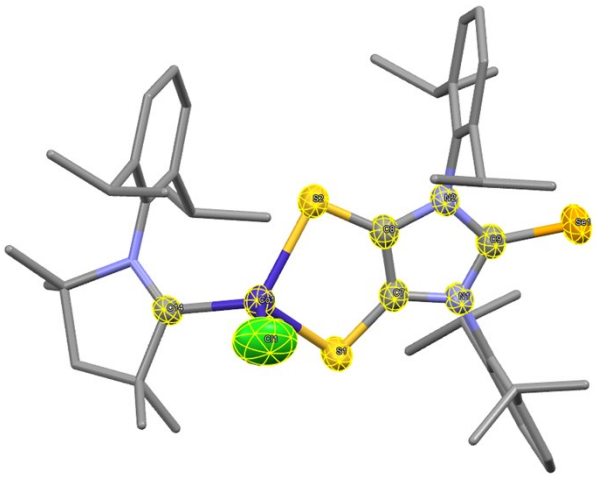

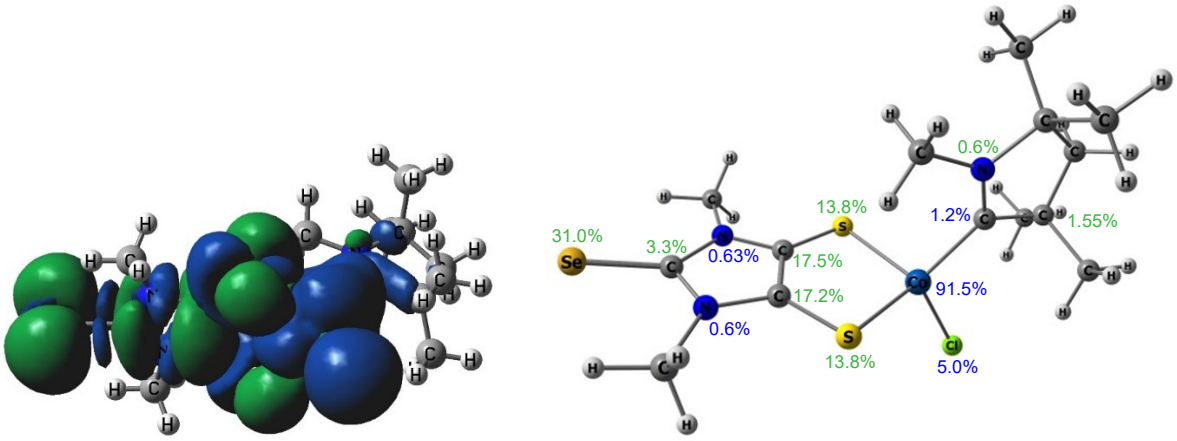

Figure S50. Single crystals (top left) and molecular structure (top right) of [Co^{II}(cAAC)(SS-NHC=Se)Cl] (**3b**) (top). Mulliken spin densities (bottom left) and numerical values on individual atoms of **3b′** [in triplet state S = 1; Dip group has been replaced with Me in **3b′**].

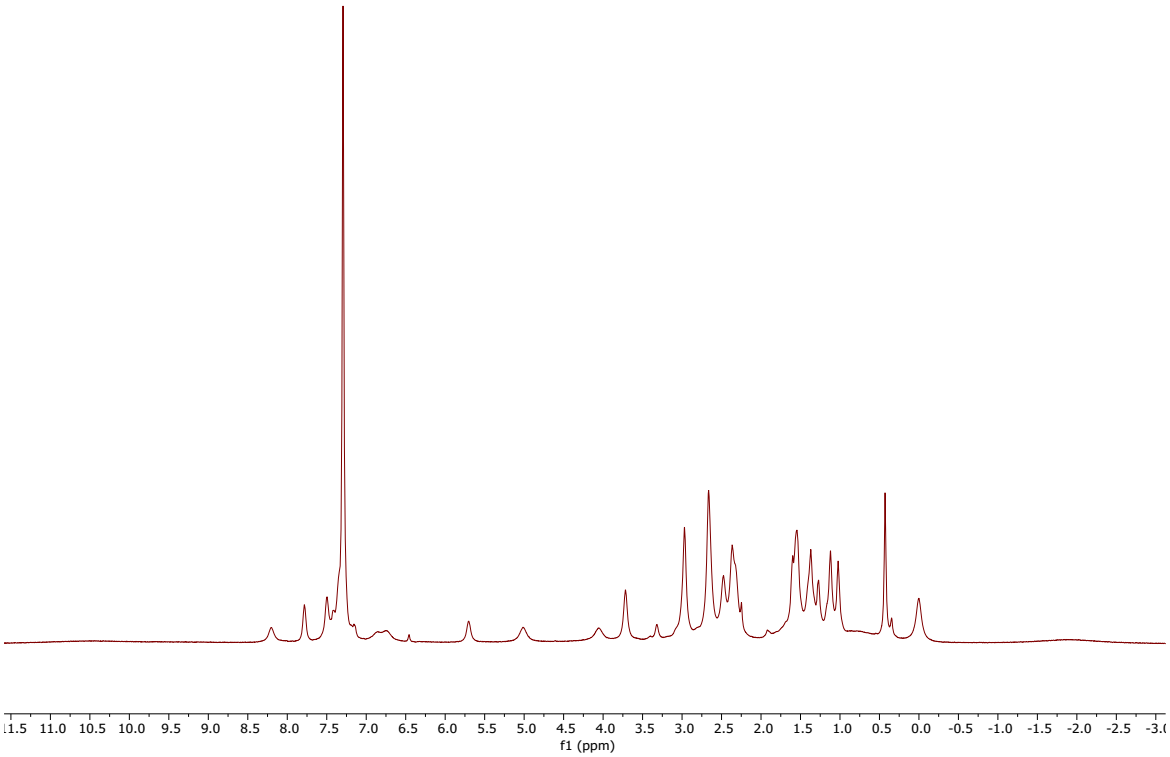

Figure S51. ^{1}H NMR spectrum of complex [Co^{II}(cAAC)(SS-NHC=Se)Cl] (**3b**) in C_6D_6 at room temperature (500 MHz). 15 mg of sample (**3b**) dissolved in 0.5 mL of C_6D_6.

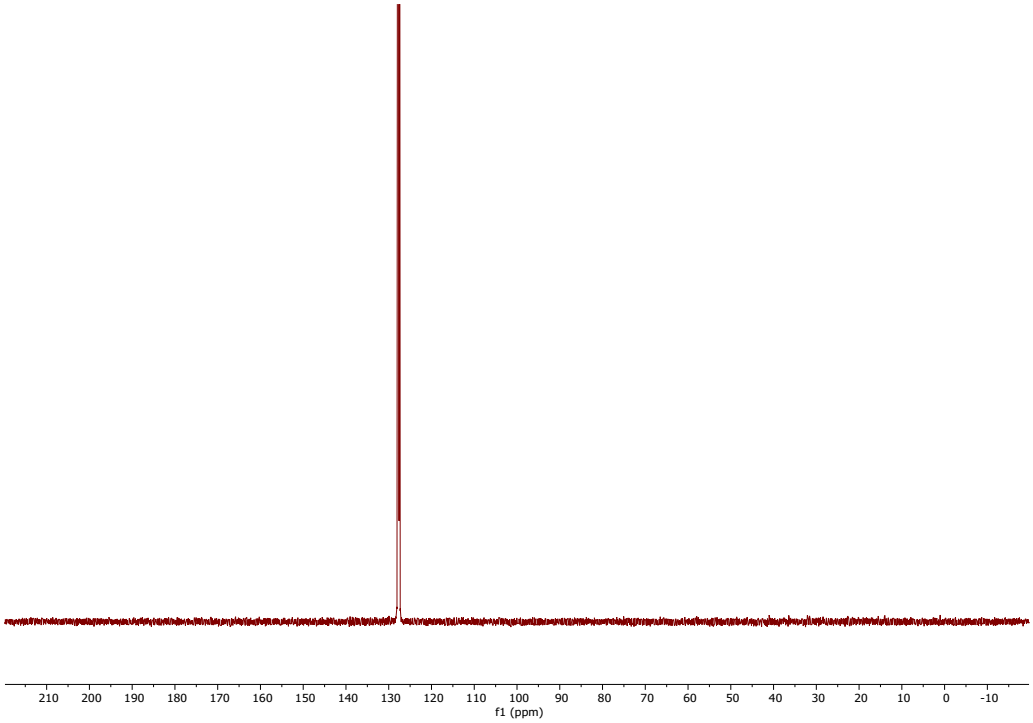

Figure S52. ^{13}C NMR spectrum of complex [Co^{II}(cAAC)(SS-NHC=Se)Cl] (**3b**) in C_6D_6 at room temperature (500 MHz). 15 mg of sample (**3b**) dissolved in 0.5 mL of C_6D_6.

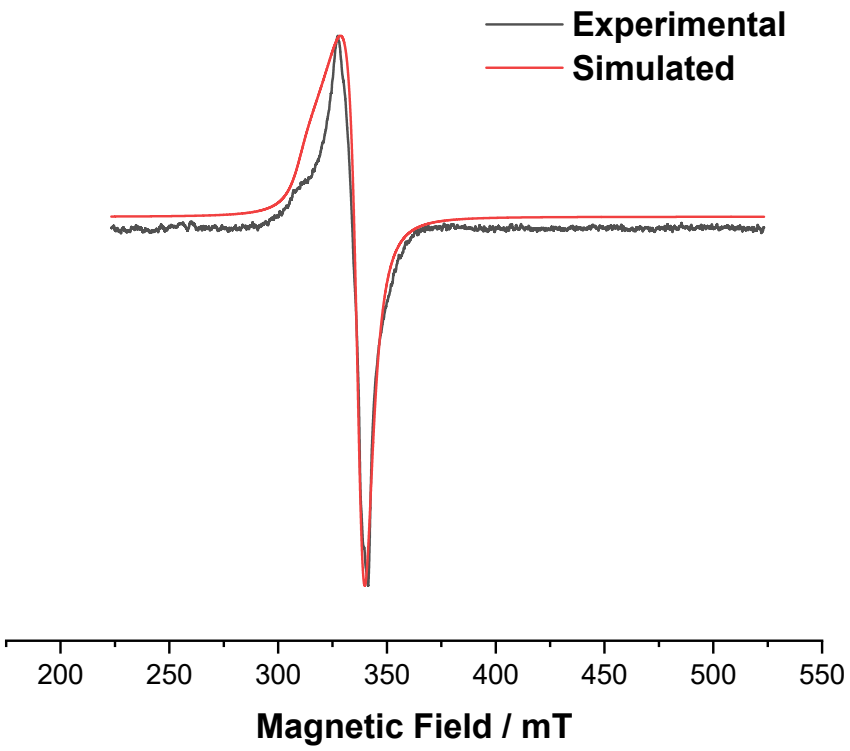

Figure S53. X-Band solid state EPR spectrum (black) of the complex **3b** at room temperature. Red and black lines represent the simulated and the experimental spectra of the complex (**3b**), and the simulation is done using EasySpin program. [$\mathbf{g_{\parallel}}$ = 2.10453, $\mathbf{g_{\perp}}$ = 2.00069, LWPP (Gaussian broadening) = 1.40278 mT, LWPP (Lorentzian broadening) = 6.27063 mT, $A_{\parallel}(^{59}Co)$ = 79.5418 MHz, X-band experimental frequency = 9.446002 GHz].

$$g_{iso} = \sqrt{\frac{{g_{\parallel}}^2 + 2{g_{\perp}}^2}{3}} = \sqrt{\frac{2.10453^2 + 2 \times 2.00069^2}{3}} = 2.035891899$$

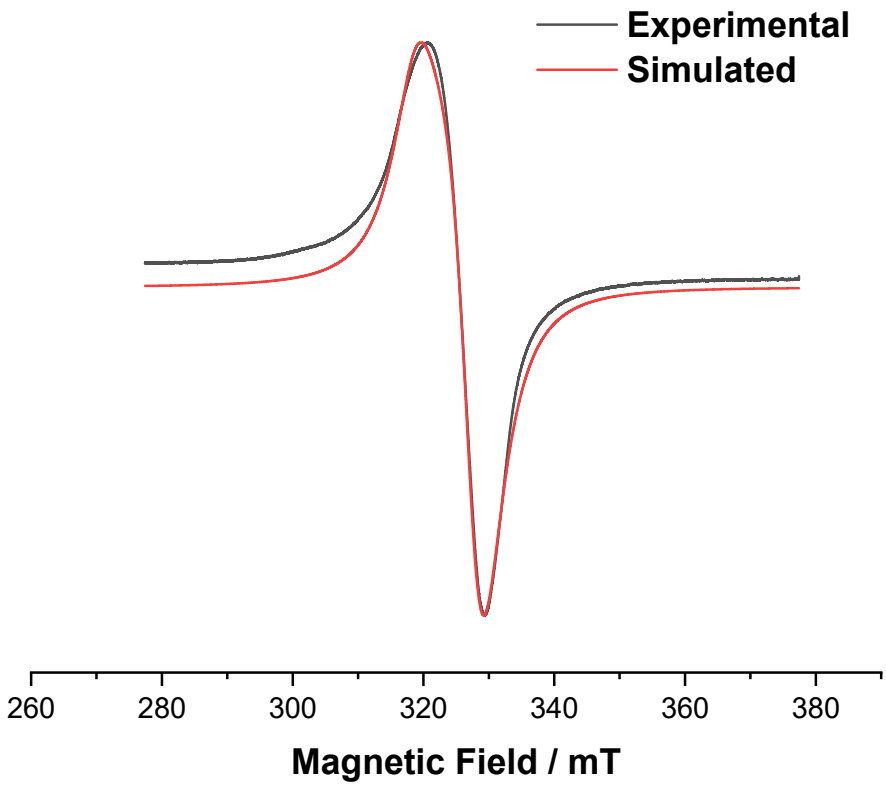

Figure S54. X-Band solid state EPR spectrum (black) of the complex **3b** at 77 K. Red and black lines represent the simulated and the experimental spectra of the complex (**3b**), and the simulation is done using the EasySpin program. [$\mathbf{g}_{\parallel}$ = 2.05688, $\mathbf{g}_{\perp}$ = 2.00211, LWPP (Gaussian broadening) = 0.00285928 mT, LWPP (Lorentzian broadening) = 5.33296 mT, X-band experimental frequency = 9.176029 GHz].

$$g_{iso} = \sqrt{\frac{{g_{\parallel}}^2 + 2{g_{\perp}}^2}{3}} = \sqrt{\frac{2.05688^2 + 2 \times 2.00211^2}{3}} = 2.020531633$$

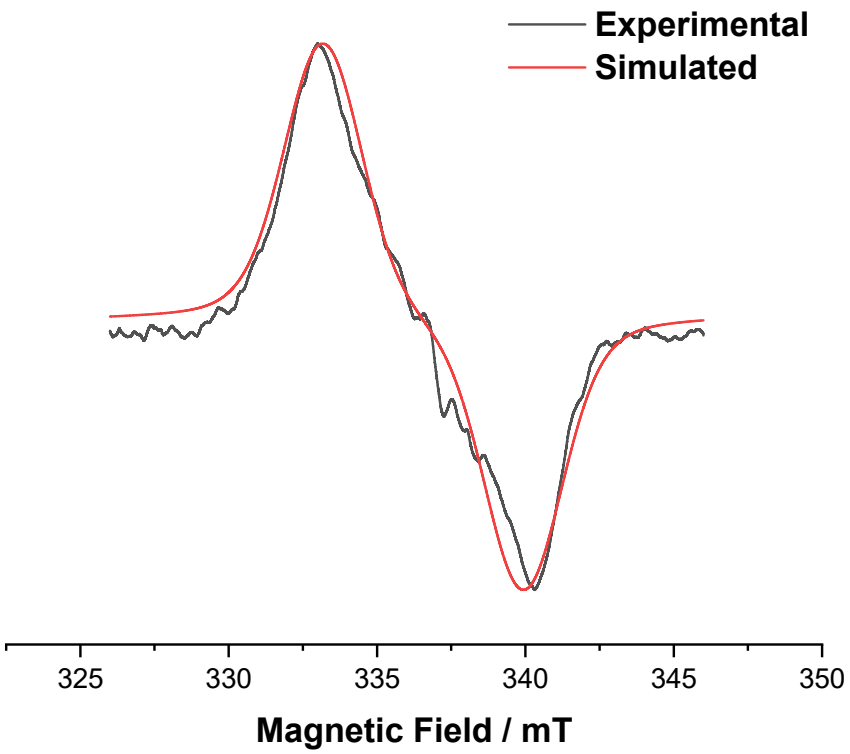

Figure S55. X-Band EPR spectrum (black) of the polymerization reaction of **3a** after 30 min at room temperature in THF. Red and black lines represent the simulated and the experimental spectra, and the simulation is done using the EasySpin program. [$\mathbf{g_{iso}}$ = 2.00598, LWPP (Gaussian broadening) = 2.32278 mT, LWPP (Lorentzian broadening) = 0.500663 mT, **A**. (^{59}Co) = 23.6904 MHz, X-band experimental frequency = 9.449265 GHz].

……..

15. Raman Spectra

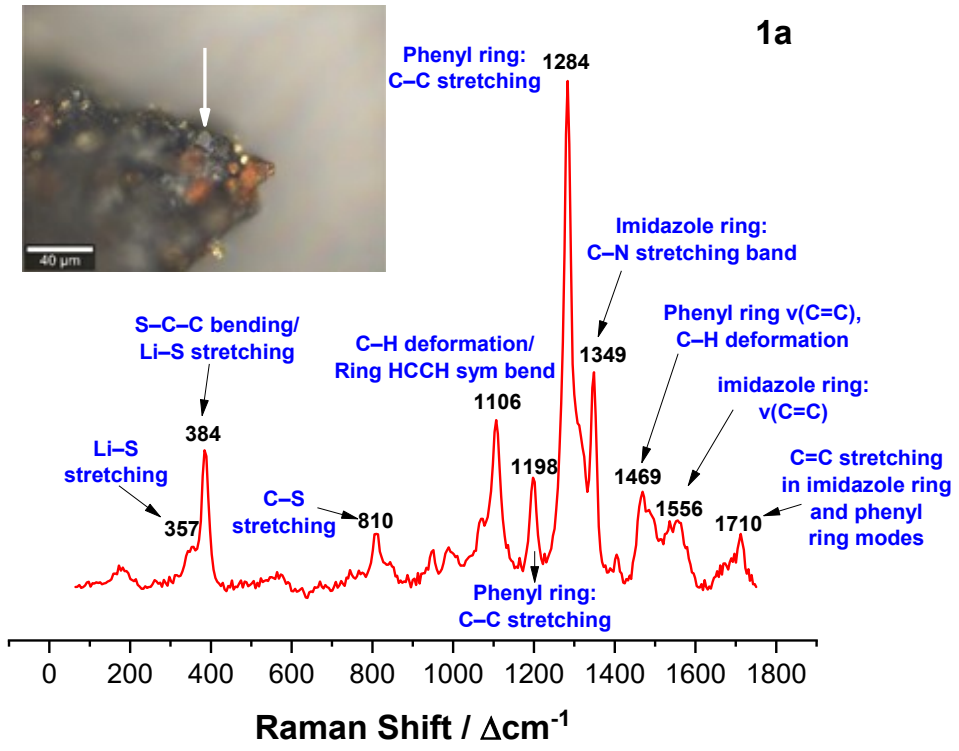

Figure S56. Solid state Raman spectrum of **1a**, $(THF)_2Li(SS\text{-}NHC{=}S)$, measured in alpha300 R Raman Microscope. The white arrow shows where the laser beam has been focussed (on the dark crystal of **1**) to record the Raman spectrum.

Table S22. Assignments of bands of **1.**

Band (cm^{-1})	**Intensity**	**Assignment of bands**	**Reference range (cm^{-1})**	**Reference**
357	Weak	Li–S stretching	350–500	S18
384	Medium	S–C–C bending/Li–S stretching	364, 350–500	S18-S19
810	Weak	C–S stretching	813	S20
1106	Medium	C–H deformation/ring HCCH sym bend	1106	S20
1198	Medium	Phenyl ring: C–C stretching	1195–1197	S20
1284	Very strong	Phenyl ring: C–C stretching	1280–1292	S20
1349	Medium	Imidazole ring: C–N stretching band	1341–1346	S20
1469	Medium	Phenyl ring ν(C=C), C–H deformation	1448–1457	S20
1556	Weak	Phenyl ring: ν(C=C)	1552–1564	S20
1710	Weak	C=C stretching in imidazole ring and phenyl ring modes	1300–1750	S20

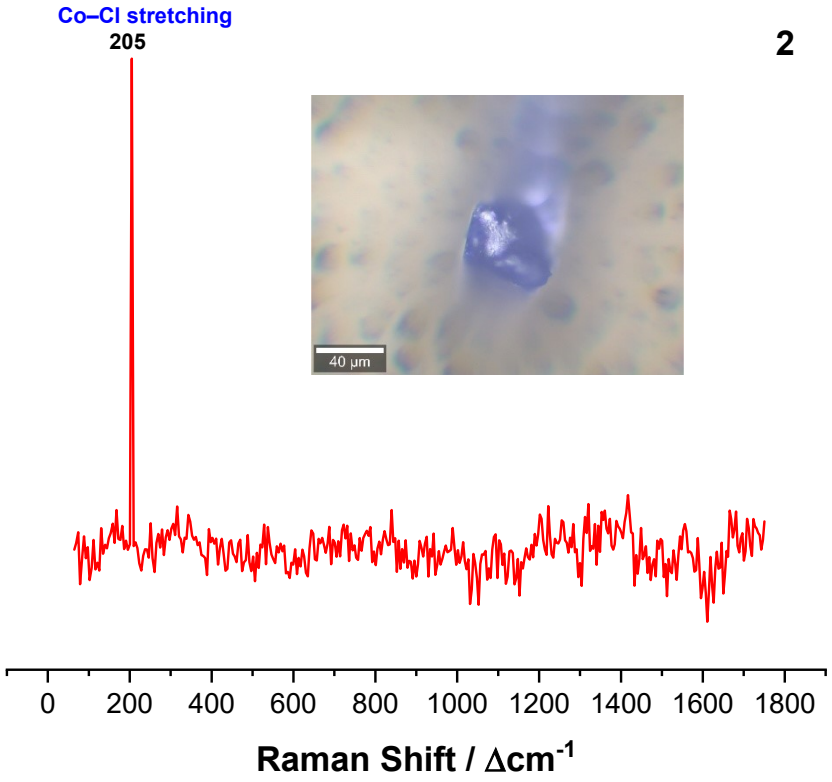

Figure S57. Solid state Raman spectrum of **2**, $(cAAC)_2Co_2Cl_4$, measured in an alpha300 R Raman Microscope. Proper Raman signals were not obtained due to the amorphous nature of **2**. Single crystals generally produce the best intensity in our machine.

Table S23. Assignments of bands of **2**.

Band (cm^{-1})	**Intensity**	**Assignment of bands**	**Reference range (cm^{-1})**	**Reference**
205	Very strong	Co–Cl stretching	237	S21

Table S24. Assignments of bands of **3a**.

Band (cm^{-1})	**Intensity**	**Assignment of bands**	**Reference range (cm^{-1})**	**Reference**
97	Weak	Co–Cl stretching	87	S21
205	Weak	Co–Cl stretching	237	S21
256	Medium	Co–Cl stretching	255	S21
293	Weak (shoulder)	Co–S stretching	288, 297	S19, S21
389	Medium	S–C–C bending	364	S19
560	Medium	C–S stretching	570–750	S22
1152	Weak	C–H deformation	1151–1163	S20
1271	Very strong	Phenyl ring: C–C stretching	1280–1292	S20
1324	Weak	Imidazole ring: C–N stretching	1320–1328	S20
1352	Weak	Imidazole ring: C–N stretching	1341–1348	S20
1377	Weak	Imidazole ring: C–N stretching	1387–1391	S20
1540	Weak	Phenyl ring: ν(C=C)	1532–1540	S20

Table S25. Assignments of bands of **3b**.

Band (cm^{-1})	**Intensity**	**Assignment of bands**	**Reference range (cm^{-1})**	**Reference**
88	Weak	Co–Cl stretching	87	S21
163	Weak	Co–S–C deformation	141	S21
205	Medium	Co–Cl stretching	237	S21
233	Weak	Co–Cl stretching	237	S21
279	Strong	Co–S stretching	297	S21
635	Weak	C–S stretching	570–750	S22
714	Weak	C–S stretching	570–750, 716	S22, S21
930	Very weak	C=Se stretching	940	S21-S22
967	Very weak	C=Se stretching	995	S21-S22
1230	Very strong	Phenyl ring: C–C stretching	1231–1242	S20
1292	Medium	Phenyl ring: C–C stretching	1280–1292	S20
1332	Strong	Imidazole ring: C–N stretching	1341–1348	S20
1580	Strong	Phenyl ring: ν(C=C)	1552–1564	S20

Solid-state Raman spectra of complexes **1**, **2**, **3a**, and **3b** were recorded using an alpha300 R Raman microscope. For each sample, the most crystalline regions were identified and selected for spectral acquisition, as indicated in the corresponding optical micrographs (scale bar: 40 μm).

Complex **1**, the precursor bearing the dithiolene ligand $(THF)_2Li$(SS-NHC=S), exhibits characteristic Li–S stretching vibrations in the Raman spectrum at 357 cm^{-1} and 384 cm^{-1}, consistent with previous reports.[S18] The band at 384 cm^{-1} may also be attributed to S–C–C bending, which has been reported at 364 cm^{-1} by Jarzęcki *et al*. [S19] The slight shift in the observed frequency is likely due to differences in the ligand environment between the two systems. The Raman spectrum of complex **1** also exhibits a C–S stretching vibration at 810 cm^{-1}, consistent with the previously reported value of 813 cm^{-1} by Boumediene *et al.*, [S20] confirming the presence of the dithiolene ligand. A prominent band at 1106 cm^{-1} corresponds to C–H deformation or symmetric HCCH ring bending, also in agreement with the literature. [S20] The C–C stretching modes of the phenyl ring appear at 1198 cm^{-1} (medium) and 1284 cm^{-1} (very strong), while the C=C stretching vibrations are observed at 1469 cm^{-1} (medium) and 1556 cm^{-1} (weak); the band at 1469 cm^{-1} may also contain contributions from C–H deformation. A medium-intensity band at 1349 cm^{-1} is attributed to the C–N stretching vibration of the imidazole ring. Additionally, a weak band at 1710 cm^{-1} is assigned to C=C stretching associated with both the imidazole and phenyl rings.

The Raman spectrum of complex **2**, $(cAAC)_2Co_2Cl_4$, displays a single prominent band at 205 cm^{-1}, which is attributed to the Co–Cl stretching vibration. This mode appears at a slightly lower frequency compared to that reported for $[CS(NH_2)_2]_2 \cdot CoCl_2$ in the literature, likely due to differences in the coordination environment. Despite the structural variation, the assignment remains consistent, as both systems feature cobalt–chloride bonding within a similar vibrational context.

The Raman spectrum of complex **3b**, [Co(II)(cAAC)(SS-NHC=Se)Cl], closely resembles that of complex **3a**, with key differences arising from the replacement of the C=S group with a C=Se moiety in the ligand framework. Several low-frequency bands are observed that are attributable to metal–ligand interactions. A weak band at 88 cm^{-1} and a medium-intensity band at 205 cm^{-1}, along with a weak shoulder at 233 cm^{-1}, correspond to Co–Cl stretching vibrations, in agreement with the reported values.[S21] A weak band at 163 cm^{-1} is assigned to Co–S–C deformation, similar to that observed in related systems. [S21] A strong band at 279 cm^{-1} is attributed to the Co–S stretching, consistent with the expected range around 297 cm^{-1}. [S21] The C–S stretching vibrations are observed as weak features at 635 cm^{-1} and 714 cm^{-1}, in line with reported ranges of 570–750 cm^{-1} and with specific reference to the 716 cm^{-1} peak in comparable dithiolene-type ligands. [S21-S22] Two very weak bands at 930 cm^{-1} and 967 cm^{-1} are assigned to C=Se stretching vibrations, corresponding to values near 940–995 cm^{-1} in

selenium-containing analogues.[S20-21] Ligand-based vibrations include phenyl ring C–C stretching bands at 1230 cm^{-1} (very strong) and 1292 cm^{-1} (medium), which fall within the typical 1231–1242 and 1280–1292 cm^{-1} ranges, respectively. [S20] A strong band at 1332 cm^{-1} is attributed to the C–N stretching mode of the imidazole ring, consistent with the 1341–1348 cm^{-1} region. [S20] Finally, a strong peak at 1580 cm^{-1} is assigned to the C=C stretching mode of the phenyl ring, within the expected range of 1552–1564 cm^{-1}. [S20]

Complexes **3a** and **3b** are derived from the combination of precursor complexes **1** and **2**, and their Raman spectral features reflect contributions from both parent units. Complex **1**, which contains the dithiolene ligand $(THF)_2Li$(SS-NHC=S), exhibits characteristic Li–S stretching vibrations at 357 and 384 cm^{-1}, alongside a C–S stretch at 810 cm^{-1} and various ligand-based modes including imidazole C–N and phenyl C–C/C=C vibrations. Complex **2**, $(cAAC)_2Co_2Cl_4$, contributes a dominant Co–Cl stretching vibration at 205 cm^{-1}. Upon coordination to form complex **3a**, [Co(II)(cAAC)(SS-NHC=S)Cl], the Li–S bands are no longer observed, and new Co–S stretching bands emerge, with a weak shoulder at 293 cm^{-1}, consistent with metal–sulphur coordination. The Co–Cl bands are retained and slightly shifted, observed at 97, 205, and 256 cm^{-1}, with the shifts attributable to the change from a dimeric Co–Cl environment in **2** to a mononuclear Co centre in **3a**. Ligand-based bands such as C–N, C–C, and C=C stretching modes are largely preserved, though small frequency shifts are observed due to the altered electronic environment around the ligand. In complex **3b**, where the sulphur atom in the C=S group is replaced by selenium (C=Se), additional bands at 930 and 967 cm^{-1} emerge, corresponding to C=Se stretching vibrations. The Co–S stretching band shifts to 279 cm^{-1} and is notably stronger for **3b** than in **3a**. C–S bands in **3b** appear at 635 and 714 cm^{-1}, slightly higher than in **3a**, likely due to the influence of the adjacent selenium atom on the sulphur bonding framework. Phenyl and imidazole-associated vibrational features remain largely consistent across **3a** and **3b**, with slight upshifts observed in **3b**, potentially due to the overall increase in ligand mass and subtle electronic redistribution introduced by selenium substitution. Collectively, the Raman data confirm successful complex formation and provide insights into how the coordination environment and ligand modifications influence metal–ligand bonding and vibrational behaviour.

16. Other measurements:

Notably, the solution initially exhibited a peak near 598 nm of complex **3a**, which gradually decreased in intensity over time. This decrease in absorbance correlates with the fading of the solution's color, which eventually became colorless after prolonged heating at 120 °C for 10 h.

We have included both the time-dependent color changes and the corresponding UV-vis spectra to clearly illustrate the thermal degradation process of the complex in solution.

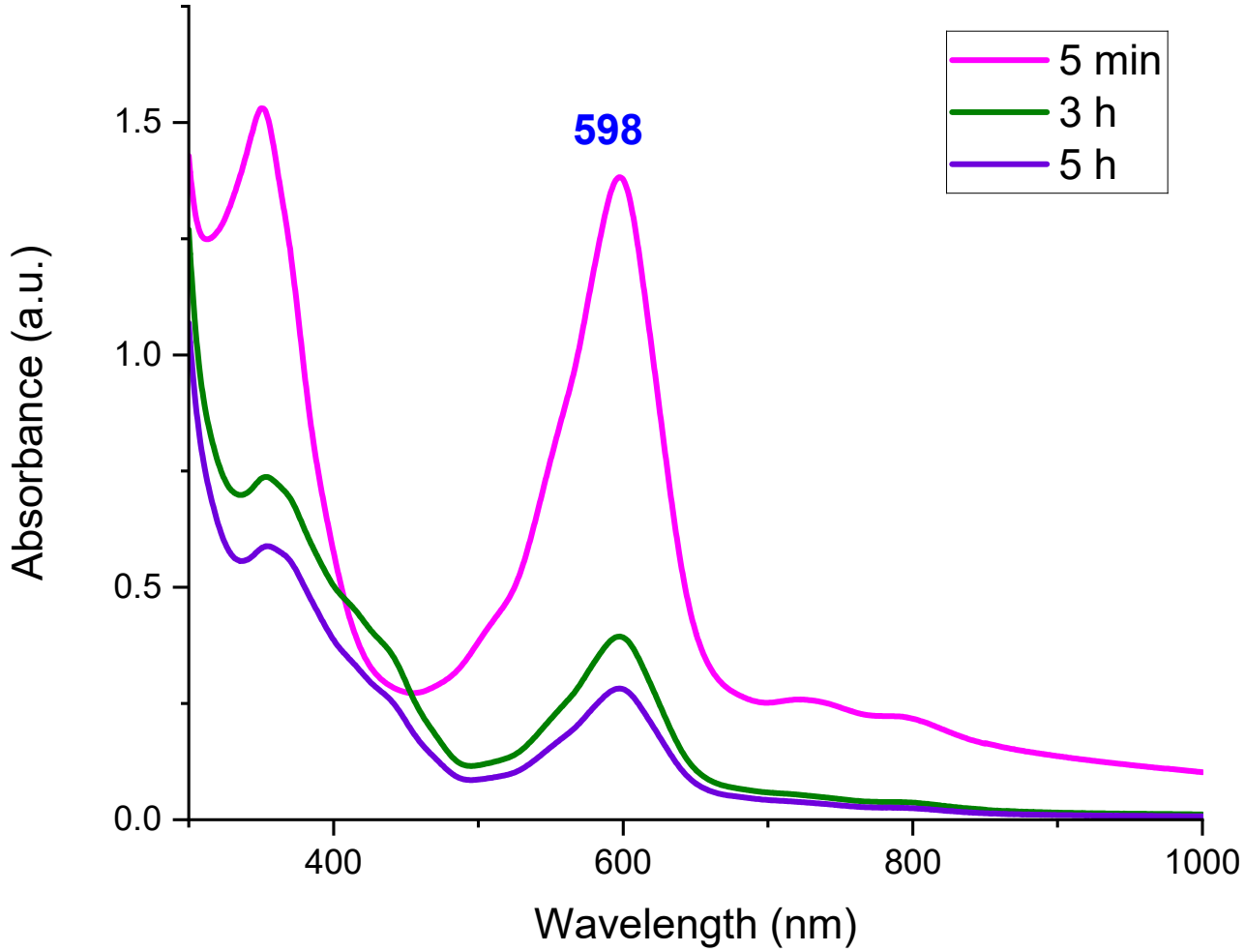

Figure S58. UV-Vis absorption spectrum of THF solutions of complex [Co^{II}(cAAC)(SS-NHC=S)Cl] (**3a**) at 120 °C at different time intervals.

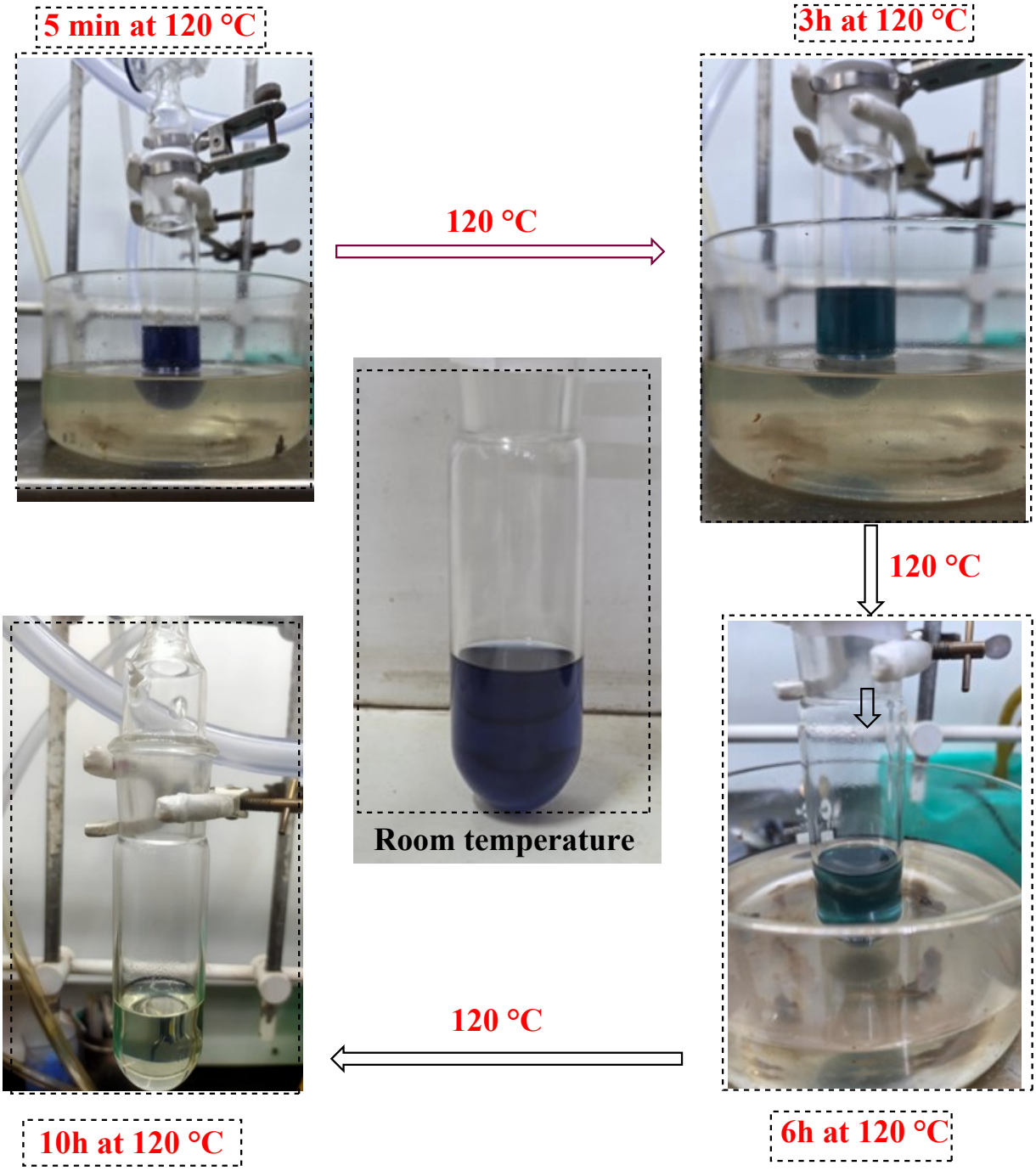

Figure S59. Variation of colors of THF solutions of complex [Co^{II}(cAAC)(SS-NHC=S)Cl] (**3a**) at 120 °C at different time intervals.

……

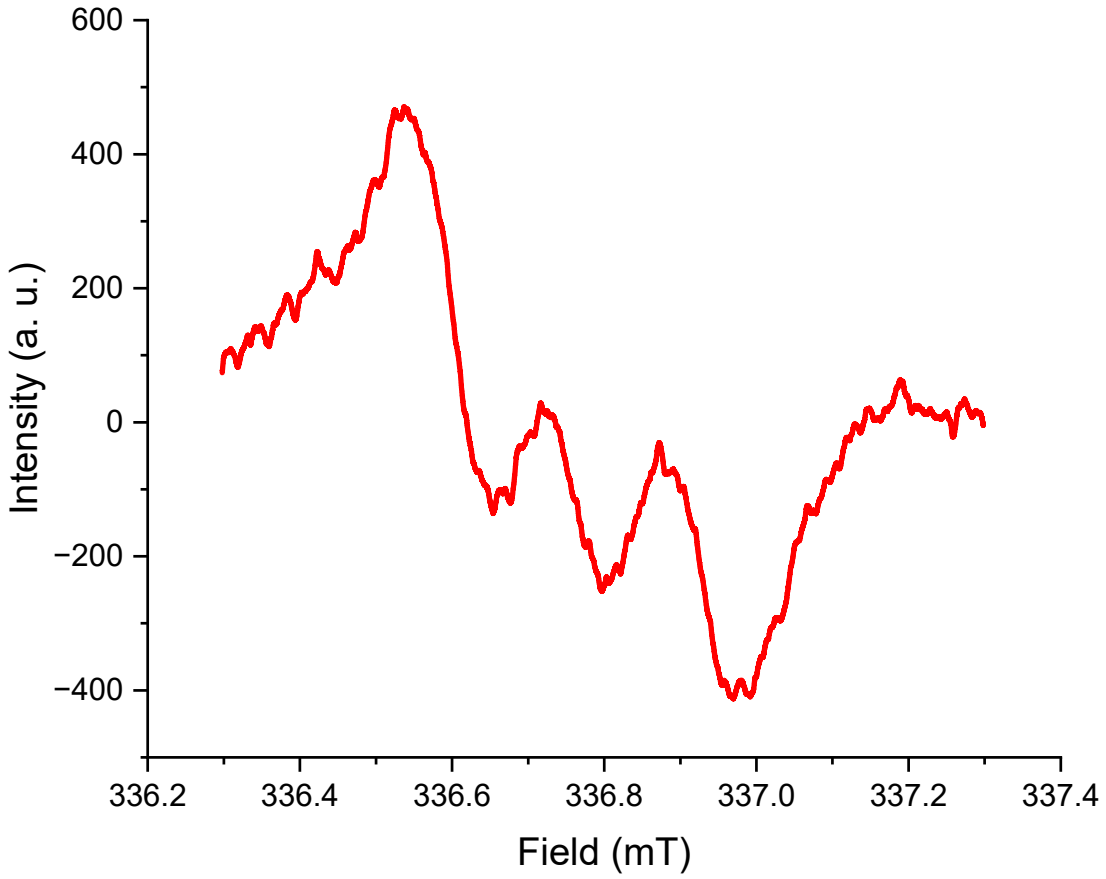

Figure S60. X-Band EPR spectrum of $(cAACH)_2[Co^{II}Cl_4]$ at room temperature in THF solution.

When complex **3a** is exposed to air, as indicated by the UV-vis spectral changes after 12-14 hours. The reviewer also raises an important point about whether the transformation corresponds to a simple one-electron oxidation to form species 3^+, as might be suggested by the cyclic voltammetry (CV) data.

To address this, we conducted a follow-up experiment in which a THF solution of complex **3a** was exposed to open air for 15 hours. After concentrating the solution, we added a small amount of hexane to induce crystallization. Crystals formed after one day, and two distinct types were observed:

1. **Sky-blue crystals**, identified by single-crystal X-ray diffraction (SCXRD) as **$[2(cAAC)H^+][CoCl_4^{2-}]$**, which corresponds to a protonated cAAC ligand paired with a **$CoCl_4^{2-}$** counterion.
2. **Light brown crystals**, also characterized by SCXRD, were found to be a **dimeric product** $(SS\text{-}NHC{=}S)_2$ **of the radical ligand 2**, likely formed via dimerization of the neutral form of the ligand (SS-NHC=S) in solution.

Both structures, mentioned above, have been previously reported in the literature. As a result, we did not go for a full data collection but collected fast-scan SCXRD data to confirm their identities of those chemical species of concern.

Based on these findings, we conclude that the transformation of complex **3a** upon exposure to air led to the one-electron oxidized form ($\mathbf{3}^{+}$) from which the neutral SS-NHC=S ligand to form previously reported light-brown colored dimeric product $(SS\text{-}NHC{=}S)_2$. The cyclic voltammetry suggests that complex **3** can be electro-chemically oxidized to $\mathbf{3}^{+}$ which could be short-lived species in solution.

We hope this addresses the reviewer's question and provides clarity on the nature of the species observed after prolonged air exposure. It is worth to mention that the *n*-hexane solution of complex **3** is does not undergo rapid oxidation. Long needles of complex **3** are formed after *n*-hexane solution of complex **3** was stored in open air. It has been structurally characterized. We have collected full SCXRD data at 298 K Kindly see ESI. The dark plates **3** (obtained from n-hexane solution under argon atmosphere) and long needle of **3** grown from n-hexane solution in open air are polymorphic in nature. They crystallize in different crystal systems [triclinic, orthorhombic] and space groups [*P*-1, *P*bca]. The bond parameters are slightly different [kindly see ESI].

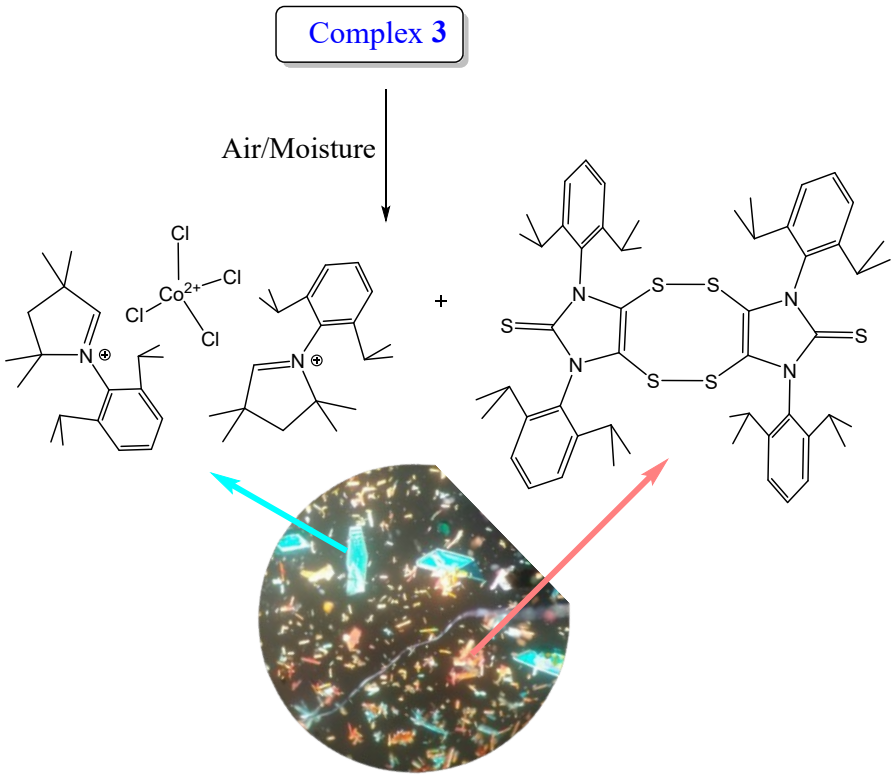

Figure S61. Proposed decomposition pathway of complex **3a** upon air exposure in THF, leading to the formation of $[2(cAACH^{+})][CoCl_4^{2-}]$, and a dimeric product of the radical ligand **2**. Molecular structures were confirmed by SCXRD.

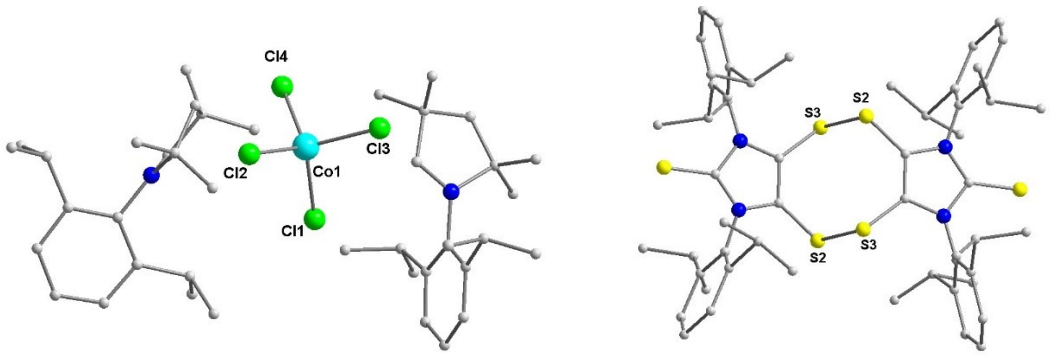

a) **[2(cAAC)H$^+$][CoCl$_4^{2-}$]** b) **(SS-NHC=S)$_2$**

Figure S62. Single-crystal X-ray diffraction (SCXRD) analysis of the products formed from the air exposure of Complex **3**. (a) Sky-blue crystals corresponding to [2(cAAC)H$^+$][CoCl$_4^{2-}$], and (b) light brown crystals corresponding to the dimeric product of the radical ligand **2**. The molecular structures were confirmed, and the data were collected in fast-scan mode and refined.

We appreciate the reviewer's comment regarding the potential implications of **3** and **1** for PDC reactivity. To investigate this, we tested **1** as a catalyst under standard reaction conditions. However, **1** did not effectively promote the reaction, suggesting that, despite the observed stability of **3** in air, **1** lacks the necessary catalytic activity under these conditions. We have given a report on the ROP reactivity of **1**.

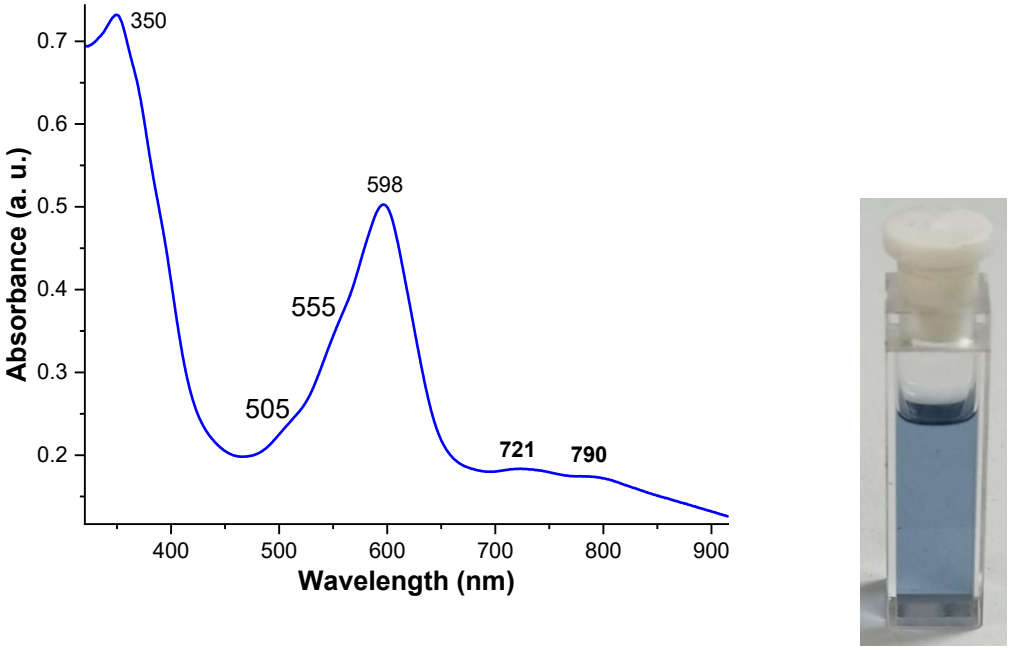

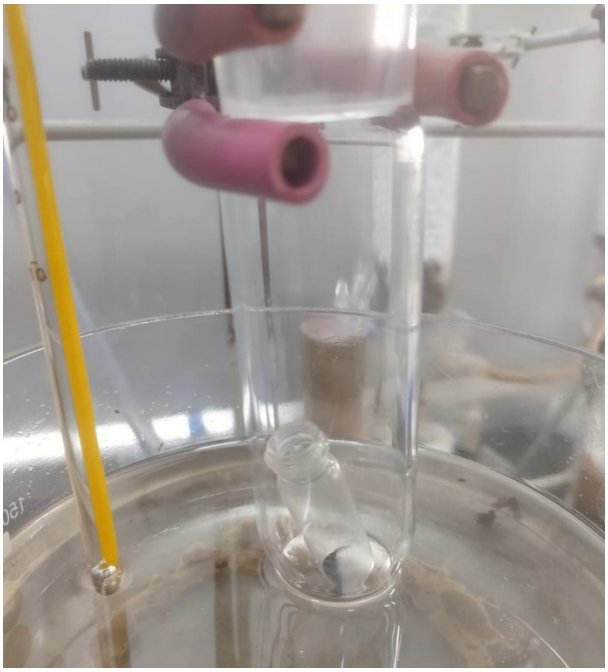

Figure S63. UV-Vis spectra of complex **3** recorded in THF. First, the solid samples of **3a** were heated at 120 °C under an argon atmosphere for 1.5 hours. It does not change color during heating. Corresponding reference spectra are shared for comparison.

For clarity, the corresponding UV-Vis spectra are provided below.

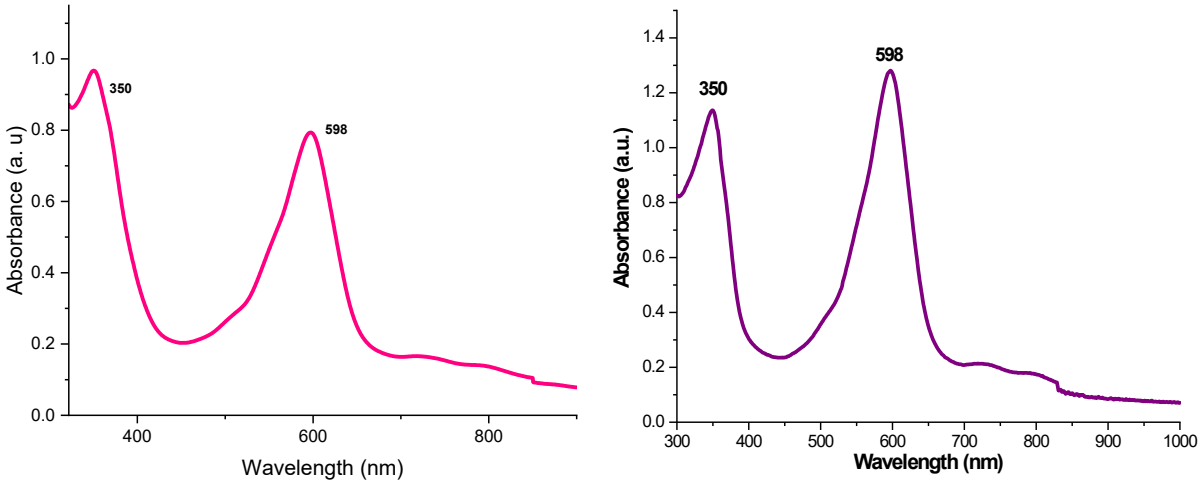

Figure S64. UV-Vis absorption spectra of complex **3a** (right) and the product formed upon reaction of complex **3a** with Cp_2Co^+ (left).

Subsequently, we employed a stronger oxidant, $NO^+BF_4^-$, to assess the oxidation behavior of complex **3**. In this case, we observed an immediate and distinct color change from the characteristic bright blue of complex **3** to a light brownish-green solution within 15 minutes. This transformation occurred consistently at both low and room temperature, indicating a clear alteration in the electronic environment.

Despite this visible change, analytical data provided no evidence for oxidation at the cobalt center or the formation of a Co(III) species. Instead, the results suggest that the oxidation is ligand-centered, leading to a subsequent structural or electronic transformation.

For clarity, we have included photographs of the reaction flask showing the observed color change. These visual and structural data support our conclusion that, under the conditions studied, oxidation occurs at the ligand and does not lead to the formation of a Co(III) species.

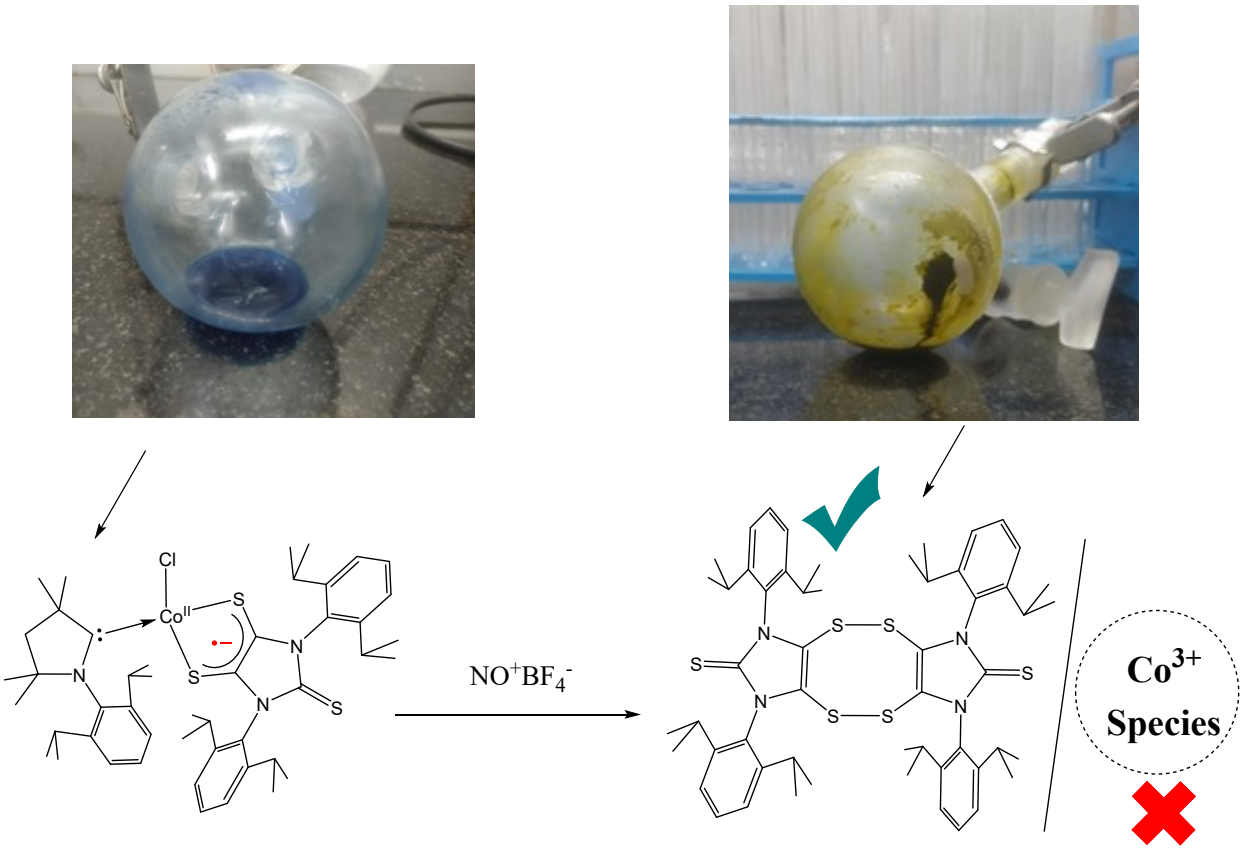

Figure S65. Representation of the reaction between complex **3a** and oxidant ($NO^+BF_4^-$), illustrating the color of the reaction solution before and after the reaction.

17. References

S1. Y. Wang, H. P. Hickox, Y. Xie, P. Wei, S. A. Blair, M. K. Johnson, H. F. Schaefer III and G. H. Robinson, A Stable Anionic Dithiolene Radical. *J. Am. Chem. Soc*., **2017**, 139, 6859−6862.

S2. Becke, A. D. A new mixing of Hartree-Fock and local density-functional theories. *J. Chem. Phys.* **1993**, *98*, 1372-1377.

S3. Stephens, P. J.; Devlin, F. J.; Chabalowski, C. F.; Frisch M. J. Ab Initio Calculation of Vibrational Absorption and Circular Dichroism Spectra using Density Functional Force Fields *J. Phys. Chem.* **1994**, 98, 11623-11627.

S4. Lee, C.; Yang, W.; Parr, R. G. Development of the Colle-Salvetti correlation-energy formula into a functional of the electron density *Phys. Rev. B* **1988**, 37, 785-789.

S5. Grimme, S.; Antony, J.; Ehrlich, S.; Krieg, H. A consistent and accurate ab initio parametrisation of density functional dispersion correction (DFT-D) for the 94 elements H-Pu *J. Chem. Phys*. **2010**, *132*, 154104-154124.

S6. Grimme, S.; Ehrlich, S.; Goerigk, L. Effect of the damping function in dispersion corrected density functional theory. *J. Comput. Chem.* **2011**, *32*, 1456-1465.

S7. Weigend, F.; Ahlrichs, R. Balanced basis sets of split valence, triple zeta valence and quadruple zeta valence quality for H to Rn: Design and assessment of accuracy. *Phys. Chem. Chem. Phys.* **2005**, *7*, 3297-3305.

S8. Gaussian 16, Revision A.03, Frisch, M. J.; Trucks, G. W.; Schlegel, H. B.; Scuseria, G. E.; Robb, M. A.; Cheeseman, J. R.; Scalmani, G.; Barone, V.; Petersson, G. A.; Nakatsuji, H.; Li, X.; Caricato, M.; Marenich, A. V.; Bloino, J.; Janesko, B. G.; Gomperts, R.; Mennucci, B.; Hratchian, H. P.; Ortiz, J. V.; Izmaylov, A. F.; Sonnenberg, J. L.; Williams-Young, D.; Ding, F.; Lipparini, F.; Egidi, F.; Goings, J.; Peng, B.; Petrone, A.; Henderson, T.; Ranasinghe, D.; Zakrzewski, V. G.; Gao, J.; Rega, N.; Zheng, G.; Liang, W.; Hada, M.; Ehara, M.; Toyota, K.; Fukuda, R.; Hasegawa, J.; Ishida, M.; Nakajima, T.; Honda, Y.; Kitao, O.; Nakai, H.; Vreven, T.; Throssell, K.; Montgomery, J. A., Jr.; Peralta, J. E.; Ogliaro, F.; Bearpark, M. J.; Heyd, J. J.; Brothers, E. N.; Kudin, K. N.; Staroverov, V. N.; Keith, T. A.; Kobayashi, R.; Normand, J.; Raghavachari, K.; Rendell, A. P.; Burant, J. C.; Iyengar, S. S.; Tomasi, J.; Cossi, M.; Millam, J. M.; Klene, M.; Adamo, C.; Cammi, R.; Ochterski, J. W.; Martin, R. L.; Morokuma, K.; Farkas, O.; Foresman, J. B.; Fox, D. J. Gaussian, Inc., Wallingford CT, **2016.**

S9. Glendening, E. D.; Landis, C. R.; Weinhold, F. NBO 6.0: Natural bond orbital analysis program *J. Comput. Chem.* **2013**, *34*, 1429-1437.

S10. Reed, A. E.; Curtiss, L. A.; Weinhold, F. Intermolecular Interactions from a Natural Bond Orbital, Donor-Acceptor Viewpoint. *Chem. Rev.* **1988**, *88*, 899-926.

S11. Ziegler, T., Rauk, A. On the calculation of bonding energies by the Hartree Fock Slater method. *Theor. Chim. Acta* **1977**, *46*, 1–10.

S12. Mitoraj, M.; Michalak, A. Donor-Acceptor Properties of Ligands from the Natural Orbitals for Chemical Valence *Organometallics* **2007**, *26*, 6576 – 6580.

S13. Mitoraj, M.; Michalak, A. Applications of natural orbitals for chemical valence in a description of bonding in conjugated molecules. *J. Mol. Model.* **2008**, *14*, 681-687.

S14. *ADF2020, SCM, Theoretical Chemistry*; Vrije Universiteit: 782 Amsterdam, The Netherlands http://www.scm.com

S15. Michalak, A.; Mitoraj, M.; Ziegler, T. Bond Orbitals from Chemical Valence Theory. *J. Phys. Chem. A* **2008**, *112*, 1933-1939.

S16. Mitoraj, M. P.; Michalak, A.; Ziegler, T. A Combined Charge and Energy Decomposition Scheme for Bond Analysis. *J. Chem. Theory Comput*. **2009**, *5*, 962-975.

S17. E. J. Shellard, W. T. Diment, D. A. Resendiz-Lara, F. Fiorentini, G. L. Gregory and C. K. Williams, *ACS Catal*, 2024, **14**, 1363-1374.

S18. P. Partovi-Azar, T. D. Kühne and P. Kaghazchi, *Phys. Chem. Chem. Phys.*, 2015, **17**, 22009–22014.

S19. A. A. Jarzęcki, *J. Phys. Chem. A.*, 2012, **116**, 571-581.

S20. M. Boumediene, B. Haddad, A. Paolone, M. A. Assenine, D. Villemin, M. Rahmouni and S. Bresson, *J. Mol. Struct.*, 2020, **1220**, 128731.

S21. J. R. Ferraro, Low-frequency vibrations of inorganic and coordination compounds, *Springer Science & Business Media*, 2012. Publisher Springer New York, NY; ISBN978-1-4684-1811-8, 978-1-4684-1809-5.

S22. G. Socrates, Infrared and Raman characteristic group frequencies: tables and charts, *John Wiley & Sons*, 2004; ISBN: 978-0-470-09307-8;